

An Investigation of Fault-Zone Hydrogeology
and Geomechanical Tidal Behavior,
South Ellwood Field, California

A Thesis by
Jeremy R. Stone

In partial fulfillment of the requirements for the degree of
Master of Science
in
Civil and Environmental Engineering

TUFTS UNIVERSITY

May 2013
© 2013 Jeremy R Stone

ADVISOR: Professor Grant Garven

Abstract

This thesis uses a reduced tidal signal to calculate poroelastic properties (hydraulic diffusivity and loading efficiency) of a fault-zone in the Santa Barbara Basin. The data set utilized shows an attenuated tidal signal at a depth of 1,500 m.

Fast Fourier Transform (FFT) and least squares harmonic regression were employed to decompose the tidal signal and pressure signal at depth. The FFT revealed tidal frequencies in the signal at depth while the least squares regression determined amplitude and phase of the five major tidal constituents.

Three analytical models were applied to determine poroelastic properties: treating the amplitude reduction as a measure of loading efficiency, determining the hydraulic diffusivity based on adaptations of heat flow solutions and the application of elastic and diffusive model of van der Kamp. A numerical model in SEEP/W simulates the tidal signal propagation effects into rock units surrounding the fault-zone.

Dedication

This thesis is dedicated to my grandmother Gloria Madruga. Your dedication to lifelong learning and perseverance should be an example to the world. Thank you and your generation for passing the torch and preserving our freedoms.

Acknowledgments

In finishing this Thesis I would like to say thank you to the many individuals and organizations who have helped me complete it. No work of this nature is conducted in isolation and its success is due to the helpful, caring, correcting and patient nature of the people who have surrounded me now and throughout my life.

I would first like to acknowledge my Thesis Advisor Dr. Grant Garven and committee members Dr. Anne Gardulski and Dr. Christopher Swan. Thank you for agreeing to be on my committee and providing me with the guidance to complete this work. I have benefitted greatly from your input as both educators and practitioners. The lessons I have learned here and in your classroom I will take with me.

Next I would like to thank Venoco Inc and Dr. James Boles of UCSB. You provided me with a truly unique data set to work with and I have tried to do as much as I could with it. Thank you for providing me with technical data concerning the geologic profile beneath Platform Holly and for answering my questions. It is my sincere hope that this Thesis is of practical value.

I thank my good friends, some I have known for years and others just recently. It is a sad necessity that I cannot list all your names.

I would like to thank my girlfriend Alessandra for her personal support and practical advice concerning signal analysis. I am fortunate to have you in my life.

Finally, I would like to thank my parents Paul and Bridget Stone. I have only succeeded because of the support you gave me. Thank you for the camping trips, the Sunday drives, the time spent on the boat, and most importantly, a good education. This acknowledgment is not enough.

Table of Contents

Abstract.....	ii
Dedication.....	iii
Acknowledgment.....	iv
List of Symbols.....	xv
Chapter 1: Introduction.....	17
1.1 Context/Motivation.....	17
1.2 Thesis Objective.....	18
1.3 Background /Literature Review.....	19
1.3.1 Geology of the Santa Barbara Basin.....	19
1.3.2 Fault-Zone Hydrogeology.....	24
1.3.3 Use of Tidal Signal to Determine Formation Properties.....	27
1.4 Thesis Approach.....	29
1.5 Poroelastic & Hydraulic Definitions.....	32
1.6 Thesis Organization.....	41
Chapter 2: Data and Platform Holly.....	43
2.1 Overview.....	43
2.2 Venoco Inc., Platform Holly, South Ellwood Field.....	43
2.3 Well #13 Data Set.....	48
2.4 Summary.....	53

Chapter 3: Signal Analysis and Analytical Solutions	54
3.1 Overview.....	54
3.2 Tidal Theory.....	55
3.3 Analysis of the Tidal Signal	58
3.3.1 Fourier Analysis	58
3.3.2 Least Squares Harmonic Regression	61
3.3.3 Application of Signal Analysis Methods	62
3.4 Analytical Solutions	72
3.4.1 Skempton / Loading Efficiency	72
3.4.2 Jacob / Ferris Model.....	82
3.4.3 van der Kamp and Wang Solution.....	87
3.5 Summary	93
Chapter 4: Application of Numerical Modeling	95
4.1 Overview.....	95
4.2 Assumptions and Simplifications	95
4.3 Simulation of Tidal Signal Propagation down Fault Zone.....	100
4.4 Effect of Hydraulic Diffusivity on Signal Propagation	117
4.5 Summary	122
Chapter 5: Conclusions	123
5.1 Thesis Summary.....	123

5.2 Discussion of results	124
5.2.1 Applications of Analytical Models	124
5.2.2 Application of SEEP/W numerical modeling	126
5.3 Global Conclusions and Fault Zone Formation Properties	129
5.4 Suggestions for Future Work	132
References.....	134
Appendix	140

List of Tables

Table 1. Frequencies for basic harmonic constituents.	58
Table 2. Result of least squares harmonic regression with amplitude comparison to Santa Barbara Station.	71
Table 3. Ratios for each constituent calculated from Table 2 and least square harmonic regression.....	71
Table 4. Diffusivity from equation 26.....	86
Table 5. Input parameters for determining diffusivity from time lag	87
Table 6. Calculation of diffusivity from time lag	87
Table 7. Calculation of loading efficiency from Wang & van der Kamp model	89
Table 8. Typical formation properties for model simulation. Fault zone formation properties keep the fault diffusivity at $13.9 \text{ m}^2/\text{s}$	100

List of Figures

- Figure 1: Santa Barbara Channel and location of Platform Holly. Contour Interval of 100 m. Platform Holly is where data set was gathered. Base map from GeoMapApp <http://www.geomapp.or>..... 21
- Figure 2. Representative stratigraphy within Santa Barbara basin. Re-drawn from USGS paper by Vedder et al (1969) and cross section by Tennyson and Kropp (1998) summarizing the work of various researchers. 22
- Figure 3. Working model of fault zone architecture and hydrology. Figure at left shows different zones of a fault zone and is after Chester and Logan (1986). Figures at right illustrate different hydraulic regimes that can develop within a fault zone based on the varying amounts of core and damage zone. Figures redrawn from Caine et al (1996)... 25
- Figure 4. Flowchart showing process of analysis utilizing signal analysis, analytical solutions and numerical modeling..... 31
- Figure 5. Illustration of the statics and forces used to derive both Jacob's tidal efficiency and Skempton's coefficient. A) three dimensional loading of porous media B) balance of static forces C) two dimensional view of loading. 37
- Figure 6: Cross section below Platform Holly showing Well #13, faults and stratigraphy. Re-drawn with permission of Venoco Inc..... 46

Figure 7. Details for Well #13 showing completions with stratigraphy and notes about electrical resistivity. Re-drawn from information provided by Venoco Inc. 47

Figure8:Kuster gauge (www.kusterco.com/pdfs/2012/Probe_Kuster_K10_Quartz_XT.pdf) 49

Figure 9: Sensor pressure data recorded at 5,000 ft below sea level in Well # 13. 50

Figure 10: Pressure head signal at depth without instrument calibration..... 51

Figure 11: Tidal signal corresponding to the same period of time as pressure signal at depth. 52

Figure 12: Positions of Moon and Earth at spring and neap tides. Lower figure illustrates tidal bulges from gravitational pull of the moon and inertial forces. (www.en.wikipedia.org/wiki/tide and www.oceanservice.noaa.gov) 57

Figure 13: Components of a sine wave bottom figure from wikipedia.org/wiki/phase ... 59

Figure 14: Straight lines and equations used to de-trend data set for pressure signal at depth. It should be noted that original data reduction technique was done by Ms. Carley Petterson working with Prof. James R. Boles of USCB. This work utilizes a slightly different linear equation and expresses formation pore pressure in terms of pressure head. 64

Figure 15: De-trended pressure signal at depth. 65

Figure 16: Plot of de-trended tidal signal and pressure signal at depth. The dashed line is the pressure signal multiplied by an arbitrary scaling factor of 5 to further illustrate its relation to the tidal signal. Original data reduction technique was done by Ms. Carley Petterson working with Prof. James R. Boles of UCSB. 66

Figure 17. Frequency spectrum for both tidal signal and pressure signal at depth illustrating that the frequencies seen in the tidal signal are also seen in the pressure signal at depth. 67

Figure 18. Graphical result of least squares harmonic regression on tidal signal with amplitudes and phase angles seen in Table 2. 69

Figure 19. Graphical result of least squares harmonic regression on pressure signal at depth with amplitudes and phase angles seen in Table 2..... 70

Figure 20. Loading efficiency chart for various common Poisson’s ratio assuming pore fluid is water and porosity $n=15\%$ 73

Figure 21. Loading efficiency chart for various common Poisson’s ratio assuming pore fluid is water and porosity $n=20\%$ 74

Figure 22. Loading efficiency chart for various common Poisson’s ratio assuming pore fluid is water porosity $n=25\%$ 75

Figure 23. Loading efficiency chart for various common Poisson's ratio assuming pore fluid is water porosity $n=30\%$	76
Figure 24. Loading efficiency chart for various common Poisson's ratio assuming pore fluid is gas porosity $n=10\%$	78
Figure 25. Loading efficiency chart for various common Poisson's ratio assuming pore fluid is gas porosity $n=15\%$	79
Figure 26. Loading efficiency chart for various common Poisson's ratio assuming pore fluid is gas porosity $n=20\%$	80
Figure 27. Loading efficiency chart for various common Poisson's ratio assuming pore fluid is gas porosity $n=30\%$	81
Figure 28. Amplitude reduction for K1 tide constituent as a function of depth. Diffusivity = $13.9 \text{ m}^2/\text{s}$ with three different values of loading efficiency γ	91
Figure 29. Amplitude reduction for M2 tide constituent as a function of depth. Diffusivity = $13.9 \text{ m}^2/\text{s}$ with three different values of loading efficiency γ	92
Figure 30: SEEP/W Model with stratigraphy, fault zones and mesh. Vertical axis in meters.....	98
Figure 31: Tidal stage vs. time as top boundary condition for the simulation.	102

Figure 32: Diffusive signal propagation and original tidal signal at depth 1208m (4,000 ft). D=13.9 m ² /s	104
Figure 33. Diffusive signal propagation and original tidal signal at depth 1500m (5,000 ft). D=13.9 m ² /s	105
Figure 34. Diffusive and elastic signal with tide at 1208 m (4,000ft).....	107
Figure 35. Diffusive and elastic signal with tide at 1500m (5,000 ft).....	108
Figure 36. Signal attenuation, model prediction and analytical solution.	110
Figure 37. Pressure head changes vs distance along the fault for the falling of the tide.	111
Figure 38. Pressure head changes vs distance along the fault for the rise of the tide.....	111
Figure 39. Pressure head propagation down fault towards the Monterey Formation. Lines are of constant pressure head. t=9 hrs.	113
Figure 40. Start of high pressure pulse propagating down fault zone and start of propagation into Monterey Formation. t=11hrs.....	114
Figure 41. Later pressure propagation showing that tidal pulse has travelled further down fault. t=14 hrs.....	115

Figure 42. Signal propagation into Monterey Formation (blue). Lines show constant pressure head. $t=236$ hrs. Y axis in meters below sea level..... 116

Figure 43. Diffusive Signal and Tidal Signal at -1500 m for $D=9.7 \text{ m}^2/\text{s}$. Note that signal predicted by model is marginal compared with tide. 118

Figure 44. Diffusive and elastic signal with tide at -1500 m for $D=9.7 \text{ m}^2/\text{s}$. Note how elastic signal component overwhelms the diffusive signal and makes it seem as if there is no time lag. 119

Figure 45. Diffusive signal and tidal signal at -1500 m for $D=18.1 \text{ m}^2/\text{s}$. Both the diffusive signal (model prediction) and the tidal signal are plotted in the figure but since the tidal signal does not attenuate they remain the same and no distinction appears. 120

Figure 46. Diffusive Signal with elastic component added on with tidal signal at a depth of 1500 m for $D=18.1 \text{ m}^2/\text{s}$. Note how signal at depth is actually greater than tidal signal. 121

Figure 47. Possible specific range for storage and hydraulic conductivity for the South Ellwood fault zone. 130

List of Symbols

A = amplitude

A' = Skempton's parameter

β_p = compressibility of pores

β_{sz} = undrained, uniaxial, compressibility in the vertical direction

β_{s1} = undrained compressibility in the σ_1 direction

β_{s2} = undrained compressibility in the σ_2 direction

β_{s3} = undrained compressibility in the σ_3 direction

β_w = compressibility of water

B = Skempton's parameter

γ = loading efficiency (L.E. or tidal efficiency T.E.)

$\Delta\phi$ = phase difference

Δu = change in pressure from surface loading

ε = strain

k = intrinsic permeability

K = hydraulic conductivity

K_b = bulk modulus of porous medium

K_f = fluid modulus

K_s = modulus of solids

K_u = undrained bulk modulus

K_v = undrained, uniaxial, vertical compressibility

μ = viscosity (dynamic)

ν = Poisson's ratio

ρ = density of water

σ_m = mean stress

σ_n = stress in the n direction

ω = angular frequency of a tidal constituent

C = Skempton's parameter

D = hydraulic diffusivity (coefficient of consolidation)

f = frequency

h = hydraulic head

n = porosity (effective)

S_s = specific storage

t = time

t_1 = time lag

T = period of a tidal constituent

x = distance

Chapter 1: Introduction

1.1 Context/Motivation

The hydrogeology of fault zones is a subject that is of increasing importance because of the wide array of its implications for many different technologies and scientific disciplines. The subject of fault zone hydrogeology concerns itself with all the hydraulic, geologic and geomechanical processes occurring along a fault zone, as related to or derived from the flow of groundwater or other fluids. The importance of such processes is apparent in understanding the buildup of stress and pore pressure in an active tectonic environment, modeling the entrapment of CO₂ in carbon sequestration, and understanding the migration of oil and natural gas in faulted sedimentary basins (Levorsen, 1967; Drake, 1978; Stanislavsky and Garven, 2003). Fault zone hydrogeology became an important topic in the development of the Yucca Mountain Nuclear Repository where a complete understanding of the flow of groundwater through the mountain and its multiple faults was essential to designing a safe facility (Shan et al., 1999; Ning Lu, 2001).

Despite such a wide range of applications the hydraulics of faults are not well understood and many questions remain unanswered. Some of the most basic and important questions are:

- 1) Do fault zones act as barriers or conduits to fluid flow?
- 2) What are the mechanical properties of fault zones?
- 3) How do faults affect the migration of geofluids?
- 4) What is the permeability of a fault zone?

5) How do faults react to other hydraulic perturbations such as pumping wells, injection wells for waste disposal, carbon sequestration or hydrofracking, and natural processes such as earthquakes?

The complex interactions of fluids, rocks, sediments, pressure buildup and stress fields requires an understanding of geology, hydrogeology, geophysics and in many cases fundamental engineering principles.

1.2 Thesis Objective

The objective of this thesis is to contribute to a better understanding of fault zone hydrogeology through the analysis of a unique data set gathered in the field. The thesis focuses on the hydraulic and mechanical properties of fault zones to determine important physical parameters that may be used in applied geomechanics and groundwater hydrology. This work may be useful for modeling mechanical stresses and fluid flow as coupled hydromechanical systems in basins that are bounded or cut by faults.

It is also the objective of this thesis to provide a well documented case study for utilizing tidal-signal propagation in an aquifer to calculate geomechanical and hydraulic properties. The background section can be looked at as a basic review of the essential theory and can serve as a guide to any future work with tidal signal propagation.

Finally, through numerical simulations the thesis models the tidal pressure fluctuation and signal propagation down a fault zone and into a conductive zone of the Monterey Formation, off-shore southern California. Using the physical parameters previously determined, the interactions of poroelasticity and fluid flow are also explored in

light of the active extraction of oil & gas in the study area. These simulations are meant to demonstrate concept and are not exact engineering studies.

1.3 Background /Literature Review

1.3.1 Geology of the Santa Barbara Basin

The Santa Barbara basin is sedimentary basin that lies both off shore and on shore in southern California. Geologically, the basin is bounded to the north by the Santa Ynez fault and continues on shore to the east where it is bounded by the San Gabriel Fault. The southern boundary is made of a system of faults crossing the Santa Monica Mountains and the Channel Islands (Galloway, 1998). The basin exists in its present form as a result of the compressional tectonic forces existing in the Transverse Range Province. The compression is a result of the Big Bend in the San Andreas fault system and is actively deforming the landscape into a series of synclines and anticlines. The syncline structures are actively filling with sediment and forming basins such as the Los Angeles whereas anticlines are building into transpressive mountain ranges such as the Santa Ynez (Harden, 1998).

Presently, the Santa Barbara Channel overlies much of the basin. The Santa Barbara Channel appears as an oblong shaped depression with an approximate bathymetry of 550 m at its center. Figure 1 shows the location of the basin and the Santa Barbara Channel along with the location of Platform Holly where the data set utilized in this thesis was gathered.

All the sedimentary formations existing in the basin predate the present tectonic environment and represent a complicated and unique geologic history and stratigraphy. A strip log showing a representative geology and geologic time beneath the channel is

displayed in Figure 2. This sequence starts in the Oligocene with the Sespe Formation which is overlain by the Rincon Formation. The Sespe and Rincon represent shallower water depths where more clastic material was being deposited in off shore deltas and submarine landslides. These rock units rest above the basal Franciscan and Jalama Formations. Of the Oligocene rocks the Sespe is most recognizable by its coarse sandstone and conglomeritic layers. The Sespe and Rincon Formation are thought to represent a range of depositional environments that are shallow marine to non marine (Galloway, 1998). A cross section of the coast from the Santa Ynez Mountains to the Santa Barbara Channel is included in the appendix.

Starting in the Oligocene and continuing to the Holocene, the basin has undergone significant rotation (120 deg) accompanying major tectonic events such as the basin subsidence and deposition of the Vaqueros Sandstone and the Monterey Shale. During the period of basin subsidence formations such as the Monterey were deposited in an off shore ocean environment. The Monterey Formation is believed to be Miocene age and is comprised of claystone, siltstone and silicified shale layers (Minor et al., 2007). This formation represents the most active oil and gas play in the basin and is the primary source rock for much of the petroleum in California. The data set utilized in this study was gathered from an oil and gas well completed in the Monterey Formation. The location of this well, drilled from Platform Holly, is shown in Figure 1.

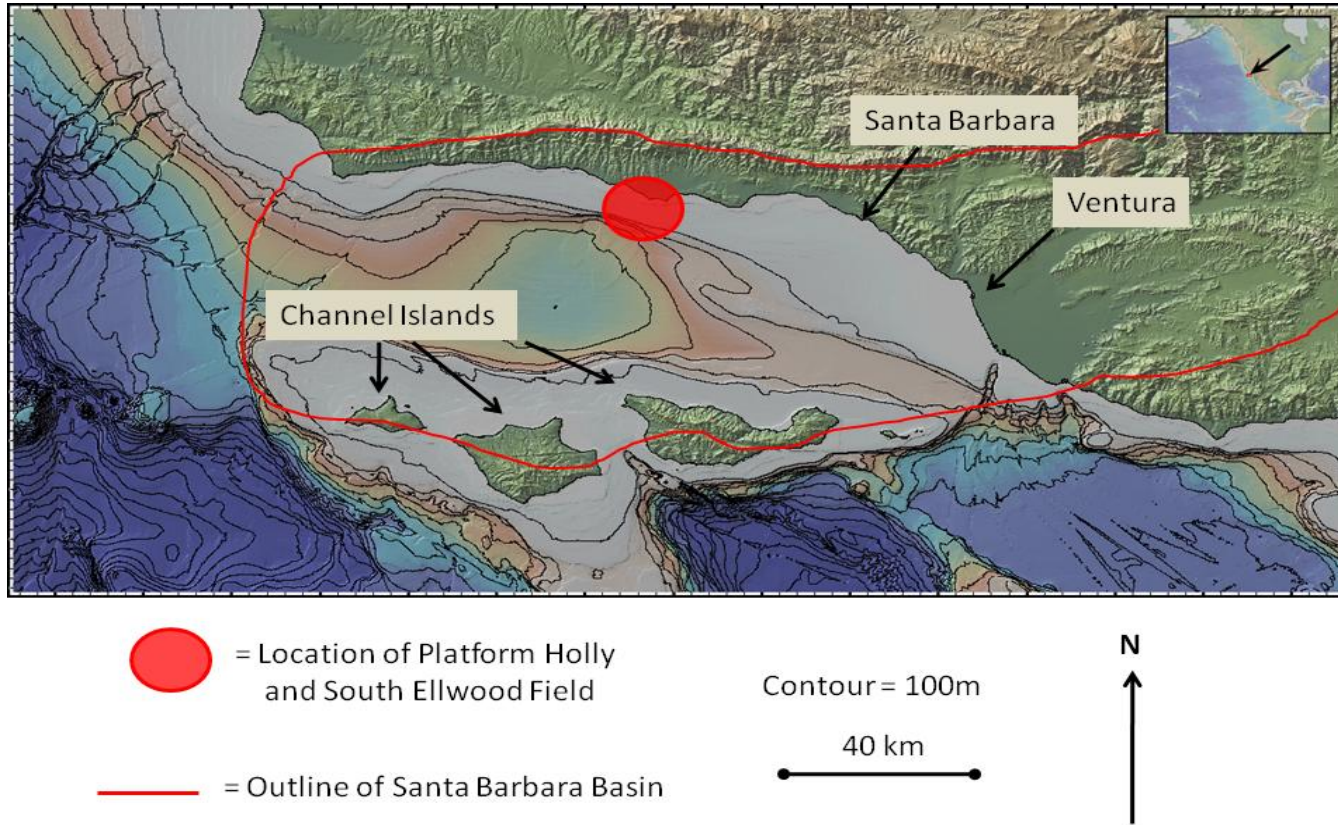


Figure 1: Santa Barbara Channel and location of Platform Holly. Contour Interval of 100 m. Platform Holly is where data set was gathered. Base map from GeoMapApp <http://www.geomapp.org>

		Symbol	Stratigraphic Unit	Lithology	Thickness (m)
Miocene	Late		Sisquoc Formation	diatomaceous mudstone; bathyal	975+
	Middle		Monterey Formation	Thin-bedded siliceous mudstone, calcareous mudstone, marl, diatomaceous mudstone, phosphatic shale, chert, porcelaneous shale, sandstone beds in lower part, bathyal	305 - 915
	Early		Rincon Formation	gray-brown mudstone with orange-weathering dolomite nodules; sandstone beds locally in upper part. bathyal	0 - 518
Pre-Miocene sedimentary rocks and Mesozoic Franciscan Complex					

Figure 2. Representative stratigraphy within Santa Barbara basin. Re-drawn from USGS paper by Vedder et al (1969) and cross section by Tennyson and Kropp (1998) summarizing the work of various researchers.

Minor et al (2007) divided the fractured shale units of the Monterey Formation into 3 units: an upper siliceous unit, a middle shale unit, and a calcareous unit. Logs provided for Well #13 show the lower units as containing higher hydrocarbon concentrations. The Monterey serves as both a hydrocarbon source as well as a reservoir formation. Petroleum and natural gas tend to accumulate within localized fracture networks.

Above the Monterey Formation rests the Sisquoc Formation, a younger siliciclastic deposits which ranges from the late Miocene to the early Pliocene. The Sisquoc is separated from the Monterey by coarser conglomerate layers that have been found to rest conformably and unconformably on the Monterey (Minor et al., 2007).

The extensional tectonic changes started during the Miocene, and culminated in the compressional and transpressional tectonics that produced the recent uplift of the Santa Ynez Mountains (Galloway, 1998). This compressional environment is believed to have re-activated many older reverse faults. This re-activation has turned previous normal faults into reverse faults (Galloway, 1998). Field studies and mapping projects both on shore and beneath the Channel reveal a sequence of sedimentary rocks folded into anticlines, synclines and cut by numerous smaller faults. (Heck, 1998; Tennyson and Kropp, 1998; Redin et al., 1998). The faulting and deformational events resulted in compartmentalized petroleum reservoirs in the basin which must be accurately understood by the petroleum companies in order to extract hydrocarbons.

Faults are thought to provide the primary conduit for oil and gas seeping to the seafloor in the Santa Barbara Channel (Boles et al., 2001). The seepage near Platform Holly is substantial enough that it was possible to install large seep tents on the ocean floor to capture natural gas escaping up the fault. These seep tents can be used as a large permeameter to determine the fault zone permeability since accurate records of pressure

change and flow rate exist for the faults. Boles et al. (2001) estimated a fault permeability at 30 md which corresponds to a conductivity of 3×10^{-7} m/s.

1.3.2 Fault-Zone Hydrogeology

While not the first to write about the nature of fault-zone hydrogeology, Caine et al. (1996) provide an invaluable review of the topic from a hydrogeologic perspective. In this paper the authors lay out a model of fault-zone hydrology that is structural, hydraulic, and mechanical. Their paper breaks the fault zone into three zones: the core, the damage zone, and the protolith. The authors argue that each area has distinct hydraulic properties including anisotropy and conductivity. The ratio of the width of the damage zone to total fault zone width is said to be the controlling influence on the type of hydraulic regime that develops in and around the fault zone, although other factors such as rock type (lithology) do play a role (Caine et al. 1996). Their model (Figure 3) shows the central core of the fault zone made of distinctly different material such as clay or cataclastite which is the product of the mechanical crushing of rock between the hanging wall and the foot wall. Immediately outside the fault core exists a fractured “damaged” zone which transitions to the undamaged protolith. In general the damaged zone can transmit fluid horizontally but such transmission is stopped at the fault core. Vertical permeability and transmissivity are generally higher along the fault-zone.

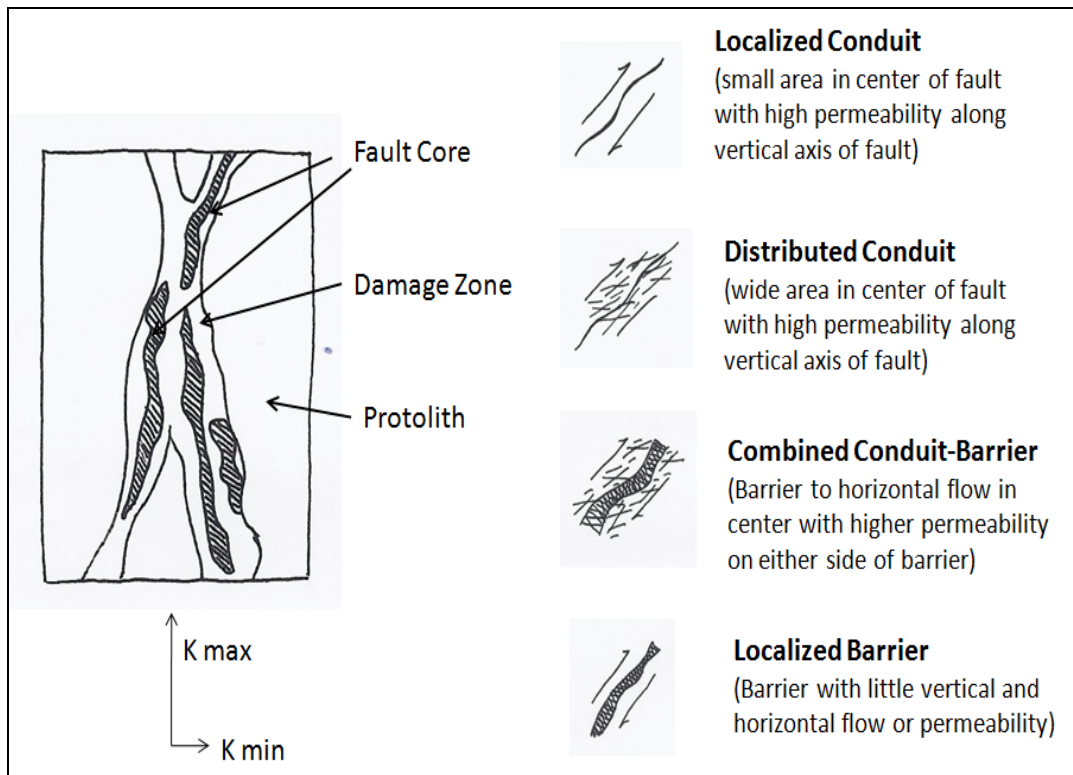


Figure 3. Working model of fault- zone architecture and hydrology. Figure at left shows different zones of a fault zone and is after Chester and Logan (1986). Figures at right illustrate different hydraulic regimes that can develop within a fault zone based on the varying amounts of core and damage zone. Figures redrawn from Caine et al (1996).

This fault zone model has proven to be a useful tool for geologists studying fault zone hydrogeology and geomechanical behavior. There exist some excellent field studies where various researchers have mapped the three different fault zones proposed by Caine et al (1996) and have shown how the percentages of sand, silt and clay change as one moves through the three distinct zones. (Heynekamp et al., 1999; Nelson et al., 1999; Sigda et al., 1999; Adyin, 2000; Odling et al., 2004). Many of the detailed field studies were conducted on surface outcrops, and borehole data in sedimentary rocks the model have been used to study hydrogeology of igneous and igneous/sedimentary fault zones (Evans et, al. 1997). In this case the three distinct zones were also mapped and the fault zone was found to be a barrier to horizontal flow.

The division of a fault into three different zones is critical when attempting to evaluate the buildup of stress from a quantitative mechanics point of view. The accuracy and usefulness of geomechanical equations requires determination of the geometry, hydraulic, and poroelastic properties of the fault. Recently the application of geomechanical modeling has been used to model stress buildup on fault systems and explore the pressure changes occurring with an anisotropic fault system (Cocco and Rice, 2002). Mechanical modeling has also proven useful when investigating fault valve behavior where water is released up a fault zone immediately following an earthquake (Stanislavsky and Garven, 2003; Sibson, 2007).

Because fault zones are capable of compartmentalizing petroleum reservoirs and acting as traps to petroleum migration the petroleum geology community has taken a great interest in this research (Odling et al., 2004). Antonelli and Aydin (1999) studied a fault exposed in cross section in railroad and highway cuts. They investigated deformation banding adjacent to the fault, and found that the banding could help trap petroleum. The study showed that the fault acted as barrier to horizontal oil migration and

acted as a vertical conduit, which allowed water to travel down the fault and degrade the petroleum.

1.3.3 Use of Tidal Signal to Determine Formation Properties

Poroelasticity theory is central to the calculation of various fault zone hydraulic properties. Various theories were developed by many authors early in the 20th century who noted the relationship between increased surface load above a saturated soil medium and the concurrent increase in pore pressure and effective stress in the saturated soil. The theory was well developed by Biot (1941, 1956), and by Terzaghi (1923, 1943) who was the first to come up with an accurate methodology to calculate building settlement in clay deposits (Holtz and Kovacs, 1981). Jacob (1940) was the first to create an equation that accurately predicted the transmission of the aquifer loading to the pore pressure based on the compressibility of both the water/pore fluid and the soil/rock solids. Similar parameters that relate the surface loading or pressure to pore pressure were also developed by the British engineer Skempton (1961) (Lambe et al., 1969).

Jacob and Ferris (1951) recognized the applicability of the theory to coastal aquifers where the rising and falling of the tide acted as a transient loading on the aquifer which was recorded in wells on shore. While the rising and falling of the tide appeared in coastal wells it was always offset by some time lag. Jacob and Ferris were quick to recognize that the phenomenon was governed by the parabolic partial differential diffusion like heat equation (Jacob, 1940; Ferris, 1951). An analytical solution was developed that allowed one to solve for various hydraulic properties by first solving for hydraulic diffusivity coefficient based on time lag and frequency of the tide.

The Ferris (1952) solution placed the entire tidal fluctuation as a boundary condition on an aquifer that abruptly terminated at the coast. This solution was found to

give an accurate estimate of hydraulic properties for only a limited set of geologic conditions that rarely conformed to this boundary assumption. Later work focused on the solution of the diffusion equation with a confined aquifer stretching under the sea an infinite distance and a leaky aquifer extending only a partial distance under the sea (Carr and van der Kamp, 1960; van der Kamp, 1972; Jiao and Tang, 1999). Later work by van der Kamp (1983) fully modified the equations to take into account both the diffusive part of the tidal signal and the poroelastic part. The end result of this history is to have three different analytical solutions. These mathematical/hydromechanical models are:

1. Skempton's coefficient (also known as Loading Efficiency or Tidal Efficiency),
Purely Elastic.
2. Purely diffusive (Jacob/Ferris)
3. Elastic and diffusive (van der Kamp 1983)

The application of poroelastic theory and pressure wave transmission through a saturated aquifer has had limited applications through the years. Van der Kamp and Carr (1969) utilize the tidal and well fluctuations to calculate the hydraulic properties of sedimentary rocks in Prince Edward Island and Nova Scotia (Canada) while Ferris illustrates the use of the method to calculate properties for a sand and gravel aquifer subject to river fluctuations in Nebraska. A comparison by Carr and van der Kamp with pump-test data shows good agreement between hydraulic properties calculated by the tidal method and those calculated by traditional pump testing. The method was also used to estimate hydraulic properties for the Floridian aquifer system and good agreement was found when comparing properties derived from pump testing, barometric fluctuations and tidal fluctuations (Merritt, 2004). This USGS study was very thorough in breaking the

tidal signal and aquifer pressure signal into its different frequencies and commenting on the best fit nature of each of the three models described above.

The best known use of poroelastic theory and pressure fluctuations in studying faults is an attempt to use barometric and Earth tide pressure fluctuations to infer hydraulic regimes and calculate permeability. These studies were conducted to determine the natural hydraulic regimes around the proposed nuclear repository site at Yucca Mountain in Nevada. The studies all used some version of a diffusive equation to model the pressure wave attenuation and time lag with depth. The values of permeability calculated appear to be reasonable in respect to the geologic information available about the site (Bredehoeft, 1997; Chao et al., 1999; Lu, 2001).

1.4 Thesis Approach

In analyzing the tidal signal and its associated propagation down the fault, I will utilize theory from geomechanics, hydrogeology, oceanography, and signal analysis. The approach to be used in this thesis (Figure 4) starts with classical tidal analysis of both the Santa Barbara tidal signal and the signal recorded at depth by the pressure transducer. The analysis will take the form a least squares harmonic regression and the application of a discrete Fourier transform. The purpose of the harmonic regression is to break the tidal signal down into its five basic harmonic constituents and obtain estimates of the phase angle and amplitude of each. The Fourier analysis will be utilized to construct a frequency periodiagram showing that the frequencies seen in the pressure signal recorded near the fault are the same frequencies seen in the ocean tidal signal.

After the tidal analysis is complete, three possible analytical solutions will be applied to the data set to determine hydraulic diffusivity and loading efficiency. The

application of these solutions will be discussed along with the applicability of each to the data set. This approach has proven useful for other researchers investigating tidal phenomenon when studying the Floridian aquifer system (Merritt, 2004). This application will be followed by finite element modeling of the fault zone and its immediate geology. The purpose of this modeling is to illustrate and replicate the signal propagation and explore how water and fluids are moving through the fault zone and how they might be affecting the Monterey Formation.

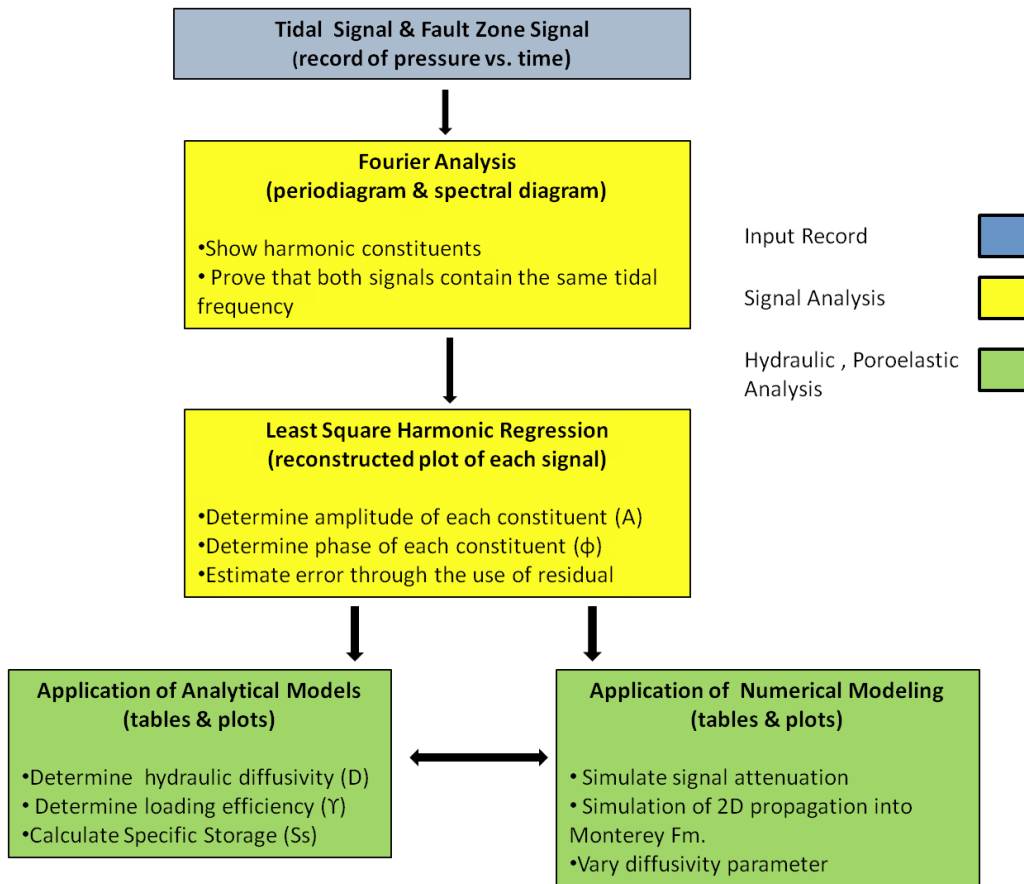


Figure 4. Flowchart showing process of analysis utilizing signal analysis, analytical solutions and numerical modeling.

1.5 Poroelastic & Hydraulic Definitions

This section discusses the basic parameters that are important in the development of the theory used to study the hydraulic and mechanics of the fault system. Many of the parameters listed here are the poroelastic coefficients that this study seeks to quantify in relation to the fault zone material. Over the years some of the parameters listed here have been defined differently by different researchers. The descriptions below are created to define things in terms of this study and the interested reader is encouraged to consult many of the quoted references for further more in-depth discussions and derivations. The reader is encouraged to consult the list of symbols at the start of the thesis for the meaning of each variable.

Hydraulic Conductivity K

Hydraulic conductivity is defined as a coefficient of proportionality that relates the volumetric flow per cross section of porous media and gradient in hydraulic head (Freeze and Cherry, 1979). Hydraulic conductivity is a property that is unique to an isotropic homogeneous medium provided the fluid does not change in viscosity or density. This physical parameter is used extensively in geotechnical engineering, soil mechanics, and hydrology since water is the primary fluid of concern and its properties are assumed constant for many practical applications.

Intrinsic Permeability k

Permeability also is defined by Darcy's Law, but characterizes the physical attributes of pore geometry and tortuosity of the flow channels. It is related to conductivity based on density and viscosity and is related to conductivity by the following expression (Hubbert, 1940):

$$K = \frac{k\rho g}{\mu} \quad (1)$$

Permeability is used extensively in the petroleum industry, soil physics and environmental engineering where often there are other fluids than water in the problem domain, such that multiphase fluid dynamics are required.

Specific Storage S_s

Specific storage is a widely used parameter that characterizes the storage properties of a porous medium based on compressibility terms. Physically this parameter quantifies the volume of water released from a unit volume of aquifer under a unit decline in hydraulic head or fluid pressure. Nur and Byerlee (1971) showed that one can define two dimensionless parameters commonly seen in the poroelastic literature:

$$\alpha = 1 - \left(\frac{K_b}{K_s} \right) \quad (2)$$

$$\lambda = \left(\frac{2\alpha(1-2\nu)}{3(1-\nu)} \right) \quad (3)$$

The first relates the bulk modulus of the entire porous medium (K_b) to the modulus of the solid fraction. This value ranges from 0 to 1 and gives a measure of compressibility of the pore space in relation to the solid fraction. The second parameter is also dimensionless and is meant to account for two dimensional strain. From these equations one can define specific storage using the Biot's theory as the following equation (van der Kamp and Gale, 1983).

$$S_s = \rho g \left[\left(\frac{1}{K_b} - \frac{1}{K_s} \right) (1 - \lambda) + n \left(\frac{1}{K_f} - \frac{1}{K_s} \right) \right] \quad (4)$$

For most engineering and many hydrogeology problems, it is acceptable to assume that strain is mostly vertical and therefore deformation is one dimensional. This assumption implies that (2) is equal to zero. Under these conditions, can simplify (4), which is the specific storage commonly used in hydrogeology and the basic groundwater flow equation (Domenico and Schwartz, 1990),

$$S_s = \rho g \left[\left(\frac{1}{K_b} - \frac{1}{K_s} \right) + n \left(\frac{1}{K_f} - \frac{1}{K_s} \right) \right] \quad (5)$$

Jacob (1940) first derived this expression of the specific storage by considering a porous control volume that was undergoing vertical 1-D deformation due to a unit drop in head. Jacob reasoned that water released from storage was created both by the expansion of water and the elastic dilation of the medium. In Jacob's expression, the solid fraction is assumed to be incompressible and all compressibility is due to the collapse of the pores. This simplification means that the bulk modulus is also the modulus of the pores (Domenico and Schwartz, 1990; Wang, 2000) such that:

$$S_s = \rho g (\beta_p + n\beta_w) \quad (6)$$

The pore compressibility term in equation 6 can be expressed in terms of bulk modulus as (7).

$$\beta_p = \frac{1}{K_b} \quad (7)$$

It is understood that there is some confusion and a bit of an enigma surrounding (6) with the use of the compressibility defined in (7). Equation 7 is defined using bulk modulus which is really a three-dimensional parameter. This parameter is then utilized in (6), derived by Jacob assuming that strains occur in the vertical dimension only. It would be possible to utilize a vertical (uniaxial) modulus only, but this would not represent the actual natural world for most hydrogeology problems so it is better to use the bulk modulus. It was also pointed out by DeWiest in (1966) and mentioned in Bear (1972) that Jacob's original derivation of (6) was incorrect due to the assumptions made about the deforming control volume. While these criticisms of Jacob's original work were accurate (6) was still proven to be accurate when considering deformation in the vertical axis only (Domenico and Schwartz, 1990).

Tidal Efficiency, Skempton's Coefficient, and Loading Efficiency

Jacob (1940) noted that pore pressures would rapidly increase within an aquifer when an external loading was applied suddenly or the hydraulic conductivity was small. By considering the water within the aquifer to be non-draining and stationary Jacob derived a coefficient that would relate the change in surface loading to the change in pore pressure. This parameter was derived by considering the aquifer to be compacting in one dimension only (uniaxial deformation). Jacob's parameter idealized the loading situation as being in static equilibrium, where the surface loading is balanced by forces generated by the compression of the soil skeleton and the pore fluid. Jacob derived his parameter and named it after the specific phenomenon he was observing. This phenomenon involved the rise and fall of the ocean tide as a transient, rapidly applied load on the

aquifer. Naturally he named this parameter “tidal efficiency” suggesting that the ability to transmit loading to the water within the porous media is a measure of “efficiency” (Ferris, 1951; van der Kamp and Gale, 1983; Domenico and Schwartz, 1990).

The increase in pore pressure due to an increase in surface loading is also a phenomenon that is important to the geotechnical engineering community. Typical applications involve problems of building or embankment construction where a load is rapidly applied to a soil of low hydraulic conductivity such as clay. It is essential that the pore pressure increase be understood so that its dissipation can be modeled and any associated settlements can be predicted. In the 1950’s the British geotechnical engineer, A.W. Skempton set out to describe this phenomenon mathematically, as Jacob did for his problem, but within the civil/geotechnical engineering community. It is not known how familiar Skempton was with the work occurring by hydrologists such as Jacob, but fundamentally the two were trying to explain the same physical phenomenon.

Skempton derived his expression through laboratory triaxial tests where he defined his pore pressure parameters by considering the forces shown in (Figure 5). This figure illustrates that for a closed control volume that allows no drainage, the external force and associated stress is balanced by a resisting force from the fluid filling the pore space and a force from the soil skeleton. Skempton defined his pore pressure parameters by considering the direction of loading and how a sample of soil in a triaxial cell is restrained (Lambe and Whitman, 1969). The two dimensional part of Figure 5 is likely the same situation considered by Jacob when he derived his tidal efficiency term.

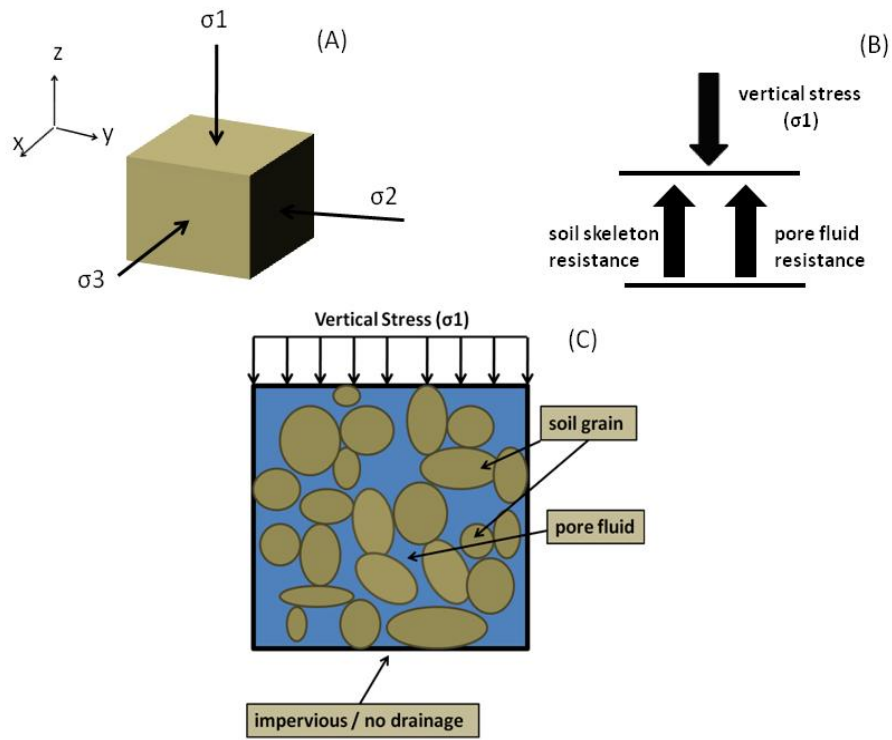


Figure 5. Illustration of the statics and forces used to derive both Jacob's tidal efficiency and Skempton's coefficient. A) three dimensional loading of porous media B) balance of static forces C) two dimensional view of loading.

If one assumes that the sample of soil is perfectly restrained on all sides and deformation can only occur in the vertical (Z) direction, then one can write the following Skempton coefficient:

$$C = A = \frac{\Delta u}{\sigma_1} = \frac{1}{1 + n \left(\frac{\beta_w}{\beta_{sz}} \right)} \quad (8)$$

If one loads an isotropic material with an isotropic increase in stress, one can write the following coefficient in terms of mean stress and compressibility:

$$\sigma_1 = \sigma_2 = \sigma_3 = \sigma_m \quad \text{and} \quad \beta_{s1} = \beta_{s2} = \beta_{s3}$$

$$B = \frac{\Delta u}{\sigma_m} = \frac{1}{1 + n \left(\frac{\beta_w}{\beta_{sz}} \right)} \quad (9)$$

This equation is the same structure as (8) but with the exception that now we have left room to consider the three dimensionality of the problem. A more detailed discussion of Skempton's Coefficient's A-D and their physical meanings for various loading scenarios can be found in most soil mechanics text books and the reader is pointed to Lambe and Whitman (1969).

Another way to arrive at (9) is by considering an expression that will utilize vertical modulus instead of compressibility given that compressibility is simply the reciprocal of vertical modulus. This expression is seen in (10) (Wang 2000).

$$B = \frac{\frac{1}{K} - \frac{1}{K_s'}}{\frac{1}{K} - \frac{1}{K_s'} + n \left(\frac{1}{K_f} - \frac{1}{K_s'} \right)} \quad (10)$$

Equation (10) is widely cited in the poroelasticity literature and constitutes a rigorous definition of Skempton's coefficient. This expression takes into account compressibility of the solids, and fluid along with bulk compressibility, allowing it to represent the three-dimensionality of the loading problem illustrated in Fig 4.

The application of (9) and (10) to actual field problems requires some modifications due to the nature of the physical situation that is occurring. The use of an open well or piezometer to measure a pore pressure fluctuation requires the introduction of a parameter that is assumed to measure strain in a one-dimensional situation only. This means that we are assuming vertical compressibility only and that the medium is undergoing compression while perfectly restrained on the side. This parameter is called the loading efficiency (γ) and is described as:

$$\gamma = -\frac{\Delta u}{\Delta \sigma_1} \quad (11)$$

Loading efficiency has the following strain condition.

$$\varepsilon_{xx} = \varepsilon_{yy} = 0 \quad (\text{uniaxial})$$

Loading efficiency can be directly calculated by taking the ratio in height of the well or transducer pressure fluctuation to that imposed by the surface loading event after factoring out other signals (such as barometric fluctuations). Whether the units of this ratio are in stress (force per unit area) or pressure head remain inconsequential so long as

units remain constant. Often, the surface loading event is the rise and fall of the ocean tide or another phenomenon such as a passing train (Jacob, 1940).

Of course, in geologic problems, perfectly vertical strain / stress changes never occurs because all compression phenomenon have some three-dimensional effects. This presents an interesting conundrum because if we are calculating loading efficiency based on actual field data and those data are derived from the actual real loading event, where three dimensional effects are occurring, then all we have in (11) with its condition is an approximation to Skempton's coefficient. The actual relation between loading efficiency as a uniaxial parameter and Skempton's B coefficient is expressed using bulk modulus, vertical uniaxial modulus and Poisson's ratio as (Wang, 2000):

$$\gamma = \frac{B(1+\nu)}{3(1-\nu)} = B \frac{K_u}{K_v} \quad (12)$$

Because of the complexity and expense in obtaining the parameters in (12) the condition of uniaxial strain is imposed on the practical problem encountered in the field, and both the bulk modulus and the vertical modulus are assumed to be equal. This means that loading efficiency and Skempton's B coefficient are considered equal. This is also equal to the tidal efficiency (T.E.) term of Jacob in (1940). In summary,

$$T.E. = \gamma = -\frac{\Delta u}{\Delta \sigma_1} = B = \frac{\frac{1}{K_v} - \frac{1}{K'_s}}{\frac{1}{K_v} - \frac{1}{K'_s} + n \left(\frac{1}{K_f} - \frac{1}{K_s} \right)} \quad (13)$$

The solid particles of the soil and sediment skeleton can also be assumed to be incompressible which reduces (13) to the equation originally presented by Jacob (1940) and used as the C parameter by Skempton. Equation (13) can be rewritten as:

$$T.E. = \gamma = -\frac{\Delta u}{\Delta \sigma_1} = B = \frac{\frac{1}{K_u^v}}{\frac{1}{K_v} + n \left(\frac{1}{K_f} \right)} = \frac{\beta_s}{\beta_s + n\beta_f} \quad (14)$$

It is also noted by Wang (2000) that for compressible fluids the B coefficient can be expressed as:

$$B = \frac{K_f}{nK_v} \quad (15)$$

These equations (6,12, and 14) represent the basic poroelastic parameters utilized in this thesis. These terms will be incorporated in the larger poroelastic theory and governing equations presented in Chapter 3. These terms will be used in the analytical solutions section and are the primary interest of this thesis.

1.6 Thesis Organization

The thesis will first discuss the field data set (Chapter 2), along with relevant information about how it was gathered. Since the data were recorded in a borehole, information will also be presented about the transducer, the borehole and the immediate geology around it. This data set represents both the tidal fluctuations at the surface and at depth in the South Ellwood fault zone, Monterey Formation, Santa Barbara basin.

The thesis will then inform the reader of the necessary background to utilize a tidal signal propagation/attenuation record (Chapter 3). This theory is interdisciplinary and draws from groundwater hydrogeology, geotechnical engineering/geomechanics, geophysics, oceanography and signal analysis. The primary focus of this presentation is on developing the geomechanics and hydraulic theory. More complete references are available for the oceanography and signal analysis parts.

Next in Chapter 3 the application of the theory is presented through the use of three different analytical models. In Chapter 4 this analysis is followed up by numerical modeling where pressure propagation is modeled through an entire subsurface cross section. Finally, in Chapter 5, the results and applicability of the analytical solutions and numerical modeling are discussed along with implications for the active extraction of oil and gas from within the study area. This section contains an estimate of the hydraulic and mechanical properties of the fault zone.

Chapter 2: Data and Platform Holly

2.1 Overview

Much detail is known about the geology of the Santa Barbara basin thanks to the efforts and sharing of knowledge by various companies in the oil industry. The data set utilized here was recorded by Venoco Inc on Platform Holly which Venoco owns and operates in the Santa Barbara Channel. The current reservoir operations by Venoco will be described in their relation to the data set. This discussion will also include information on Well #13 which is the source of my field observations.

2.2 Venoco Inc., Platform Holly, South Ellwood Field

Venoco Inc is a smaller oil and gas development company that operates in California. The company currently has operations in the Santa Barbara Channel and the Sacramento Basin. The company's operation in the Santa Barbara Channel consist of operating three offshore oil and gas production platforms called Gail, Grace and Holly. Each of these platforms is currently exploiting a different oil and gas field within the channel. Platform Holly is situated above the South Ellwood oil field and 2 miles from shore near the University of California Santa Barbara campus. The platform sits in 211 feet of water and was originally built in 1966 and operated by Mobil Corporation. Venoco acquired this platform in 1997 and has been operating it since (www.venocoinc.com).

Platform Holly is situated on the northern side of the Santa Barbara Channel and is positioned above a series of anticlinal/synclinal structures that strike east to west along the north coast of the channel (Heck, 1998; Tennyson and Kropp, 1998). The typical

stratigraphy consists of the Rincon Formation overlain by about 1500 ft of the Monterey Formation, capped by about 3,000 ft of the Miocene-Pliocene Sisquoc Formation (Figure 2). As noted in Chapter 1 each of these units is lithologically complex, reflecting the complex depositional history in the Santa Barbara basin. It is not uncommon to find assorted mixtures of shale, sandstone and conglomerate existing in each formation. The Sisquoc Formation is generally a relatively impervious mudstone while the Rincon is a mudstone with sandy layers in the upper part.

The Monterey Formation is the primary target formation for oil and gas drilling near Platform Holly. This formation also displays a complex stratigraphy and is broken up into multiple intervals for distinct classification. The USGS quadrangle map breaks the formation into three zones while the petroleum industry further subdivides it into seven zones. Each zone is distinguishable by the presence of hydrocarbons, mineralogy, and changes in electrical resistivity and natural gamma observed during geophysical logging. The Monterey Formation is significantly fractured which is believed to account for much of the effective porosity and permeability. The formation is generalized as a fractured shale. This is consistent with other geologic observations elsewhere in the Santa Barbara basin (Galloway, 1998; Heck, 1998; Minor et al., 2007).

Figure 6 below illustrates the stratigraphy beneath Platform. This figure shows the location of Well #13 where the data for this thesis was gathered from while Figure 7 shows the detailed construction of Well #13. Figure 6 also shows the location of the fault zones that have laterally compartmentalized the oil and gas reservoir. These fault zones are of great interest since they are believed to be active conduits for the vertical leakage seepage of oil and natural gas to the sea floor and are responsible for the large amount of natural seepage seen in the channel. These faults are also the faults on which the large seep tent structures were constructed (Boles et al., 2001). These faults represent the

hydraulic conduits which would allow communication between the Monterey Formation at depth and the sea floor in terms of pressures and the transmission of fluid.

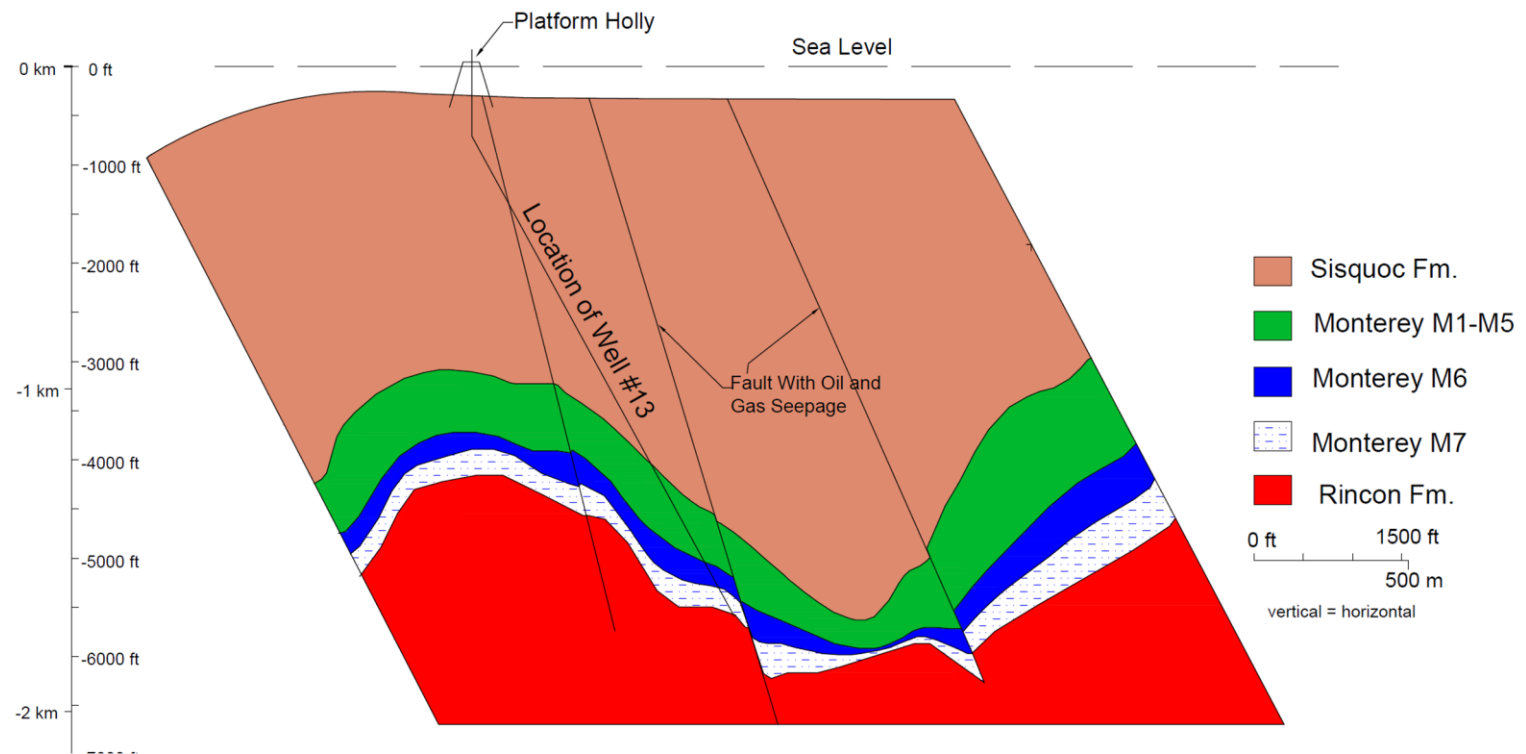


Figure 6: Cross section below Platform Holly showing Well #13, faults and stratigraphy. Re-drawn with permission of Venoco Inc.

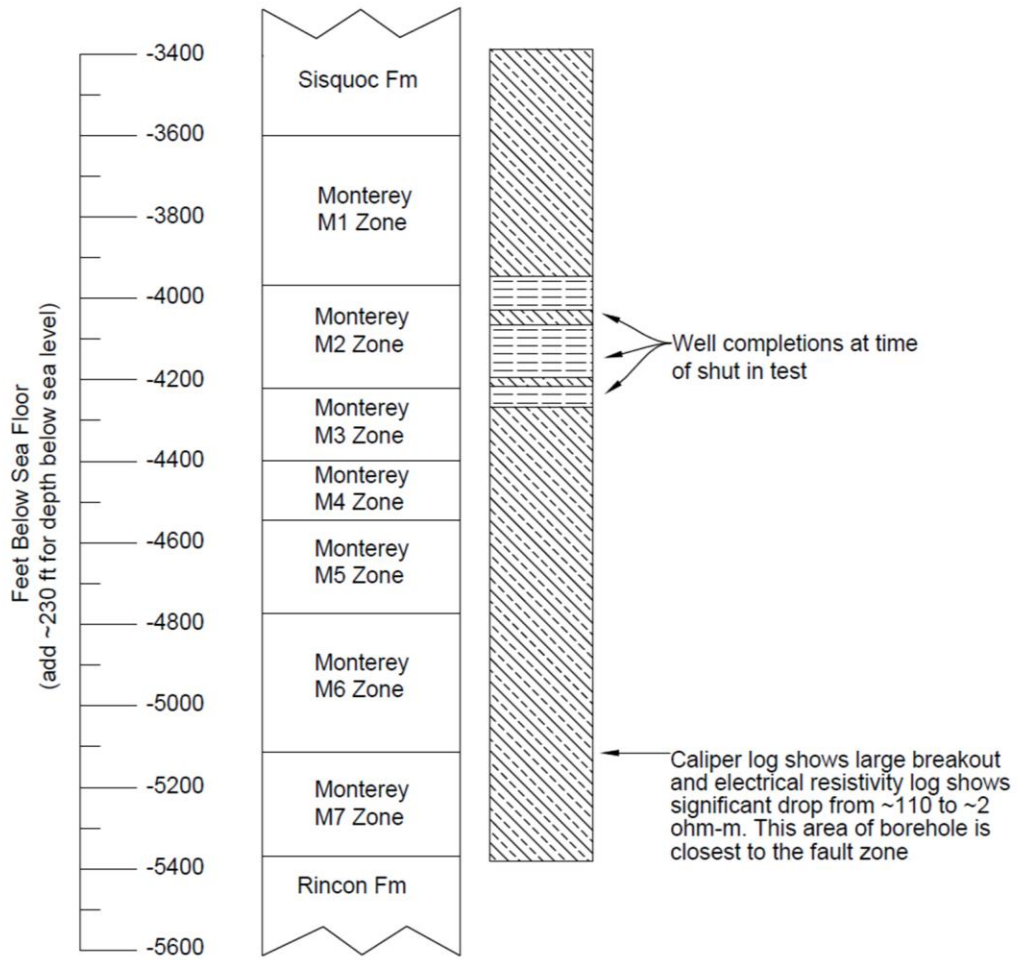


Figure 7. Details for Well #13 showing completions with stratigraphy and notes about electrical resistivity. Re-drawn from information provided by Venoco Inc.

2.3 Well #13 Data Set

Starting on November 26, 2001 a routine test was conducted on Platform Holly to monitor pressures during a 14 day “shut in” period when the active removal of oil and gas from the reservoir was ceased. During this time period the pressures were monitored in five different boreholes around Platform Holly. The pressure monitoring was conducted using Kuster K10 quartz crystal pressure sensors that are an industry standard for this type of work. Typically these borehole pressure sensors are about 9 ft long when combined with data recording system, battery, and delivery platform. These sensors are designed to work at temperature in excess of 300 deg F (150 C) and pressures above 10,000 psi (68.9 MPa) which are often found in oil reservoirs. This type of system uses a single quartz crystal to measure both temperature and pressure. The Kuster Company is an industry provider of this type of technology and more information can be seen at www.kusterco.com.

During this monitoring period the reservoir pressures were seen to increase since production was halted and formation fluids relaxed. While most of the sensors in operation exhibited expected behavior the pressure record in Well #13 was unusual in that it showed an oscillation of the pressure around the expected pressure increase. The raw data of this record is shown in Figure 9. This plot does not alter the data in any way and shows the pressure spike and drop at either end that are associated with instrument calibration and are expected. This data was provided by Professor James R. Boles of University of California Santa Barbara (UCSB). If the pressure spike and dramatic pressure decrease associated with instrument deployment and calibration are factored out of the signal and the pore pressure is plotted in terms of pressure head using a unit weight of 62.4 lb/ft^3 , the result is seen in Figure 10. The ocean tidal signal recorded at the Santa Barbara tidal station for this interval of time is illustrated in Figure 10 (Boles, 2012).



Figure 8: Kuster gauge
(www.kusterco.com/pdfs/2012/Probe_Kuster_K10_Quartz_XT.pdf)

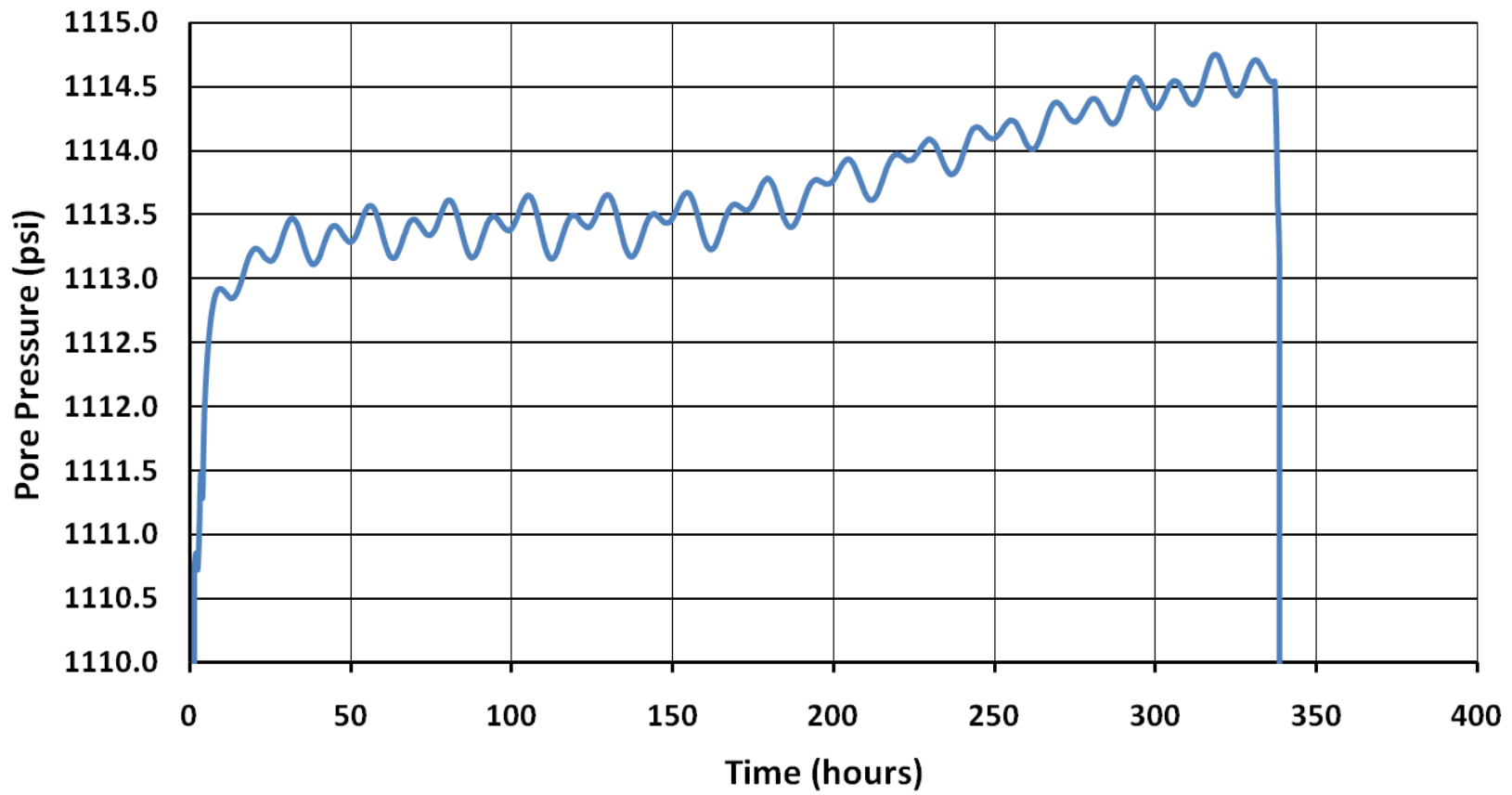


Figure 9: Sensor pressure data recorded at 5,000 ft below sea level in Well # 13.

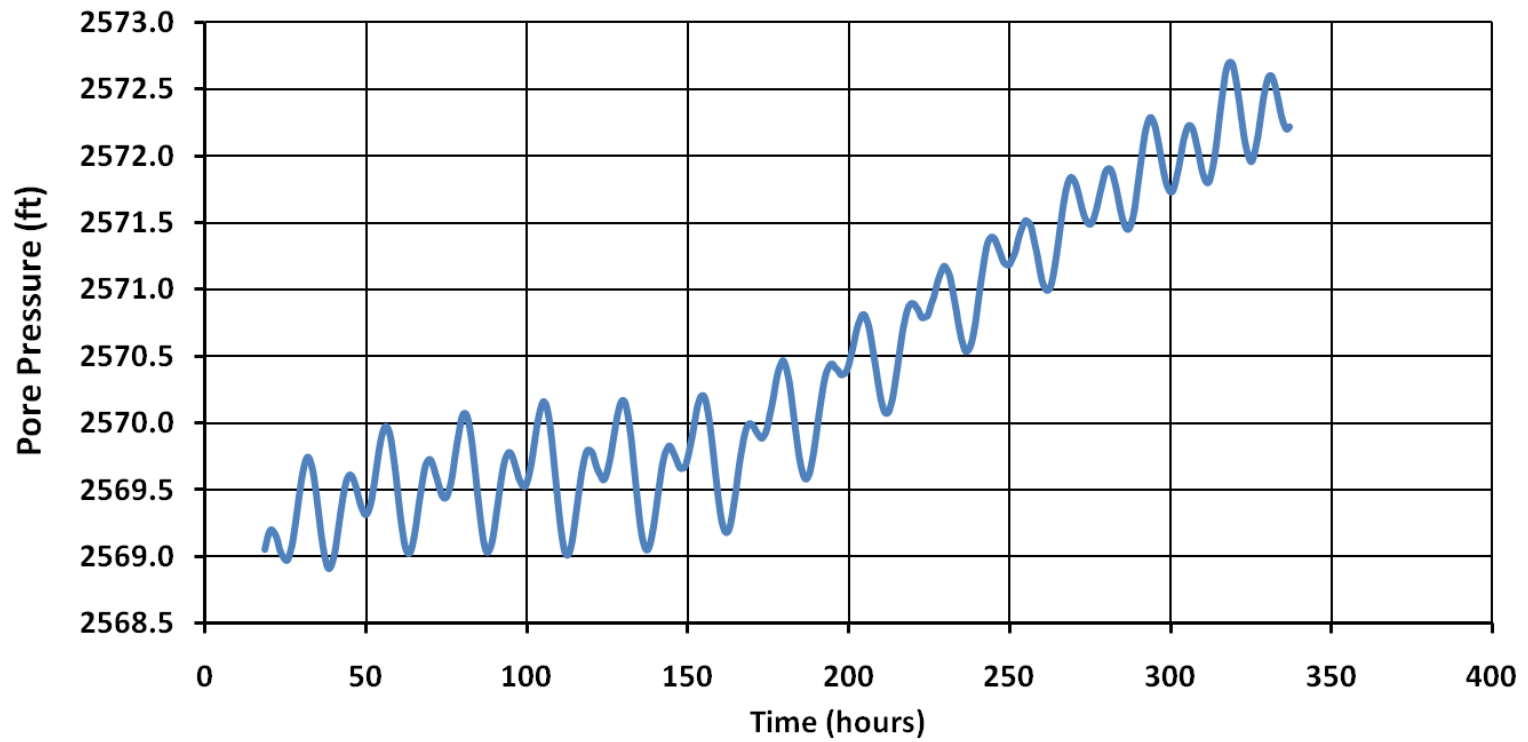


Figure 10: Pressure head signal at depth without instrument calibration.

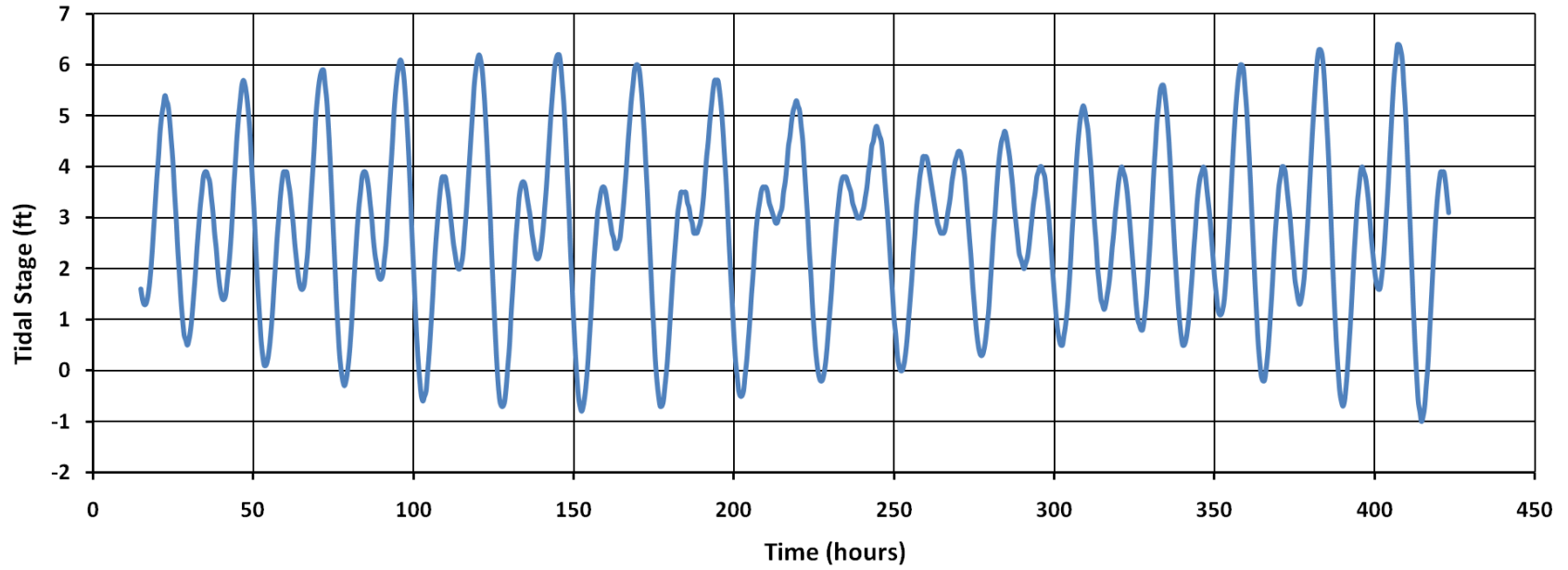


Figure 11: Tidal signal corresponding to the same period of time as pressure signal at depth.

2.4 Summary

This chapter presented the subsurface data set that is to be analyzed in Chapter 3 along with important considerations about how the data was gathered and the immediate geologic environment surrounding where it was gathered. The synthesis of this section is that a unique pressure signal was gathered at a depth of 5,000 ft below sea level in a borehole (well #13) that was part of Platform Holly. This pressure signal is assumed to be a subdued version of the tidal signal and this correlation will be explored more in the next chapter. Given the knowledge of the subsurface geology surrounding the borehole, the hydraulic nature of fault zones discussed in the literature review, and the knowledge that the well completion seen in Figure 7 is near the fault zone, it is assumed that the pressure signal seen in this pressure data is being transmitted via the fault zone. This feature is explored and analyzed further in the next chapter.

Chapter 3: Signal Analysis and Analytical Solutions

3.1 Overview

The objective of this analysis is to calculate many of the poroelastic quantities defined in Chapter 1. This calculation is accomplished through the use of three different analytical solutions that have been proposed by various researchers from the hydrogeology and geotechnical engineering communities. The results of this analysis are summarized at the end of the chapter and the reader is referred to the list of symbols in chapter one for a definition of parameters and variables.

The use of the poroelastic theory and analytical solutions require that the tidal and pressure data signal seen in Figures 10 and 11 be resolved into a series of simple sinusoidal signals. This requires that the tidal and pressure signal be investigated and analyzed with an understanding of the science behind ocean tides. This investigation also requires the use of signal analysis techniques that will allow both the tidal signal and the pressure signal to be decomposed into its different constituent frequencies. This chapter will first provide a brief discussion of ocean tides before applying basic signal analysis techniques that will be used to decompose the signal. In addition to determining the amplitudes and phase of each constituent, signal analysis will also be done on both the tidal signal and the signal at depth to show that they contain the same frequency. The signal analysis techniques are familiar to the oceanography community and any introductory text in the analysis of tides should provide an even more in-depth discussion than what is here. A useful example is in the textbook by Fante (1988).

3.2 Tidal Theory

The task of understanding, analyzing and predicting the rise and fall of the tide goes far back into recorded science history at least to the 1600's if not further (Ippen, 1966). The casual observer standing on the shore will notice that the tide will rise and fall two times per day. If the tidal record is recorded and plotted out (e.g. Figure 11) then one will also noticed that the signal is not perfectly sinusoidal and that the amplitudes of the wave will vary somewhat between cycles. This is not always the case in every part of the world where the rise and fall of the tide happens once a day while in other locations a mixed phenomenon occurs. The rise and fall twice daily is called the semi-diurnal tide while the rise and fall once daily is called the diurnal tide. The tidal signal seen in Santa Barbara harbor in Figure 10 is a mixed semi diurnal signal though the general trend seen in Figure 10 is of a twice daily tidal fluctuation.

In 1687 Isaac Newton was the first scientist to develop an accurate theory of tides that explained the phenomenon as due to the interaction of the gravitational forces of the sun and moon on the Earth. The Earth and the Moon both rotate around the Sun and the Moon rotates around the Earth. If one considers this system in motion the Earth experiences two tidal bulges where water is being pulled outwards. These two bulges are on opposite sides of the Earth. One bulge is due to the gravitational attraction of the moon and the other bulge is due to the inertial force on the water as it is pushed to the outer edge of the planet due to its rotation. Depending on the alignment the sun also contributes to the gravitational bulge though, in varying amounts.

Since the direction the Earth spins is the same direction of the moon's rotation around the earth any given point on Earth will experience a tidal signal that is not exactly the same from day to day. This effect is also added to by the fact that the Moon, Sun and earth will align in a different arrangement from day to day. Figure 12 below which shows

the alignment of the planets required to cause extremely high and low water levels known as spring tides along with tidal bulges present on the earth (Ippen, 1966).

The result of the dynamic interactions between the spinning of the planets, their relative rotations and declination to one another, is that the observed tidal signal from any given location on the Earth is not a simple sinusoidal frequency. The signal is seen to increase once or twice a day and wax or wane from amplitude to amplitude. The signal is a composition of a series of different signals or harmonic constituents and each constituent is due to some aspect of this dynamic system. While there are 56 harmonic constituents that make up the ocean tide, there are five basic constituents that account for about 95% of the signal. The five basic are the K_1 , M_2 , S_2 , O_1 & N_2 constituents and out of these the K_1 & M_2 are typically most pronounced in the signal and can be resolved from the tide record accurately with a 15 day signal (Emery and Thompson, 2001) Table 1 below shows the five basic constituents and their frequencies along with an explanation of their cause. These values are taken from Merrit (2004), though they are widely published in a variety of sources including many introductory texts on oceanography.

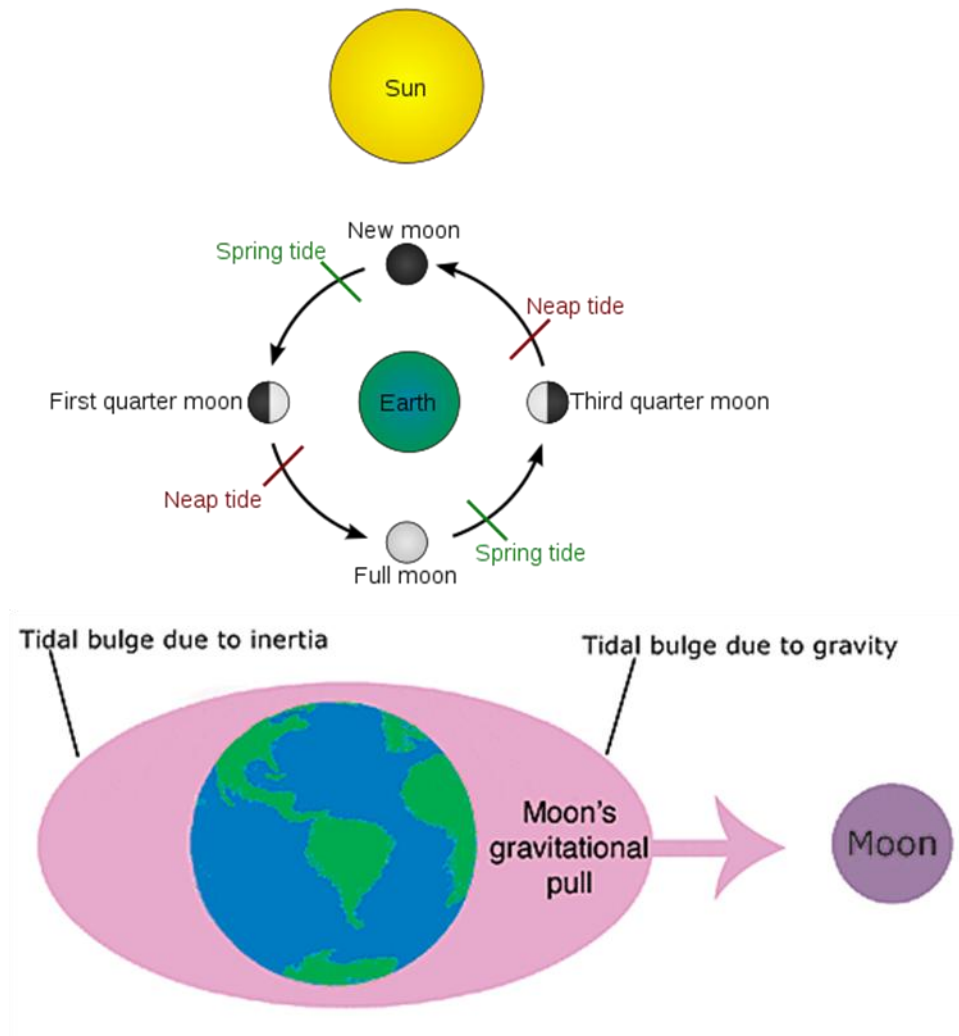


Figure 12. Positions of Moon and Earth at spring and neap tides. Lower figure illustrates tidal bulges from gravitational pull of the moon and inertial forces. (www.en.wikipedia.org/wiki/tide and www.oceanservice.noaa.gov)

Table 1. Frequencies for basic harmonic constituents in the primary ocean tides on Earth.

Constituent	frequency (cycles/day)	frequency (cycles/hour)	Period (hours)	Cause
K ₁	1.00273794	0.041780748	23.93446886	Lunar-solar diurnal
M ₂	1.93227356	0.080511398	12.42060156	Main lunar semidiurnal
O ₁	0.92953574	0.038730656	25.81934074	Main lunar diurnal
S ₂	2	0.083333333	12	Main solar semidiurnal
N ₂	1.89598199	0.07899925	12.65834809	Lunar elliptic (moon's distance)

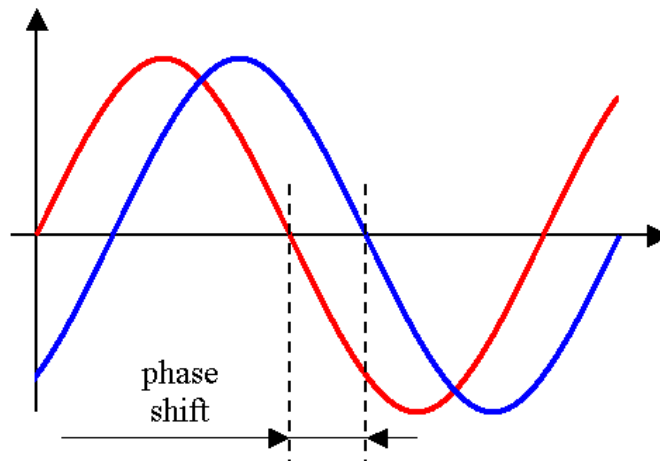
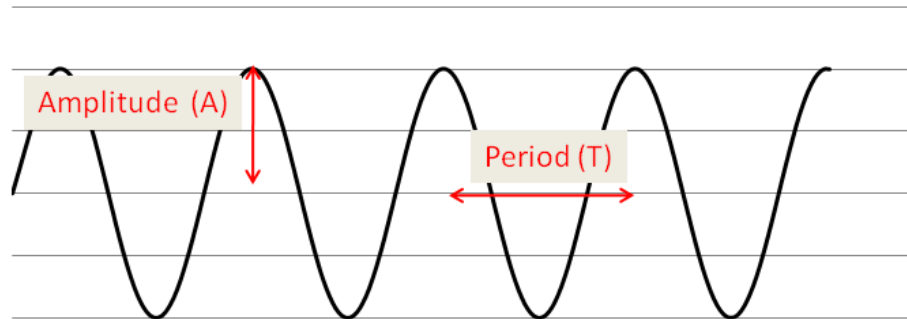
The frequencies determined for each of the constituents are the result of many hundreds of years of observation and recording. These frequencies remain constant in the tidal signal though there amplitudes and phase angle vary from location to location. In order to re-construct or predict the tidal signal in any location one must have the frequencies listed above along with the amplitudes and phase angles. With the amplitudes and phase angles the signal can be reconstructed as the sum of all five constituents or sinusoids. The determination of these constituents from the Santa Barbara Channel tidal signal will be presented in the following section.

3.3 Analysis of the Tidal Signal

3.3.1 Fourier Analysis

The presence of a sinusoidal signal means that there is at least a frequency (f) and amplitude (A) in the signal. A more complex signal (such as the tidal signal) can be thought of as summation of different individual signals or sinusoids and each signal will have its own amplitude and frequency. One way to represent a larger signal that is a summation of a series of signals is to represent it in the time domain. This type of

representation is seen in Figure 11 where tidal stage height vs. time is recorded. This type of representation does not illustrate very much about the individual frequencies, which do not stand out in the composite signal.



$$\Delta\phi = \omega t_1$$

Figure 13: Components of a sine wave. Bottom figure from en.wikipedia.org/wiki/phase_waves.

It is more valuable on occasion to have a plot that will show the individual frequencies contained with a larger signal and be able to rank or display their importance and contribution to the larger signal. This type of representation is done in the frequency domain where the signal is deconstructed into its different frequencies and the overall contribution of any one given signal to the larger composite can be seen. The mathematical technique that allows one to go from the time domain to the frequency domain is based on the application of the Fourier transform (Fante, 1988). If one imagines a signal in the time domain $y(t)$, which we wish to convert into the frequency domain $Y(f)$, then the two transforms are available for the continuous deterministic signal are (Fante, 1998; Emery and Thomson, 2001).

$$Y(f) = \int_{-\infty}^{\infty} y(t)e^{-i2\pi ft} \quad (16)$$

$$y(t) = \int_{-\infty}^{\infty} Y(f)e^{i2\pi ft} \quad (17)$$

The application of (16) to a real data sets require that the equation be expressed in terms of a signal that is collected as a discrete series of data points. It is often the case that the collection of data is done at a regular interval Δt for a total number of N samples of n integers with values y_n . This yields a new equation that is the discrete Fourier transform representation with the integral replaced by a summation:

$$Y(f) = \Delta t \sum_{n=1}^N y_n e^{-i2\pi fn\Delta t} \quad (18)$$

This equation can be used to create a plot showing the contribution of a given frequency on the y axis and the frequency on the x axis. Since this method is

computationally intensive the fast Fourier transform (FFT) was developed (Fante, 1988). This method involves breaking the time domain signal into two half sine waves and conducting a discrete summation that is similar to (18). The procedure for this operation can be found in most signal analysis books and the reader is directed to discussions Fante or Emery and Thomson (2001) for a more detailed description of the procedure. Equation (18) can be squared to provide an estimate of the energy spectral density and when this is done the ensuing plot is referred to as a “periodiagram” and is the preferred way of conducting this type of analysis within the oceanography community (Emery and Thomson, 2001).

3.3.2 Least Squares Harmonic Regression

The Fourier transform is a useful technique to find individual frequencies within a larger signal. This technique is applicable when nothing is assumed about the data set and one wishes to merely see what frequencies are present or make a correlation between two different records showing the same frequencies. This is not the case in the problem of tidal analysis where (through historical observation) the frequencies of all the tidal constituents seen in Table 1 are known. The problem in tide prediction or tidal signal reconstruction is not to determine the frequencies but to determine the amplitudes and phase angle of each harmonic constituent. Since a record of nearly a year is needed to reconstruct the signal using all 56 constituents and their associated frequencies, it is more convenient to use only the five major constituents noted in Table 1 imposed on a shorter record. The problem is that because the longer record contains the influence of all 56 constituents and because there are more data points than frequencies, the problem is over determined. The method of least squares allows this error to minimize and an appropriate

estimate of phase angle and amplitude to be determined (Emery and Thomson, 2001).
The basic equation for this regression with M constituents/frequencies is:

$$x(t_n) = x_{av} + \sum_{q=1}^M C_q \cos(2\pi f_q t_n - \phi_q) + x_r(t_n) \quad (19)$$

$$x(t_n) = x_{av} + \sum_{q=1}^M A_q \cos(2\pi f_q t_n) + B_q \sin(2\pi f_q t_n) + x_r(t_n) \quad (20)$$

Where the term x_r is the residual error, x_{av} is the mean value, C_q is the amplitude and ϕ_q is the phase angle of any individual constituent. This method seeks to minimize the residual error by expanding the error term and taking the derivative of that error with respect to A_q and B_q terms. This allows for a series of simultaneous equations to be set up and placed into a matrix form allowing the amplitude and phase angle for each constituent to be calculated. The total signal can then be recomposed in accordance with (18) and (19) and be compared with the original record (Emery and Thomson, 2001).

3.3.3 Application of Signal Analysis Methods

The first step in the application of both the Fourier analysis and the least square harmonic regression was to de-trend the raw data seen in Figures 10 and 11. The tidal signal recorded in Figure 11 was relatively easy to de-trend and simply involved subtracting out an average value from the data set that would bring the signal down to the x axis. The pressure signal recorded at depth seen in Figure 10 was somewhat more difficult due to the expected ramp up in pore pressure being present in the signal. By

inspection of the plotted data in Figure 10 this ramp up has two components that appear to be very linear in nature and this was taken advantage of in de-trending the data. An equation was written for each linear part of the data set and then subtracted from the data to bring the signal down to the x axis. The results of this procedure can be seen in Figures 14-16.

Once the data was de-trended it was possible to apply a Fourier analysis (transform) to see the constituent frequencies in both the tidal signal and the signal at depth. The point in applying the transform is to demonstrate and verify that the same frequencies seen in the ocean tidal signal are also present in the formation pressure signal recorded at depth. The pressure signal at depth being a reflection of the tidal signal might appear obvious by inspection (Fig. 16) and the transform is applied to provide a mathematical basis for this observation. The transform is seen in Figure 17 below and was accomplished by using the commercial software MATLAB and the FFT (Fast Fourier Transform) function.

After applying the Fourier transform and demonstrating that the signal recorded at depth displays the same frequencies seen in the tide, the least square harmonic regression was applied to determine the phase angle and amplitude of each of the five harmonic constituents. This analysis was completed using the World Tides software program developed by Boon (2007). This program was written in MATLAB and utilizes a user friendly GUI interface to input the tidal data. The program is freely available to the public and can be downloaded from the MATLAB file share website (Boon, 2007).

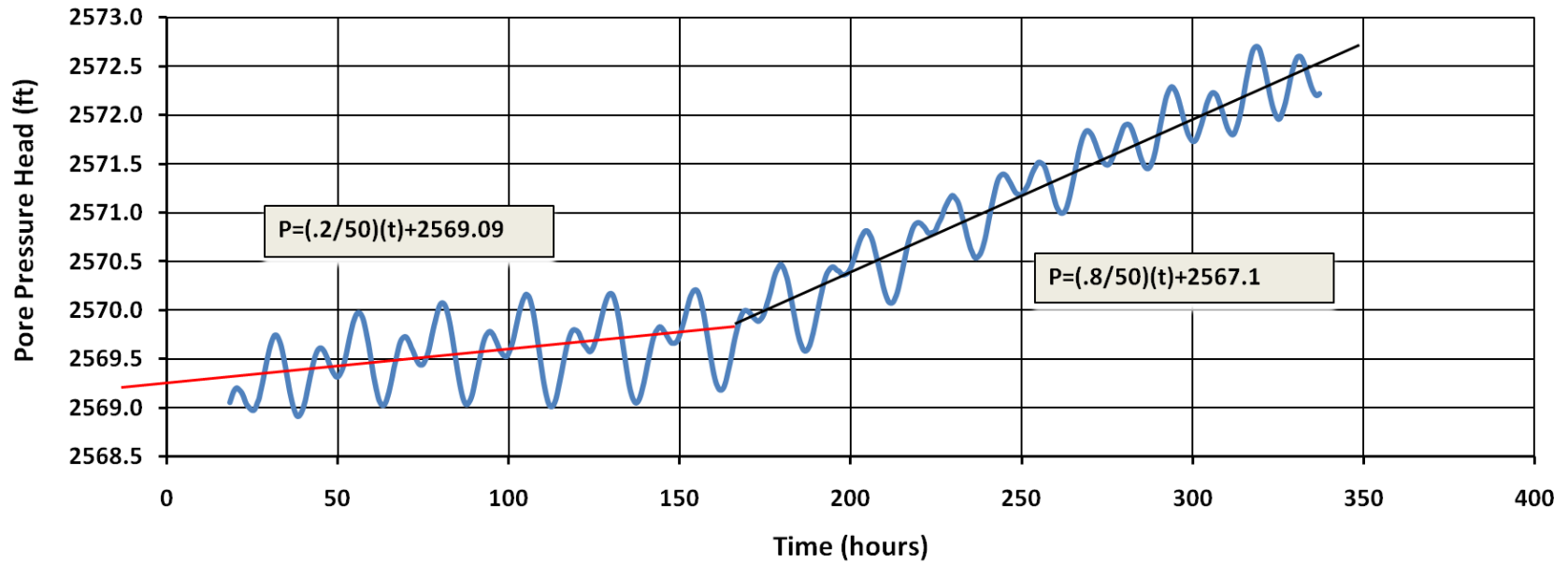


Figure 14: Straight lines and equations used to de-trend data set for pressure signal at depth. It should be noted that original data reduction technique was done by Ms. Carley Petterson working with Prof. James R. Boles of USCB. This work utilizes a slightly different linear equation and expresses formation pore pressure in terms of pressure head.

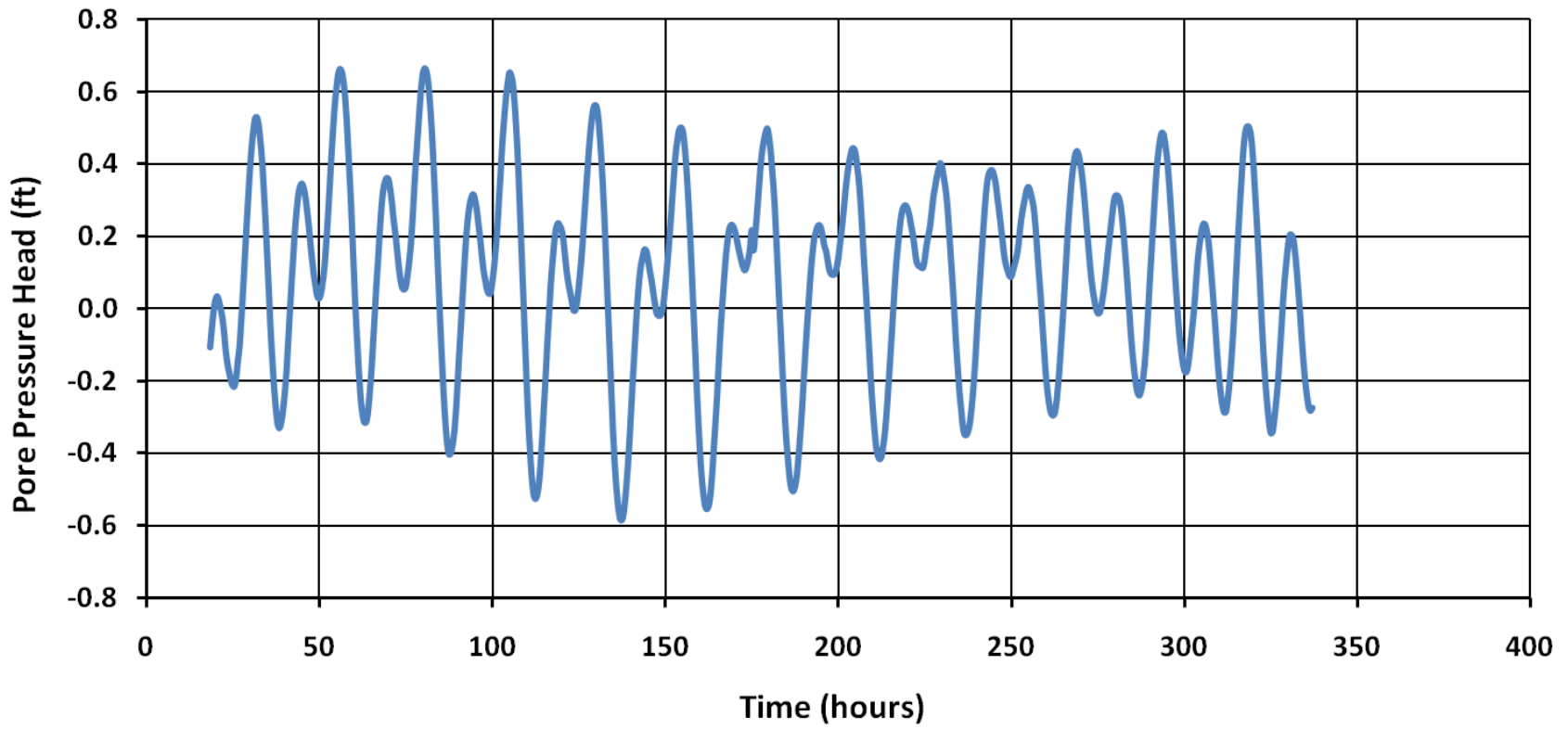


Figure 15: De-trended pressure signal at depth.

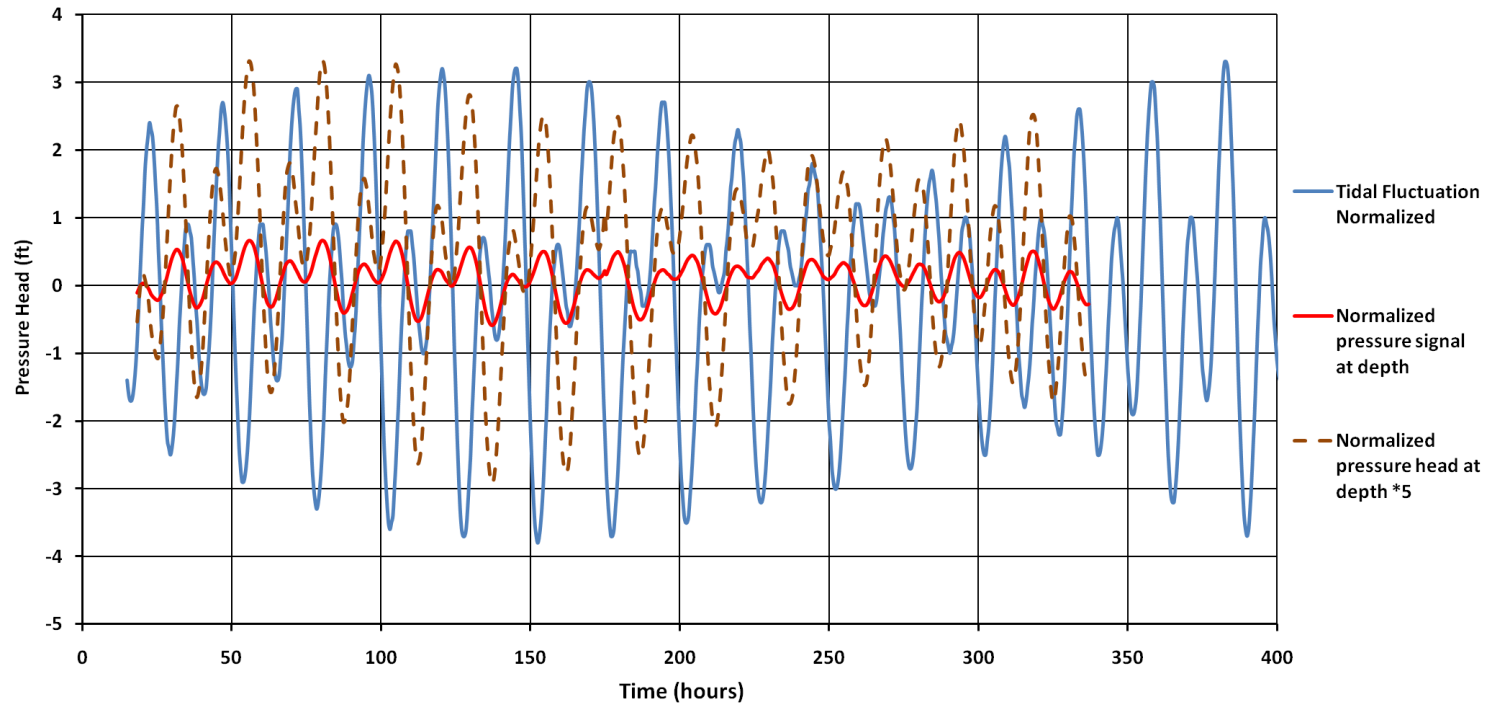


Figure 16: Plot of de-trended tidal signal and pressure signal at depth. The dashed line is the pressure signal multiplied by an arbitrary scaling factor of 5 to further illustrate its relation to the tidal signal. Original data reduction technique was done by Ms. Carley Petterson working with Prof. James R. Boles of UCSB.

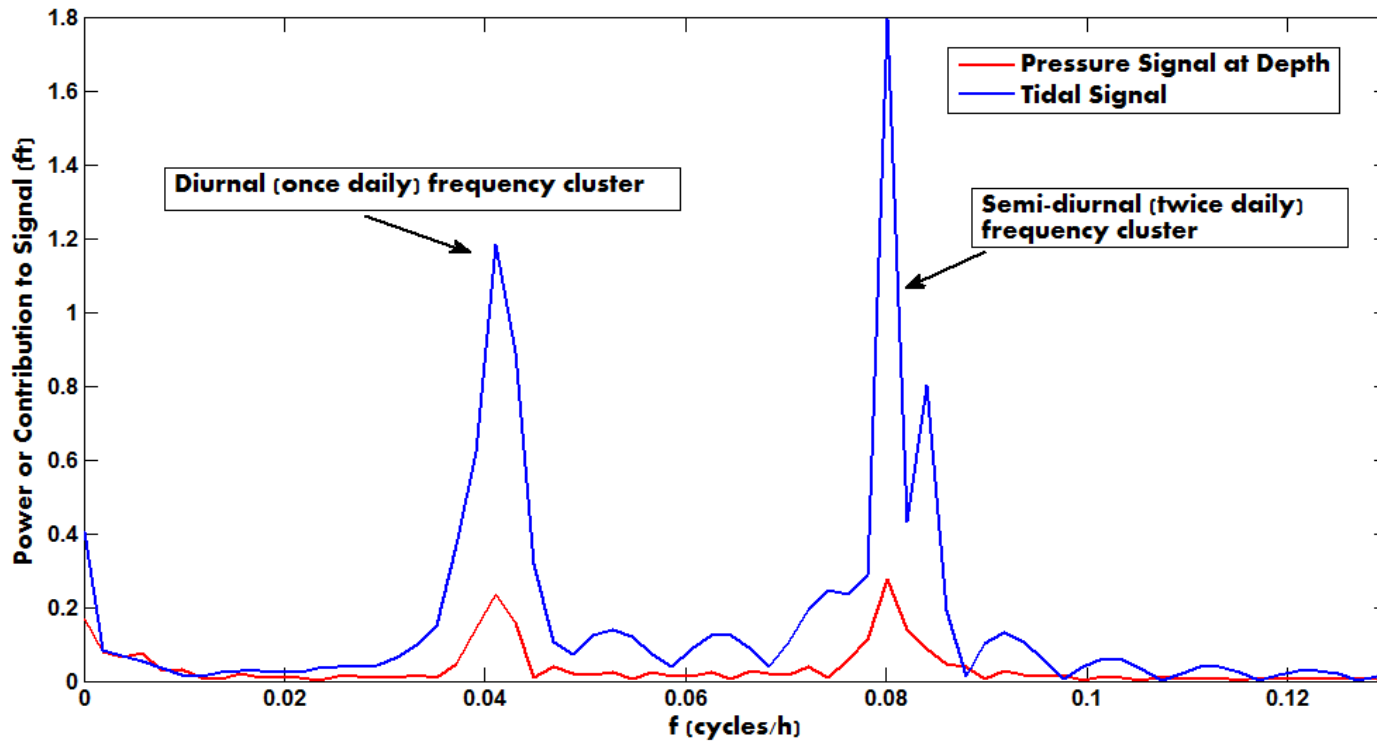


Figure 17. Frequency spectrum for both tidal signal and pressure signal at depth illustrating that the frequencies seen in the tidal signal are also seen in the pressure signal at depth.

The World Tides program allows for the basic five tidal constituents to be imposed on the data, and from a determination of the amplitude and phase of each constituent, the total signal can be re-composed by summing all five constituents together. This calculated or astronomic signal can then be plotted on the same graph with the observe signal to see how well the least square regression did in determining the amplitude and phase of each constituent. The difference or “residual” between the observed and the calculated can be viewed as an estimate of the final error in the processes. Plots of the analysis were constructed of both the tidal signal and the formation pressure signal at depth and show the residual between the observed signal and the reconstructed or astronomic signal (Figure 18 and 19).

Table 2 shows the amplitudes and phase angle computed by the least square regression for both the tidal signal and the pressure signal. This table also compares the values to those provided by the U.S. National Oceanic and Atmospheric Administration (NOAA) for the Santa Barbara Station. No phase angle is compared for the Santa Barbara Station because the phase angle depends on the point in time when the instrument started recording. There is a small difference in the amplitude values because of the short length in the tidal signal utilized in this study and that recorded by the NOAA station which utilizes 56 constituents.

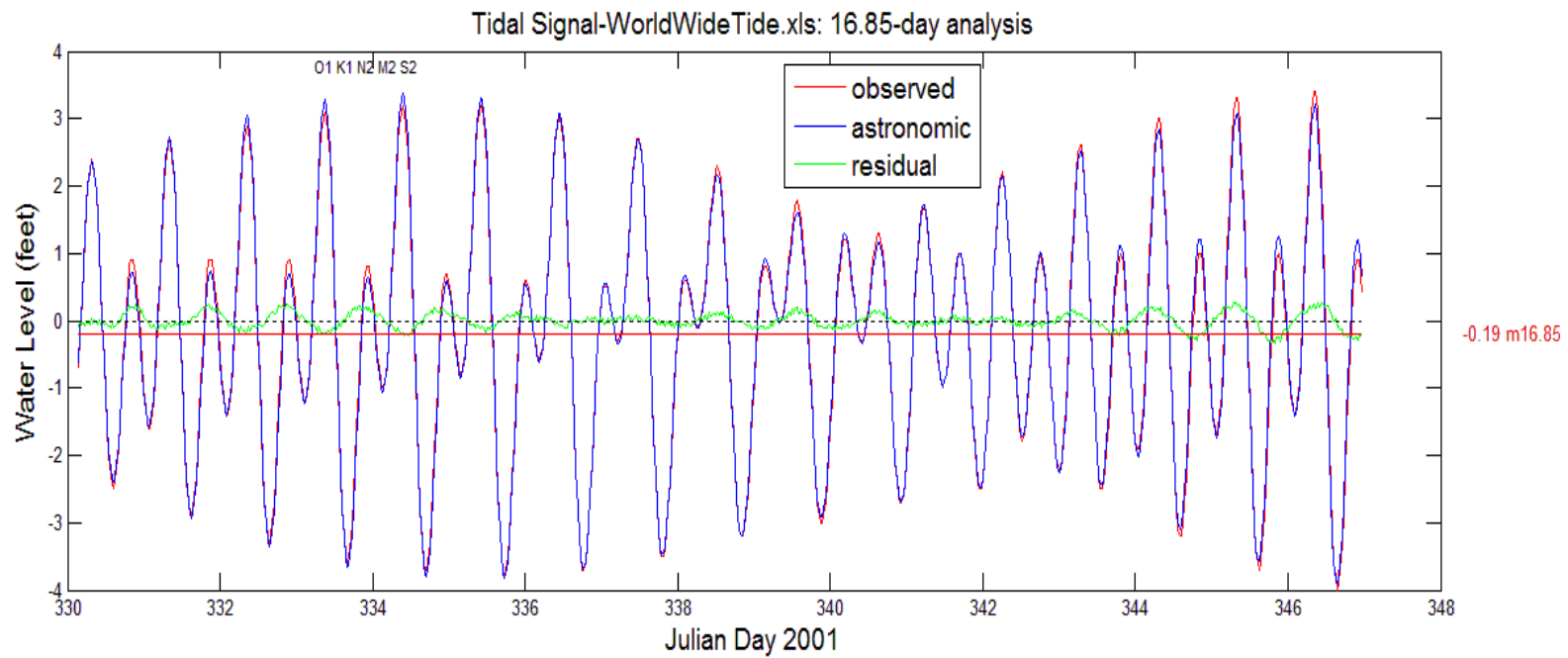


Figure 18. Graphical result of least squares harmonic regression on tidal signal with amplitudes and phase angles seen in Table 2.

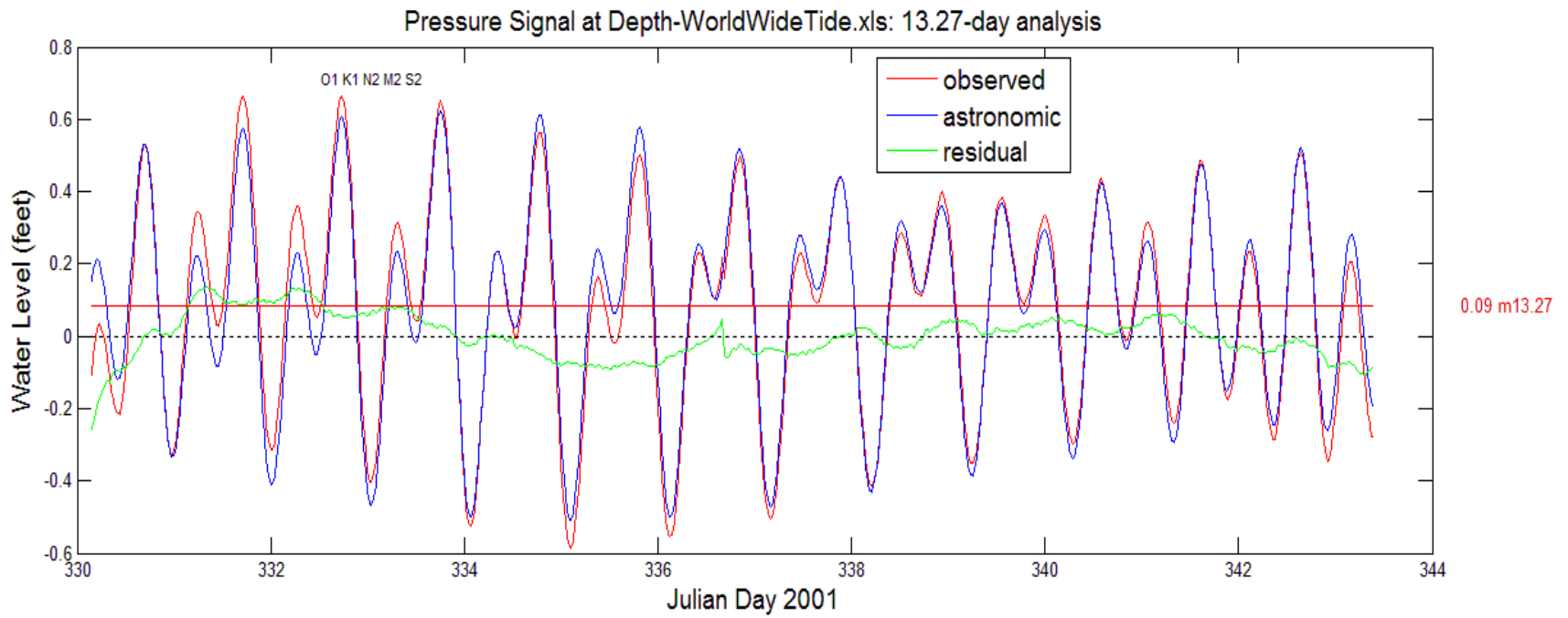


Figure 19. Graphical result of least squares harmonic regression on pressure signal at depth with amplitudes and phase angles seen in Table 2.

Table 2. Result of least squares harmonic regression with amplitude comparison to Santa Barbara Station.

	Tidal Signal Platform Holly	Pressure Signal At Depth	Santa Barbara Station (tide)
K ₁ Amplitude (ft)	1.392	0.231	1.145
K ₁ Phase φ (deg)	81.7	207.17	N/A
M ₂ Amplitude	1.594	0.249	1.572
M ₂ Phase φ (deg)	271.26	188.32	N/A
O ₁ Amplitude(ft)	0.702	0.109	0.745
O ₁ Phase φ (deg)	67.58	203.71	N/A
N ₂ Amplitude (ft)	0.32	0.055	0.377
N ₂ Phase φ (deg)	187.66	119.69	N/A
S ₂ Amplitude (ft)	0.568	0.075	0.548
S ₂ Phase φ (deg)	273.13	174.43	N/A

* N/A = Not Applicable

Table 3. Amplitude ratios for each constituent calculated from Table 2 and least squares harmonic regression. Ratio is amplitude at depth divide by amplitude at surface.

Constituent	Ratio (A_d/A_s)
K ₁	0.1659
M ₂	0.1562
O ₁	0.1553
N ₂	0.1719
S ₂	0.1320

3.4 Analytical Solutions

3.4.1 Skempton's Loading Efficiency

The first and simplest model to apply to the data set and the amplitudes calculated in Table 2 and 3 is that of Skempton's. This model assumes that no fluid is allowed to flow in or out of the control volume and that any applied loading is balanced by the pore fluid and soil skeleton (Figure. 5), according to Terzaghi's Law. The application of Skempton's coefficient (B value) to this data set will be called loading efficiency or tidal efficiency since we are measuring a phenomenon in the field. Equations (12)-(15) will be applied for this analysis with equation 12 being used to express loading efficiency in terms of Poisson's ratio.

The application of equation (12) requires one to take the ratio of the amplitudes seen in Table 2 and use them to solve for the soil modulus assuming a standard value for pore water compressibility. This equation can also take into account various values for Poisson's ratio ν . Equation (12) is plotted out below for various values of Poisson's ratio typical for soil and rock (Figure 20-23). The graph covers a range typical to soil and rock with $44.0 \times 10^{10} \text{ N/m}^2$ being a very strong competent rock such as granite and $6 \times 10^{10} \text{ N/m}^2$ being a weaker mudstone or dense till. These values are taken from the Wang (2000), but are a compilation from various publications. Because the exact Poisson's ratio is not known, it is common to use the uniaxial $\nu = 0.5$ line for calculating the modulus of the tidal ratio. The compressibility of water was taken as $4.4 \times 10^{-10} \text{ m}^2/\text{N}$ (Lambe and Whitman, 1969)

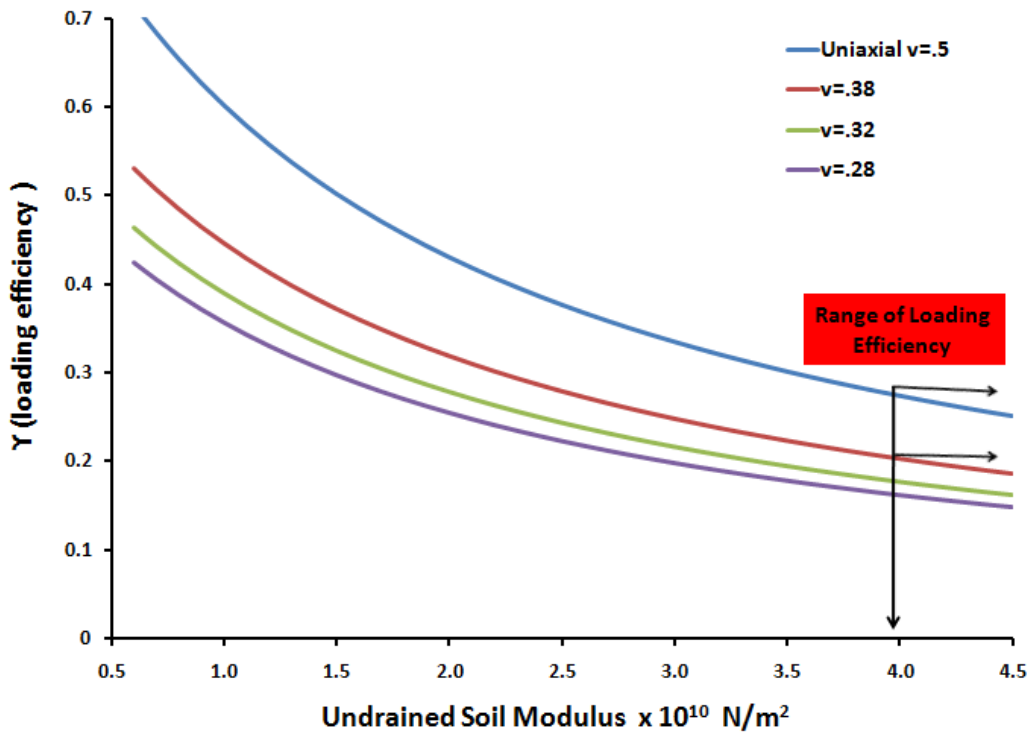


Figure 20. Loading efficiency chart for various common Poisson's ratio assuming pore fluid is water and porosity $n=15\%$.

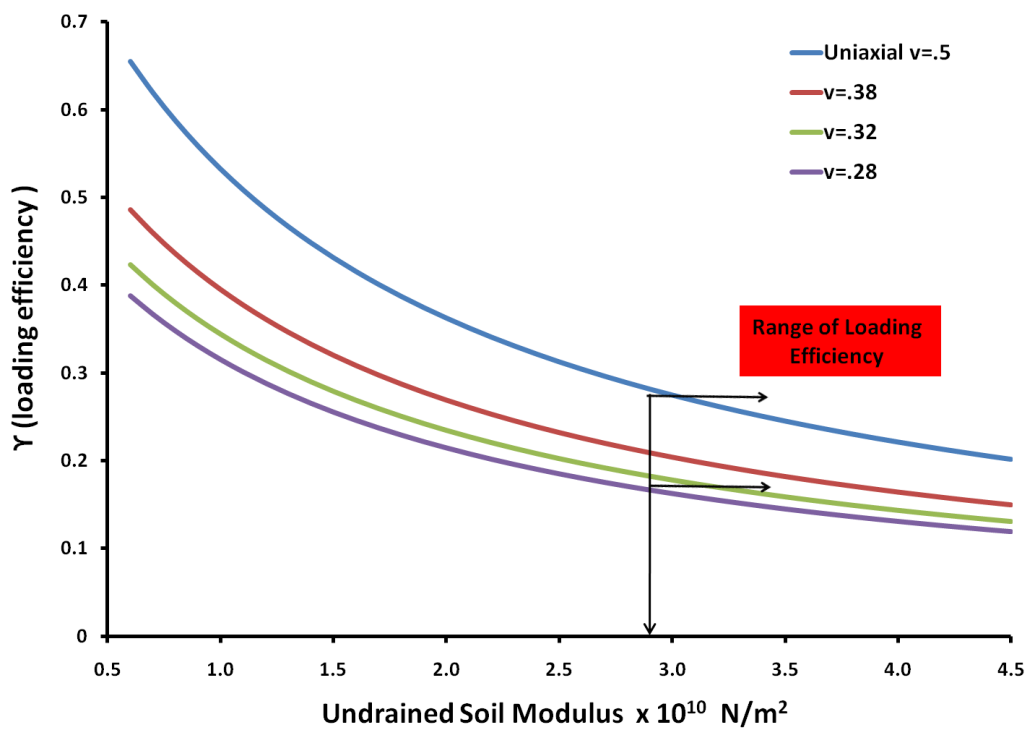


Figure 21. Loading efficiency chart for various common Poisson's ratio assuming pore fluid is water and porosity $n=20\%$.

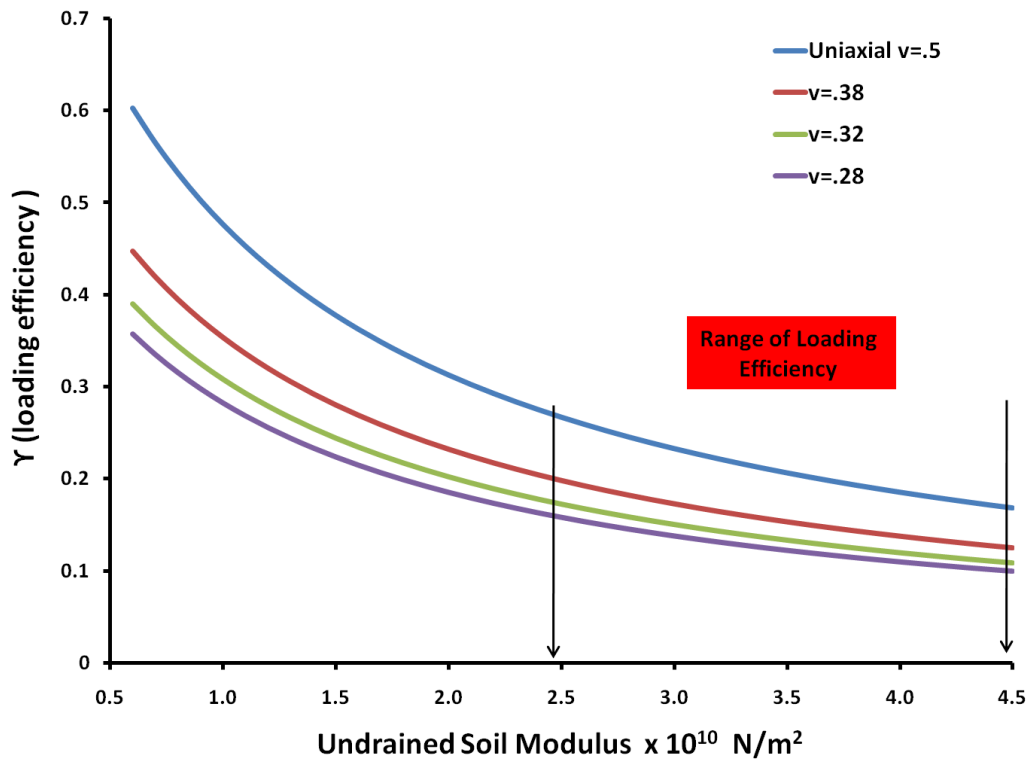


Figure 22. Loading efficiency chart for various common Poisson's ratio assuming pore fluid is water porosity $n=25\%$.

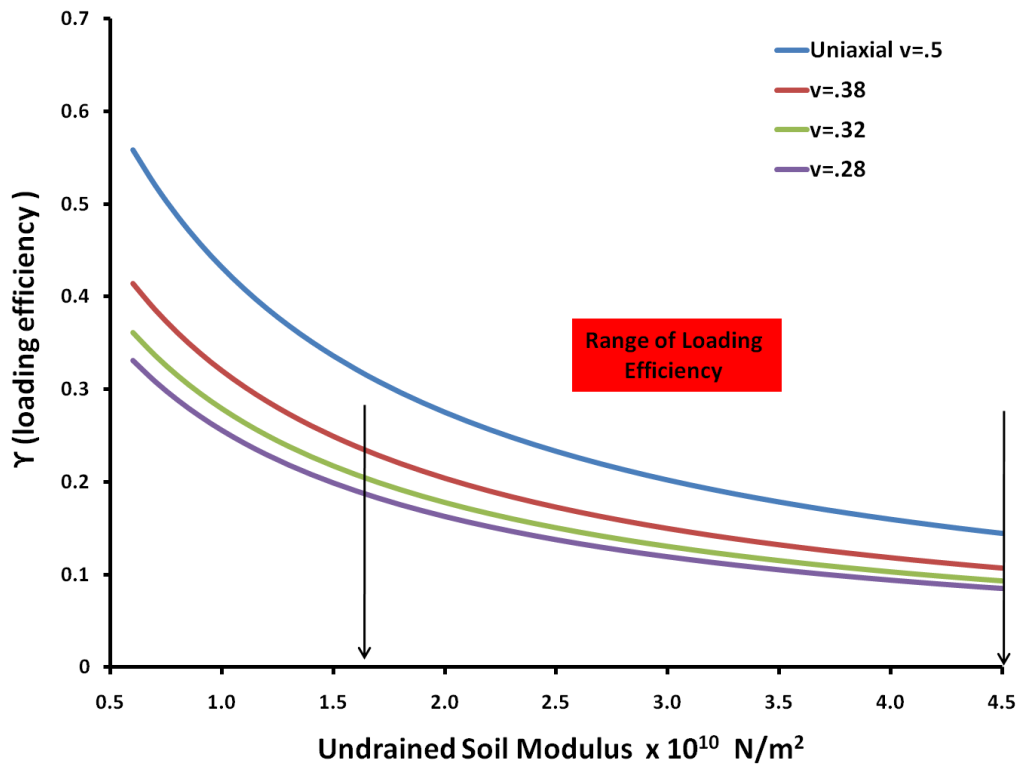


Figure 23. Loading efficiency chart for various common Poisson's ratio assuming pore fluid is water porosity $n=30\%$.

The observations of seepage of natural gas up the fault zone and existing hydrocarbon seeps at the sea floor near Platform Holly would be consistent with a pore space that is filled either partially or totally with gas as the compressible fluid. In order to adjust for this Wang (2000) suggests equation (15) for the calculation of Skempton's coefficient and loading efficiency. Using (15) and taking the vertical modulus of the gas as equal to the pore pressure generates a second set of graphs (Figure 24-27). Once again the calculated range of possible modulus values for the various amplitude ratios is shown.

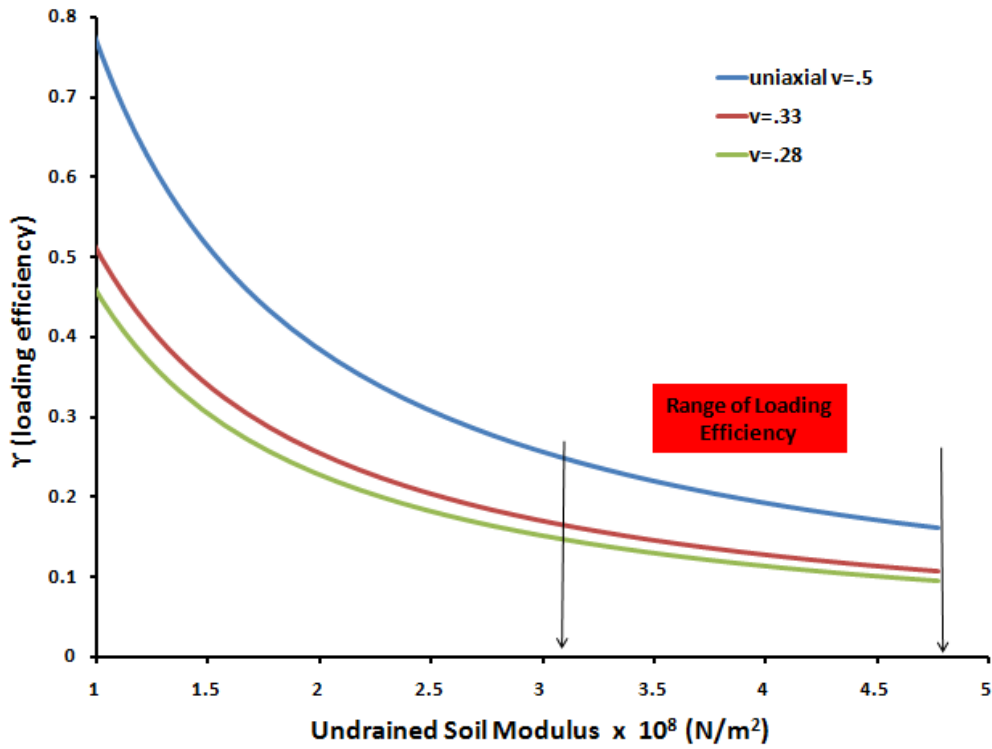


Figure 24. Loading efficiency chart for various common Poisson's ratio assuming pore fluid is gas porosity $n=10\%$.

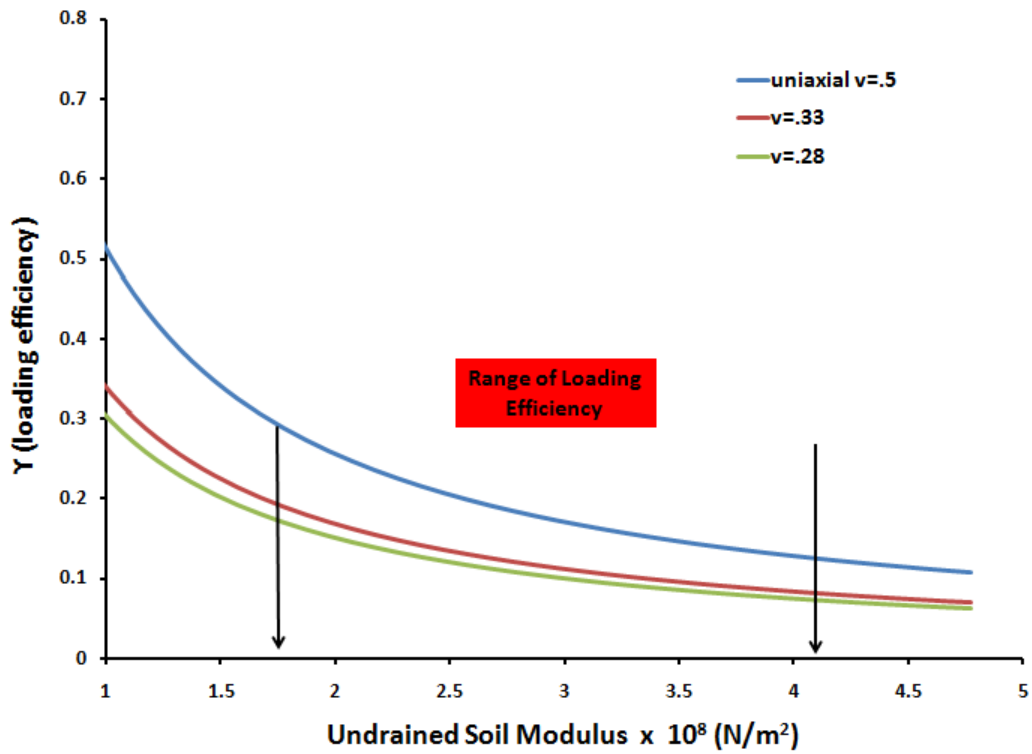


Figure 25. Loading efficiency chart for various common Poisson's ratio assuming pore fluid is gas porosity $n=15\%$.

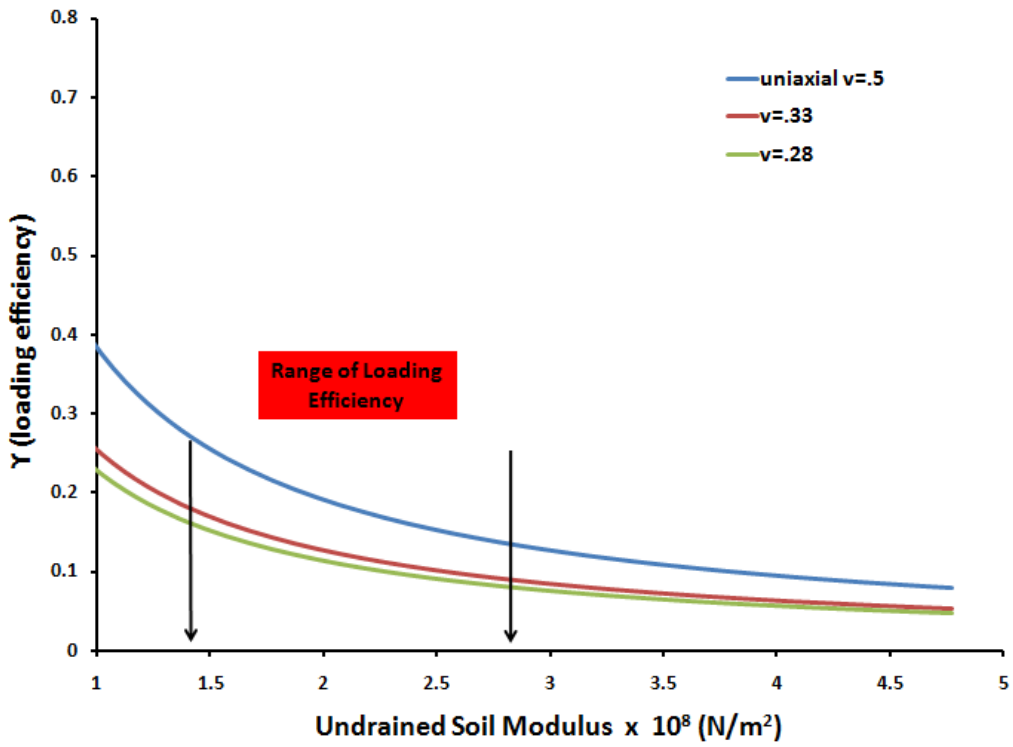


Figure 26. Loading efficiency chart for various common Poisson's ratio assuming pore fluid is gas porosity $n=20\%$.

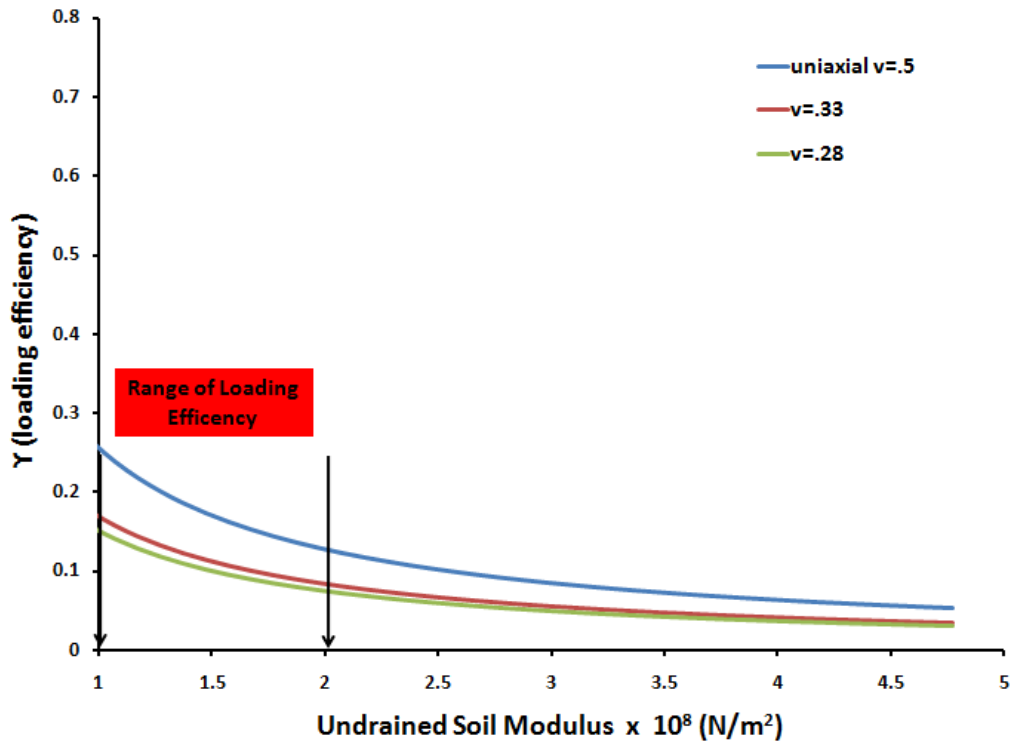
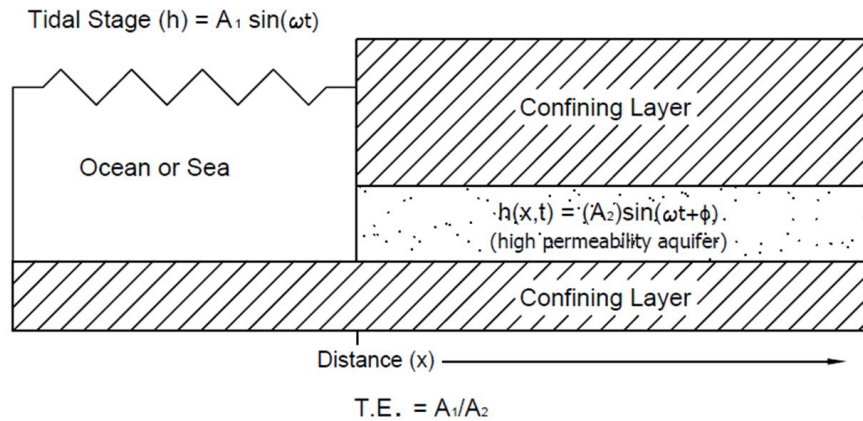


Figure 27. Loading efficiency chart for various common Poisson's ratio assuming pore fluid is gas porosity $n=30\%$.

3.4.2 Jacob / Ferris Model

The model suggested by Jacob (1940) and Ferris (1950) was originally developed for a confined aquifer extending to the coastline and cropping out beneath the sea where it is open to the imposed loading of the tide. The aquifer is assumed to be perfectly confined and the tidal fluctuation is treated as a simple sinusoidal wave. Using these boundary conditions Ferris recognized that this problem was analogous to ones already solved for heat flow (Ferris, 1952). The analogy between heat equation and the groundwater flow equation was assumed to be perfect and the solution developed by Ingersoll (1948) was applied for the boundary conditions just stated and shown in Figure 26 below.

Jacob & Ferris Model (original geology / situation)



Jacob & Ferris Model (applied to fault zone / geology beneath Platform Holly)

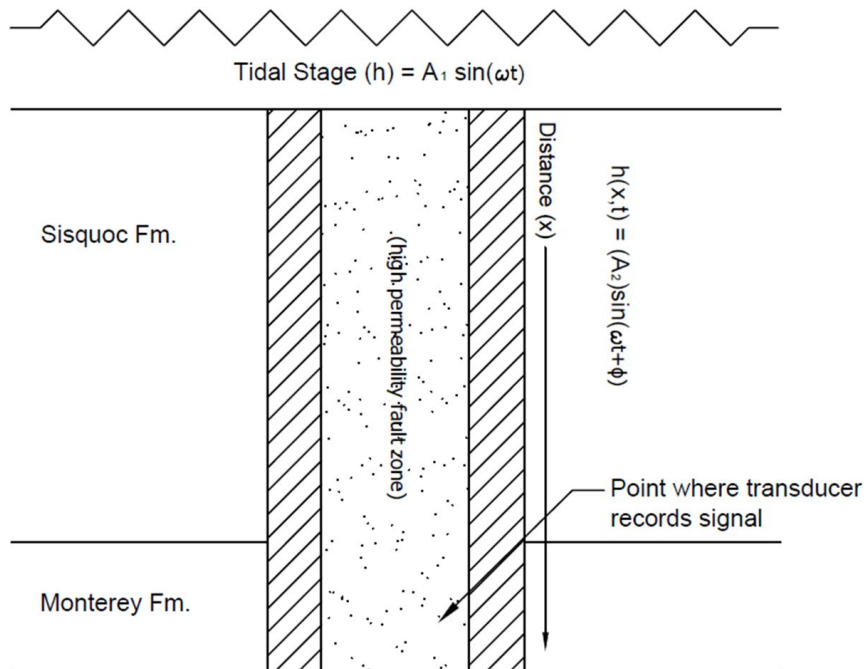


Figure 26. Illustration showing the Jacob-Ferris model for the propagation of the tidal signal into a coastal aquifer and how that model is applied to the field conditions in this study.

The use of the one-dimensional groundwater flow equation to model the processes that are occurring assumes that there is no real instantaneous elastic response to the formation and the dissipation of the pressure increase caused by the tidal loading is purely diffusive. There is an assumed elasticity in calculating the hydraulic diffusivity since it is dependent on specific storage and specific storage is dependent on the vertical compressibility of the soil. This compressibility is the drained compressibility and not the undrained compressibility utilized in the calculation of loading efficiency. Thus, it is strictly incorrect when applying the Jacob and Ferris model to assume that the reduction in amplitude is both a measure of loading efficiency and diffusion although this approach was taken in earlier studies (Carr and van der Kamp, 1969).

Assuming one-dimensional flow in an isotropic-homogeneous formation, the groundwater flow equation becomes (Freeze and Cherry, 1979):

$$\frac{\partial^2 h}{\partial x^2} = \frac{S_s}{K} \frac{\partial h}{\partial t} \quad (21)$$

With the boundary conditions shown in Fig. 26 the analytical solution becomes:

$$h(x, t) = A_1 e^{\Gamma_1} \sin(\omega t + \Gamma_1) \quad (22)$$

Or in terms of the period of the angular frequency:

$$h(x, t) = A_1 e^{\Gamma_2} \sin(\omega t + \Gamma_2) \quad (23)$$

Where:

$$\Gamma_1 = -x \sqrt{\frac{\omega S_s}{2K}} \quad (24)$$

$$\Gamma^2 = -x \sqrt{\frac{\pi S_s}{TK}} \quad (25)$$

The first part of (22) and (23) is the reduction term which simply describes the amplitude attenuation with depth. The amplitude attenuation with depth from (22) can be written as:

$$h(x, t) = A_1 e^{\Gamma^2} \quad (26)$$

The second term of (22) or (23) is an expression for the phase shift in the signal from the original sinusoidal frequency. Converting the last part of (22) and (23) to a form using the time difference or time lag from when the loading is imposed at the surface and when it is recorded at depth yields:

$$\Delta\phi = \omega t_l = x \sqrt{\frac{\pi S_s}{TK}} \quad (27)$$

Using (23) and (24), it is possible to get to estimates for the ratio of specific storage to conductivity which is an expression for the hydraulic diffusivity:

$$\frac{S_s}{K} = \frac{1}{D} \quad (28)$$

The application of (25) is listed in Table 4 below. This was done for each constituent by first equating the ratios in Table 3 to the division of the pressure signal at distance x and time t by the amplitude at the surface (26). This allows one to then solve for the ratio of specific storage to conductivity and the hydraulic diffusivity because the period T for that given tidal constituent is known:

$$\frac{A_2}{A_1} = e^{-x\sqrt{\frac{\pi S}{TK}}} \quad (29)$$

Table 4. Diffusivity based on equation 26

Harmonic	Amplitude ratio(T.E.)	Diffusivity (m ² /s)
K1	0.17	49.5
M2	0.16	89.3
O1	0.16	42.7
N2	0.17	97.4
S2	0.13	77.7

Solving (27) for the time lag requires that the phase angle is calculated for both the tidal signal at the surface and the pressure signal at depth (Table 2) be subtracted from each other. Care must be taken in doing this and the difference can only be resolved assuming the signals are not more than 360 degrees apart and remembering that the tidal signal produces the pressure signal so the pressure signal at depth must come later in time. The input parameters for this calculation and the calculation of diffusivity from this method are summarized in Tables 5 and 6. The depth at which the signal was recorded was estimated to be about 1.5 km (~4920 ft) down the fault. It should be noted that the diffusivities seen in Tables 4 and 6 vary significantly. This difference will be discussed in Chapter 5.

Table 5. Input parameters for determining diffusivity from time lag.

depth below surface (m)=	1480
Phase Angle difference K1 (rad)=	2.18986
Phase Angle difference M2 (rad)=	4.83561
Phase Angle difference O1 (rad)=	2.37592
Phase Angle difference N2 (rad)=	5.09689
Phase Angle difference S2 (rad)=	4.56055

Table 6. Calculation of diffusivity from time lag.

Harmonic	Tidal Frequency (rad/hr)	Time lag (hrs)	Hydraulic Diffusivity (m ² /s)
K1	0.26251618	8.34	16.6
M2	0.50586804	9.56	12.7
O1	0.24335189	9.76	12.2
N2	0.49636693	10.27	11
S2	0.52359878	8.71	15.3

3.4.3 van der Kamp and Wang Solution

The use of Skempton's loading efficiency to calculate the vertical undrained modulus of the soil requires that the control volume be completely closed to any flow. In contrast the use of the Ferris model requires that one assume the control volume is open to flow and the transmission of pressure is governed by the isotropic-homogeneous form of the groundwater flow or diffusion equation. What is needed is an overall equation that describes both the instantaneous loading and undrained response of loading efficiency and utilizes the basic groundwater flow equation to govern the dissipation of that pressure

with time. This equation is the one-dimensional consolidation equation which can be written in many different ways (van der Kamp, 1983; Domenico and Schwartz, 1990; Wang 2000). Writing this expression in terms of excess pore pressure one can write:

$$K_x \frac{\partial^2 P}{\partial x^2} = S_s \frac{\partial P}{\partial t} - (\rho_w g \beta) \frac{\partial \sigma}{\partial t} \quad (30)$$

This equation can also be expressed in terms of loading efficiency and hydraulic diffusivity as:

$$D \frac{\partial^2 P}{\partial x^2} = - \left(\frac{\partial P}{\partial t} + \gamma \frac{\partial \sigma}{\partial t} \right) \quad (31)$$

Equation (30) and (31) allow a loading event to be imposed on the porous, elastic medium and utilize the loading efficiency term to describe how that loading is transmitted to the pore pressure (and therefore effective stress). This pressure is then dissipated according to the diffusion or groundwater flow equation. Of course, the uniaxial strain condition is invoked along with all the assumptions inherent in the specific storage term and the development of the basic groundwater flow equation. For any subdued tidal signal recorded at depth, the time lag observed is attributed to the diffusion part of (31) and the amplitude reduction is the result of the instantaneous poroelastic formation response coupled with the diffusive component. While various analytical solutions exist to solve (31), Wang (2000) presents the following solution in terms of the pressure differential from the surface tidal loading to the pore pressure recorded at depth.

$$\Delta P = (1 - \gamma) P_s \left[\left(\exp\left(\frac{-z}{\delta} \cos\left(\frac{z}{\delta}\right) - 1\right)^2 + \exp\left(\frac{-z}{\delta} \sin\left(\frac{z}{\delta}\right)\right)^2 \right)^{1/2} \right] \quad (32)$$

$$\delta = \sqrt{2D/\omega} \quad (33)$$

The characteristic length δ represents the distance at which the term $\exp(-z\sqrt{\omega/2D})$ decays to 1/e times its original boundary (Wang, 2000).

These equations allow one to use the time lag t_l to solve for the hydraulic diffusivity in (31). This is the same diffusivity calculated from the Ferris model in (27). Once this value is calculated and the “ δ ” term is calculated in (33) it is possible to subtract the signal at depth amplitude from the tidal signal amplitude and treat this as the difference in pressure. This pressure difference is then divided by the pressure amplitude recorded at depth and one can manipulate (32) to solve for the loading efficiency. Table 7 below illustrates the calculation of loading efficiency for the five different harmonic constituents.

Table 7. Calculation of loading efficiency from Wang & van-der Kamp model

Harmonic	Angular Frequency (rad/hr)	Time lag (hrs)	Hydraulic Diffusivity (m²/hr)	Amplitude Ratio Difference	δ (m)	Loading Efficiency (Y)
K1	0.26251618	8.34	16.6	1.16	675.84	0.22
M2	0.50586804	9.56	12.7	1.35	424.87	0.18
O1	0.24335189	9.76	12.2	0.59	599.75	0.21
N2	0.49636693	10.27	11	0.27	399.28	0.19
S2	0.52359878	8.71	15.3	0.49	458.32	0.16
AVERAGES		9.33	13.6			0.19

While Table 7 lists the direct calculation of loading efficiency from the previously calculated diffusivity and angular frequency of each constituent, but it is also

useful to plot (32) in order to understand how loading efficiency will change with depth. I have done this with (32) in terms of amplitude ratio versus depth for the K_1 and M_2 constituents with a diffusivity of $13.9 \text{ m}^2/\text{s}$ (Figures 26 and 27). These plots show an exponentially decreasing ratio. The exponential nature of this decrease is predicted in (24), (25), and (32) and can easily be seen in the structure of the first exponential terms in these equations.

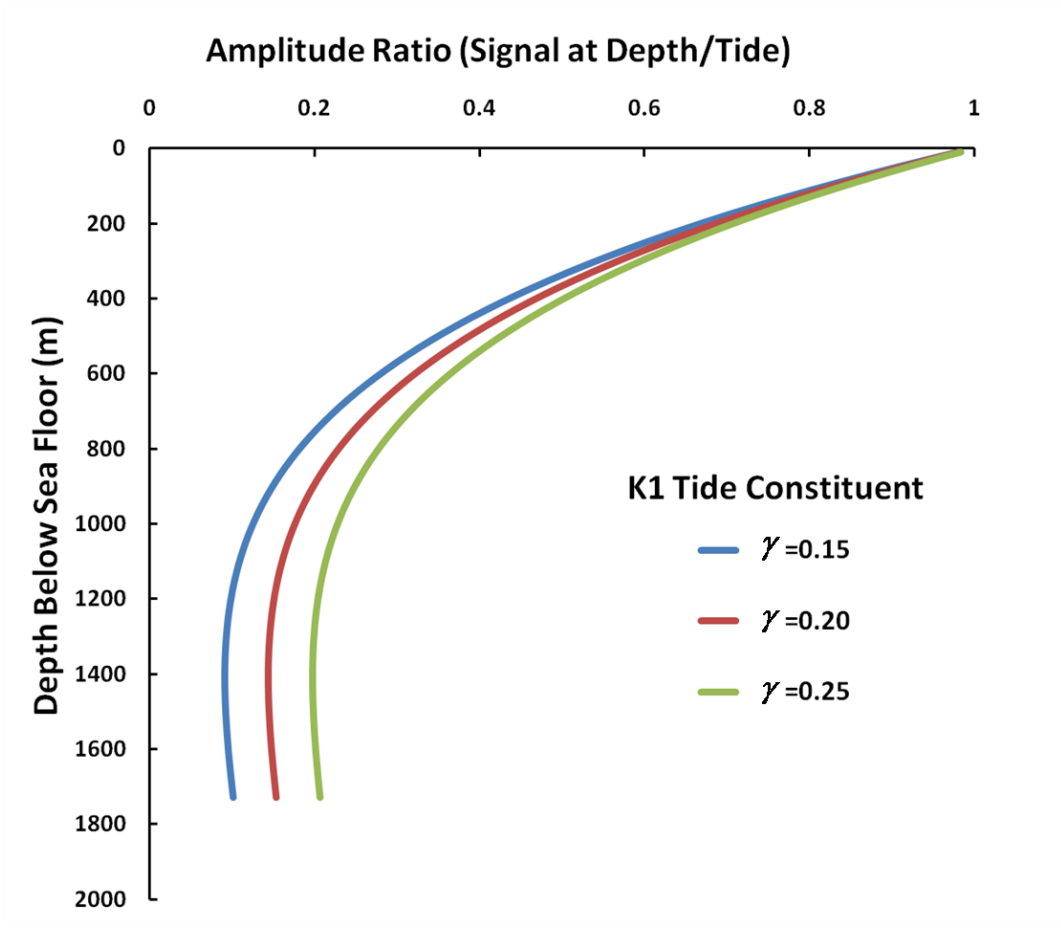


Figure 28. Amplitude reduction for K1 tide constituent as a function of depth. Diffusivity = 13.9 m²/s with three different values of loading efficiency γ .

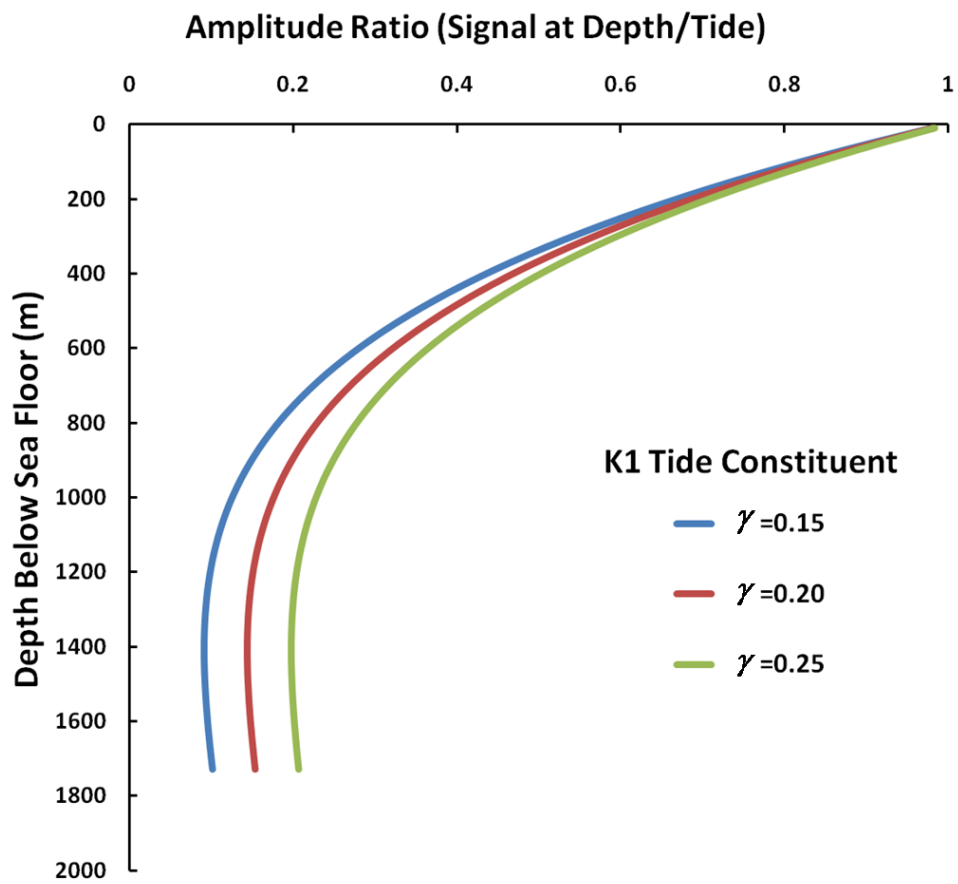


Figure 29. Amplitude reduction for M2 tide constituent as a function of depth. Diffusivity = $13.9 \text{ m}^2/\text{s}$ with three different values of loading efficiency γ .

3.5 Summary

This chapter has presented a quantitative analysis of both the tidal signal recorded in the Santa Barbara Channel and the signal recorded at subsurface depth in Well #13. The analysis has focused on two parts, with the first part being the application of traditional signal-analysis techniques which were employed to decompose both of the signals. The fast Fourier transform was performed on both the tidal signal and the signal at depth to illustrate that both contained the same tidal frequencies. The classical oceanography technique of a least-squares harmonic regression was applied to both signal records to determine amplitude and phase of each of the five basic tidal constituent frequencies (Tables 2 and 3).

The phase angle differences and amplitude ratios were then used to calculate various properties of the fault zone material. The first analytical technique employed was to treat the amplitude ratio as a measure of loading efficiency and calculate the vertical undrained modulus of the soil or rock skeleton. A decision must be made whether gas or water fills the pore space and charts (Fig. 20-27) were made to display the ranges of possible modulus.

The second and third analytical solutions applied relied on solving two different versions of the simplified 1-D groundwater flow equation. The first was the Jacob-Ferris solution, which is a solution to the groundwater flow equation with no poroelastic component. The second analytical solution solved a version of the groundwater flow equation with a poroelastic term, which is the loading efficiency term from the earlier solution. The point in applying these two different analytical solutions was to use the time lag to solve for hydraulic diffusivity and then use diffusivity to solve for the loading efficiency term in equation 30. Once the loading efficiency is estimated, one can consult

Figures 20-27 to determine a modulus value for the formation. It should be noted that the calculated loading efficiency in Table 7 happens to be equal to the amplitude ratio and makes one consider the necessity of equation (32) to solve for loading efficiency if one can determine it from the amplitude ratio. Figures 26 and 27 plot out (32) for the two main tidal constituents for a diffusivity of $13.9 \text{ m}^2/\text{s}$. These charts plot out the amplitude reduction with depth for the fault zone beneath Platform Holly.

Chapter 4: Application of Numerical Modeling

4.1 Overview

This chapter presents numerical simulations that are designed to further explore the diffusion and attenuation of the tidal signal in the South Ellwood fault zone. The numerical simulations are valuable because, in addition to studying the one-dimensional signal propagation, it is possible to explore how the signal might first propagate and attenuate down the fault zone and then into a stratigraphic unit such as the Monterey Formation. The simulations also allows for exploration of how changing the diffusivity would affect the signal attenuation and propagation. The three objectives to the modeling are:

1. Simulate the signal attenuation with depth
2. Investigate the effects of fault zone anisotropy in 2D signal propagation.
3. Explore parameter sensitivity.

The commercial the finite element code *SEEP/W* was used for this study. This software access was made available through a user license in the Department of Civil Engineering and is distributed by GEO-SLOPE International Ltd.

4.2 Assumptions and Simplifications

The geology beneath Platform Holly and across the entire Santa Barbara Basin represents a complex stratigraphy that is the result of a dynamic geologic history. This history includes geomechanical and geochemistry components that are complex and can be mapped on spatial scales ranging from microns to kilometers. In light of this wide

spectrum it is challenging to model the effect of tidal signal propagation down the fault zone near Platform Holly and into surrounding formations. The biggest challenge is in trying to incorporate the effects of small scale lithology and structure within the larger kilometer scale.

Geologists have mapped the sedimentology, structure, and stratigraphy in the Santa Barbara basin it is possible to classify the rock types into various formations. The stratigraphic succession beneath Platform Holly can be grouped into the Sisquoc, Monterey and Rincon formation. And each formation can be subdivided further into distinct layers for the purposes of modeling each formation is treated as a homogeneous material with the exception of the Monterey. For this thesis, the Monterey Formation is subdivided into an upper and lower zone. The decision to divide the Monterey in this way was based on geophysical log data provided by Venoco Inc for Well #13 and other geologic studies of the formation. Field studies by the USGS and other geologists suggest anywhere from three to seven distinct stratigraphics zones in the Monterey, (Tennyson and Kropp, 1998; Galloway, 1998; Minor et al., 2007). Geophysical log data for Well#13 also shows a higher percentage of shale (and associated hydrocarbons) in the lower part of the Monterey.

In light of the lithologic and structural complexity, and the need to simplify that complexity for the purposes of numerical modeling, a simplified geologic profile became the basis of the model (Figure 30).

The challenge in modeling this section came from trying to incorporate a very narrow fault zone within the larger “kilometer” scale section. The fault zones illustrated in Figure 31 are 27 m (88.5 ft) wide which is unrealistic when evaluated in light of field studies. Despite this the width of the fault zone was necessary to ensure there were no numerical issues with the grid spacing. Furthermore, one of the assumptions made about the fault zones is that they are most permeable along there vertical and that any

movement of geofluids takes a path that goes from surrounding formations to the fault zone and then up or down the fault. The reverse path is also possible. In light of this the vertical movement of fluid up and down the fault is the primary topic of interest when considering the fault zone on its own. The inter-fault horizontal or two dimensional flow regime is assumed to be negligible when compared to the overwhelmingly vertical component. This means that so long as the width of the fault zone does not obscure the impact of the geometry of adjacent layers, then the actual width of the fault is of negligible importance in a kilometer-scale simulation. My focus is on the one-dimensional nature of the tidal propagation signal.

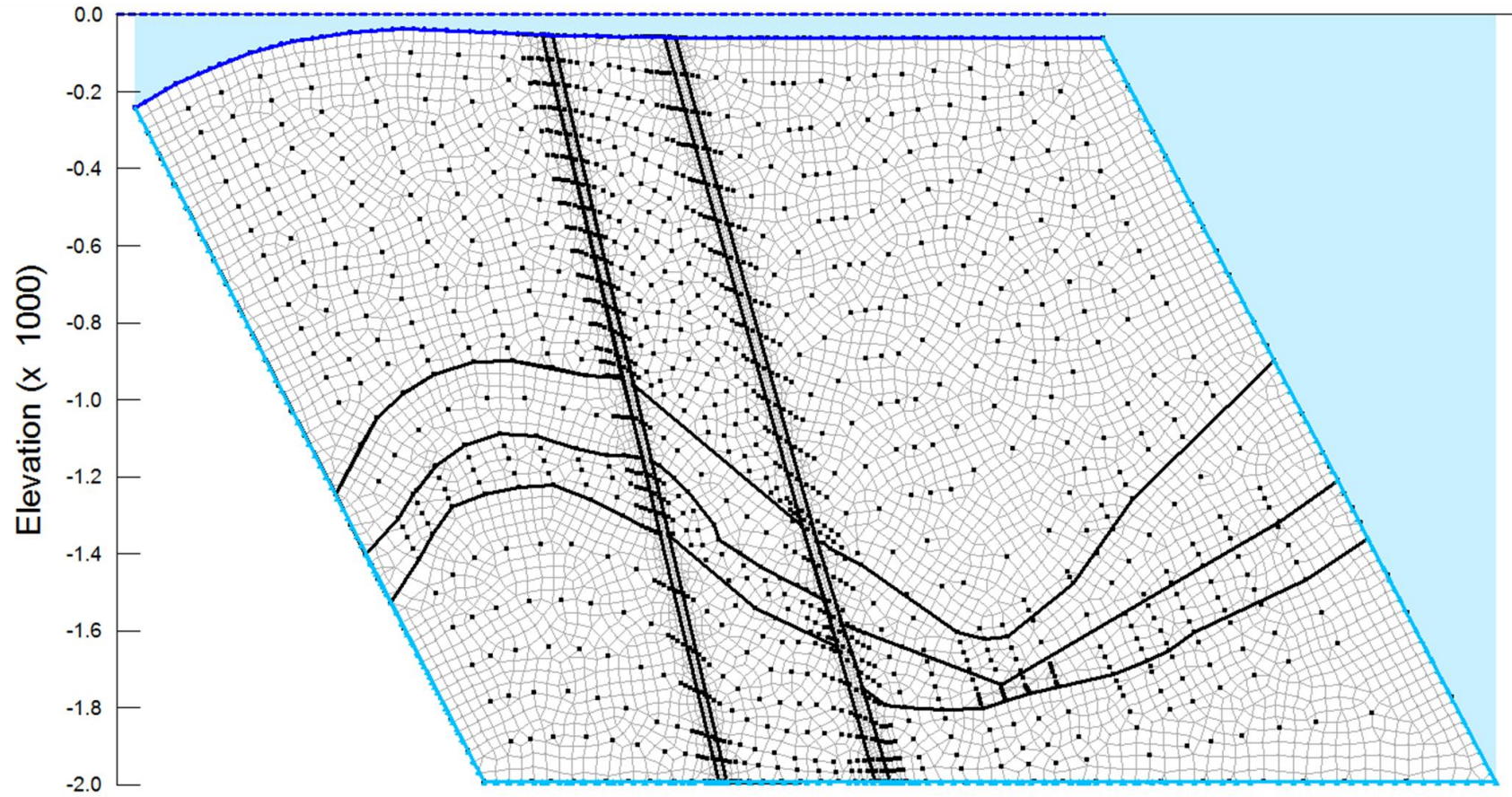


Figure 30: SEEP/W Model with stratigraphy, fault zones and mesh. Vertical axis in meters.

Another assumption to discuss is the distance and nature of the model boundaries. Inspection of various uplifted geologic cross sections of the Santa Barbara basin reveal that the basin is strongly deformed on its north by a large anticlinal system (Rincon trend) that is broken up by numerous faults. The section chosen for modeling was taken from a larger structural cross section provided by Venoco Inc., and is bounded on the left and right side by two faults. Since some field and numerical studies suggest that faults often behave as a barrier to horizontal flow the boundaries (faults) on either of the section sides were assigned no flow boundary conditions (Caine et al., 1996; Antonellini and Aydin, 1999; Heynekamp et al., 1999; Stanislavsky and Garven, 2003)

The final modeling assumption common to all hydrogeology studies is the choice of material properties. These material properties are the effective porosity, bulk compressibility and hydraulic conductivity of each geologic unit portrayed in the model. Table 8 lists the material properties assigned for each formation seen in Figure 6 and the model. The formation properties chosen were thought geologically representative (California Department of Conservation Division of Oil, Gas, and Geothermal Resources, 1991) (Appold et al., 2007). These parameters fall within the expected range as suggested by other researchers (Ge and Garven, 1992; Neuzil, 2003).

Table 8. Typical formation properties for model simulation. Fault zone formation properties keep the fault diffusivity at 13.9 m²/s.

Formation	Sisquoc	Monterey M1-M5	Monterey M6-M7	Rincon	Fault Zone
Porosity=	0.30	0.25	0.25	0.15	0.1
Hydraulic Conductivity K _x (m/s)=	3.17E-09	3.17E-07	4.83E-08	3.17E-10	9.00E-05
Hydraulic Conductivity K _z (m/s)=	3.17E-09	7.93E-08	1.21E-08	3.17E-10	9.00E-05
Formation Compressibility α (Pa ⁻¹)=	3.00E-10	3.00E-10	3.00E-10	3.00E-10	6.60E-07

It should be noted in Table 8 that the hydraulic conductivity and bulk compressibility value for the fault chosen are to reflect a hydraulic diffusivity of 13.9 m²/s based on my analysis of the Ferris / Jacob analytical solution calculated as an average, representative value on all five tidal constituents. There are a broad range of hydraulic conductivities and specific storage coefficients combinations that could make this diffusivity possible, but the choices listed in this table were assumed to be plausible. In theory the hydraulic diffusivity value in the fault zone is what is important to the signal propagation down the fault. This point will be discussed further in the conclusion chapter.

4.3 Simulation of Tidal Signal Propagation down Fault Zone

The model parameters listed in Table 8 were used to simulate the tidal signal propagation down the fault zone. The objective of this modeling was to see if the signal

attenuation could be replicated at depth and to see if the signal would propagate into the Monterey Formation containing anisotropic characteristics. The left, right, and bottom boundaries were set as no flow boundaries and the initial condition is hydrostatic (hydraulic head=0 m). The vertical scale was set so that 0 elevation corresponded to mean sea level.

The top boundary of the model (sea floor) was set as a fluctuating boundary condition that represented the tidal cycles. This boundary condition was created by downloading 400 hrs of tidal data from the NOAA website for the Santa Barbara Tide Station starting from 01/01/2013. The file contained values of tidal stage in meters and time in hour increments. This data was then loaded into the SEEP/W program and fitted with a spline function which smoothed the hydraulic head data for time increments less than an hour (Figure 31).

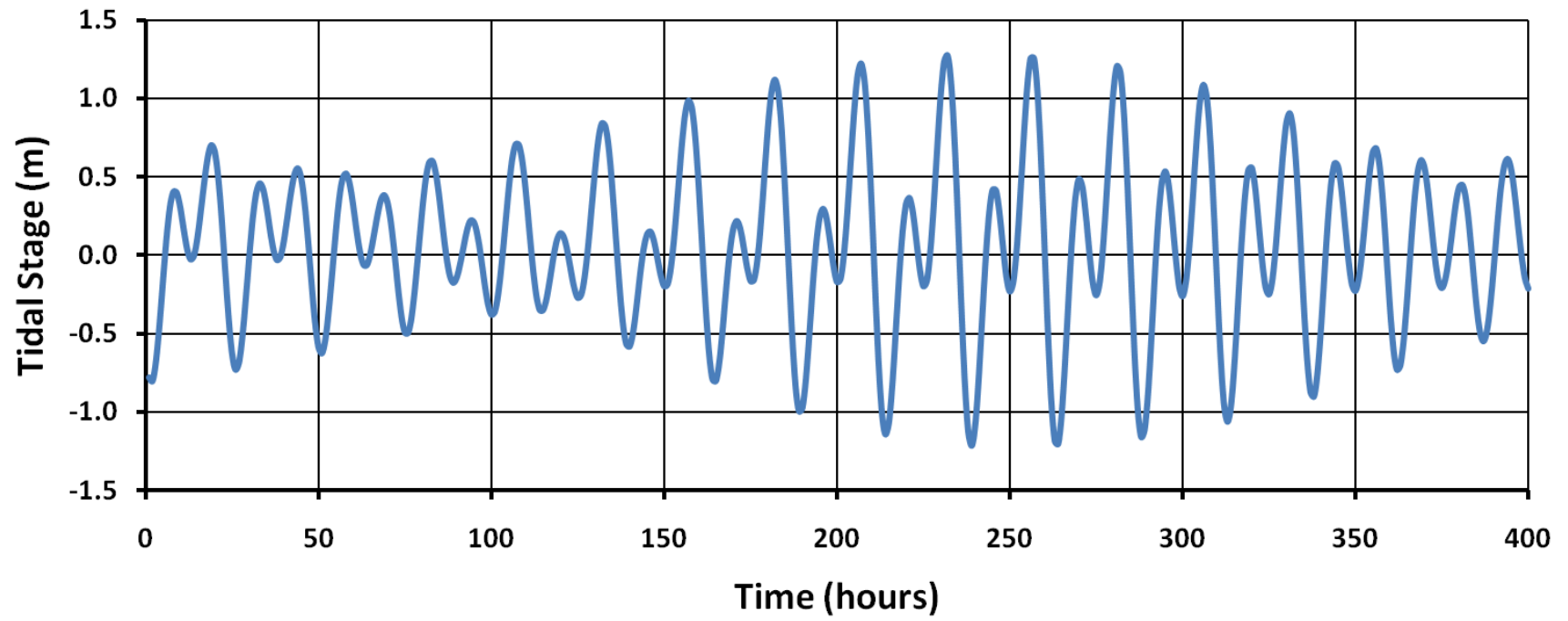


Figure 31: Tidal stage vs. time as top boundary condition for the simulation.

The model simulation was allowed to run for 400 hrs at a time step of $\Delta t=1$ hr. Every time step was saved so that an accurate record of hydraulic head changes could be recorded at depth and so that the sampling frequency of the head changes with time would be small enough to capture the tidal signal profile.

At both the bottom and top of the Monterey Formation, near the projected path of Well #13, a node was selected and the pressure head versus time record was reconstructed for the 400 hour time period. This pressure record was plotted with the original tidal signal input at the surface and the two were compared. The top of the formation corresponded to a depth of about 1200 m (4,000 ft) while the bottom of the formation corresponded to a depth of 1500 m (5,000 ft). These depth were taken to illustrate how the pore-pressure signal can change with depth. The depth range that the signal was captured at during the actual recording of the pressure signal at depth likely falls between these two intervals (Figures 32 and 33).

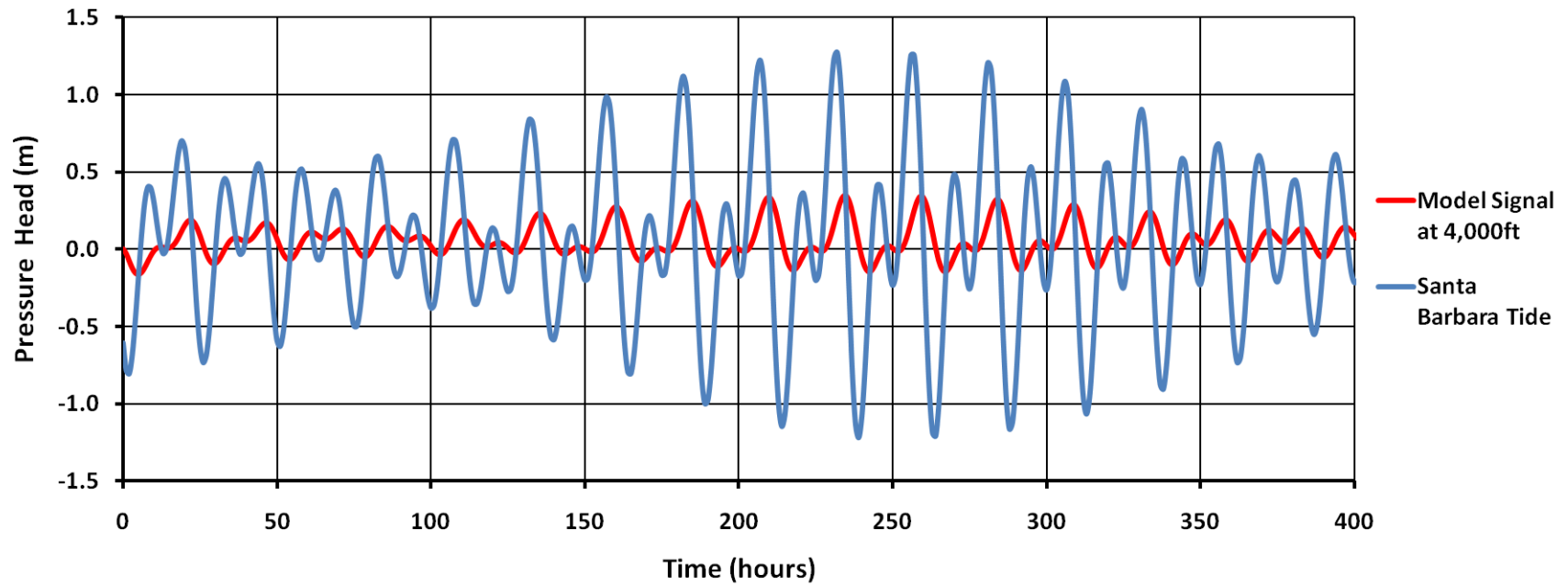


Figure 32: Diffusive signal propagation and original tidal signal at depth 1208m (4,000 ft). $D=13.9 \text{ m}^2/\text{s}$

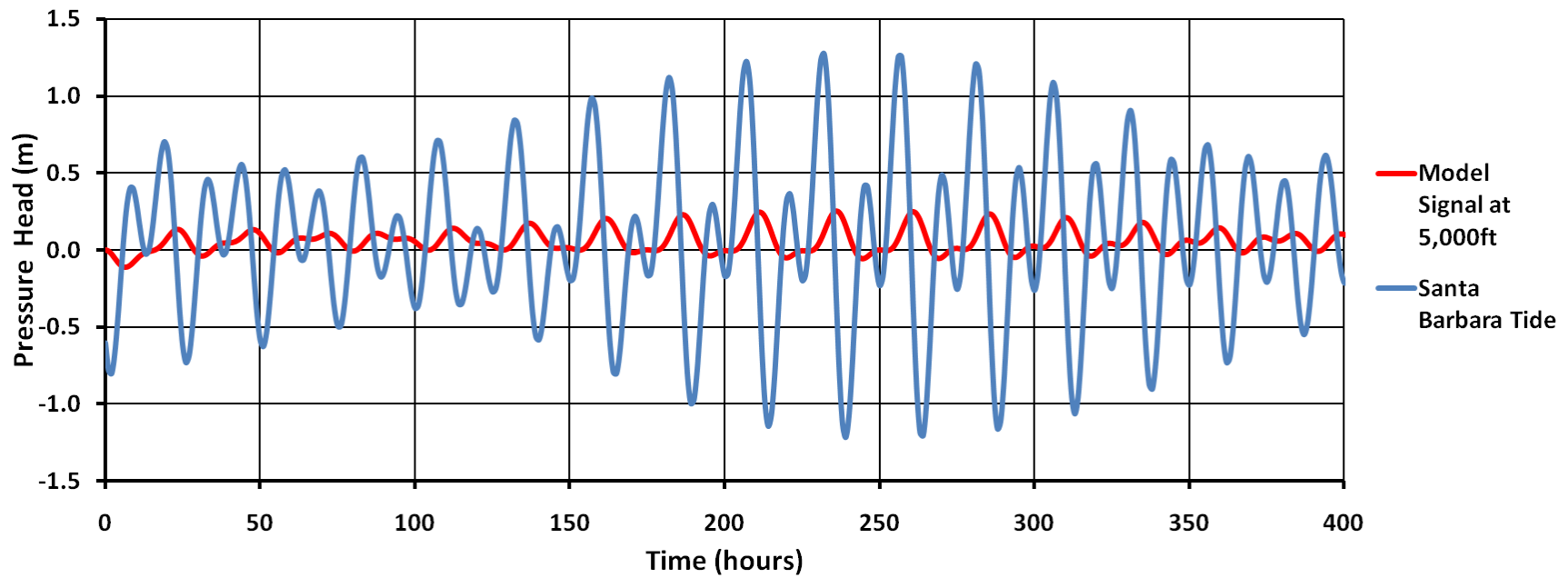


Figure 33. Diffusive signal propagation and original tidal signal at depth 1500m (5,000 ft). $D=13.9 \text{ m}^2/\text{s}$

Figures represent the signal attenuation as governed by the diffusive processes as represented in 21. An attempt was also made to include the poroelastic part or the loading efficiency term of (30). This term was calculated to be $\Upsilon \sim 0.20$ for all the individual tidal constituents. Since the theory behind (30) states that the pressure signal at depth is a summation of the pressures due to instantaneous deformation of the media and the diffusive signal, it is appropriate to assume that the instantaneous pore pressure head increase at depth is simply loading efficiency multiplied by the stage or height of the tide at the surface (Wang, 2000). This diffusive component can then be added to the diffusive signal in Figures 32 and 33 for any moment in time. The result of the addition of the elastic component to the signal can be seen Figures 32 and 33 for the same depths as Figures 34 and 35.

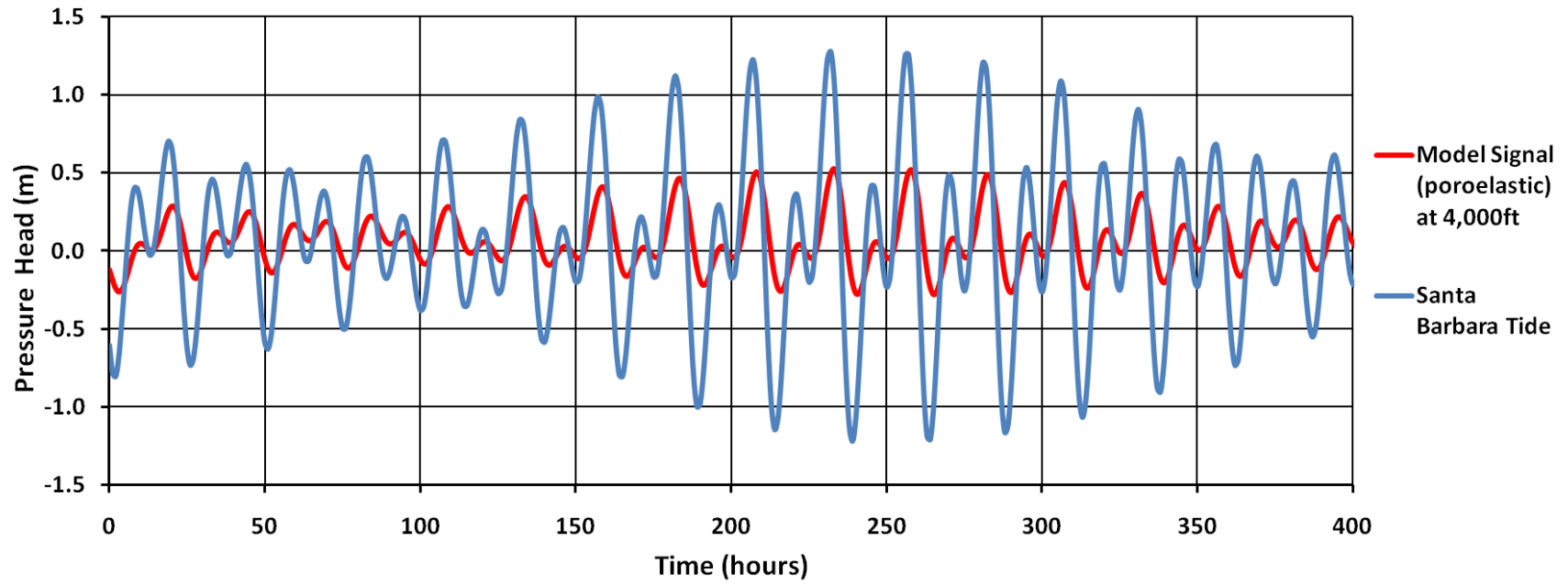


Figure 34. Diffusive and elastic signal with tide at 1208 m (4,000ft).

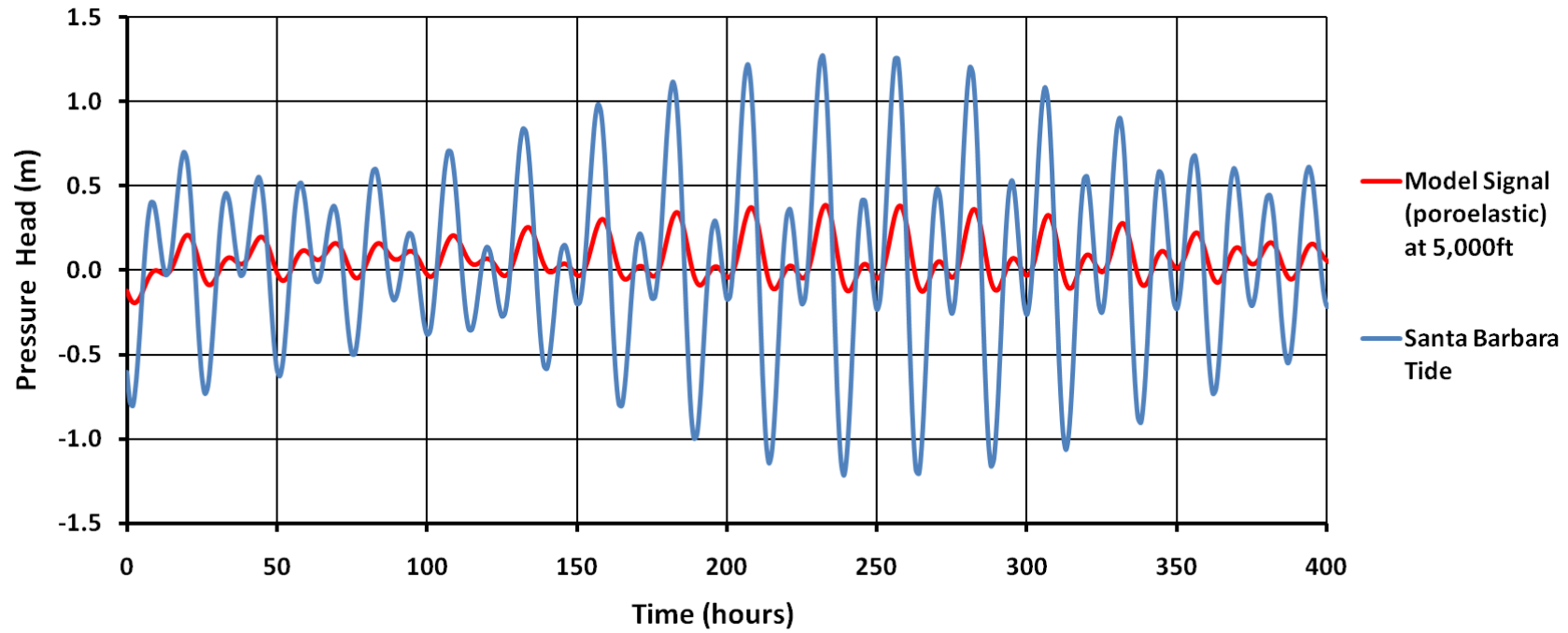


Figure 35. Diffusive and elastic signal with tide at 1500m (5,000 ft).

Another interesting way to view the results of the numerical model is to see the amplitude attenuation of the tidal signal as function of depth. Figure 36 below shows a plot of the pressure head versus depth for 19 hours. The 19 hour interval must be chosen because at this point the tidal height is at a local 12 hour maximum which allows one to see the true amplitude attenuation. According to the theory proposed by Jacob and Ferris, this processes should show an exponential decay governed by (29). Figure 36 shows both the numerical model results and the analytical solution. It should be noted that to utilize (29) in this plot it must be plotted assuming only one tidal constituent at a time. This was only done for both the K_1 and M_2 constituents, as these are the most dominant constituents in the time series and also represent the diurnal and semidiurnal frequencies seen in the tide.

It is also interesting to graph the pore pressures changes along the fault for either the rising or the falling of the tide (Figure 37 and 38). These figures also show the exponential attenuation of the tidal signal as predicted by the Jacob & Ferris solution in (29). In looking at these figures it is possible to see how with the rising and falling of the tide the pore pressure head in the fault is always changing.

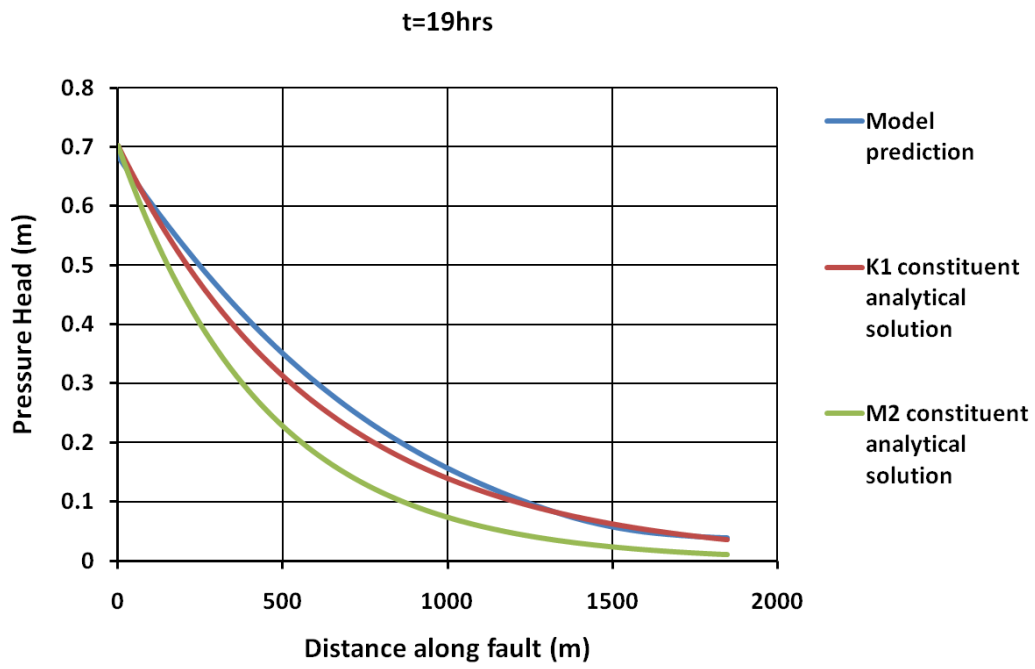


Figure 36. Signal attenuation, model prediction and analytical solution.

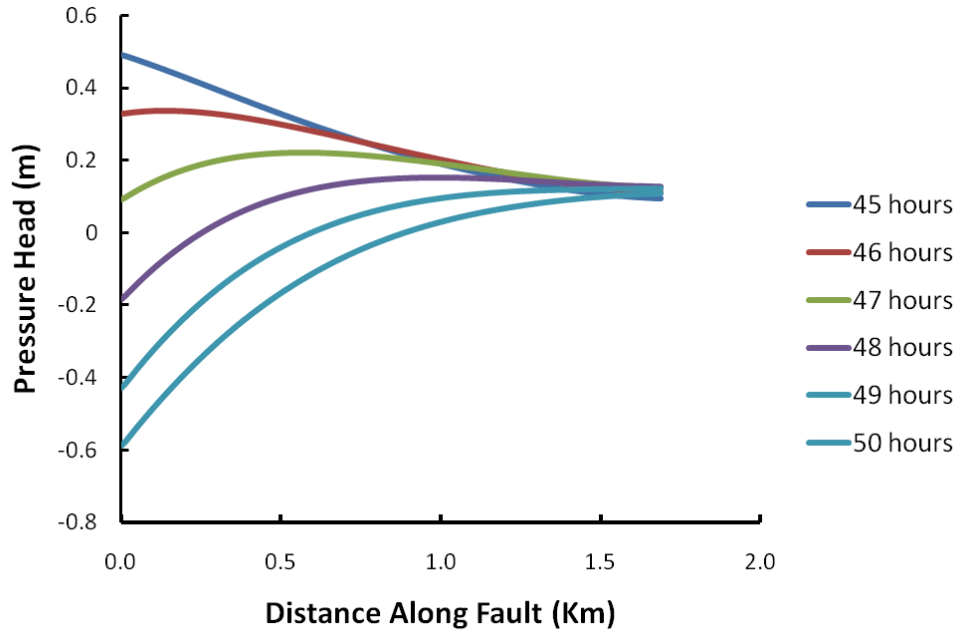


Figure 37. Pressure head changes vs distance along the fault for the falling of the tide.

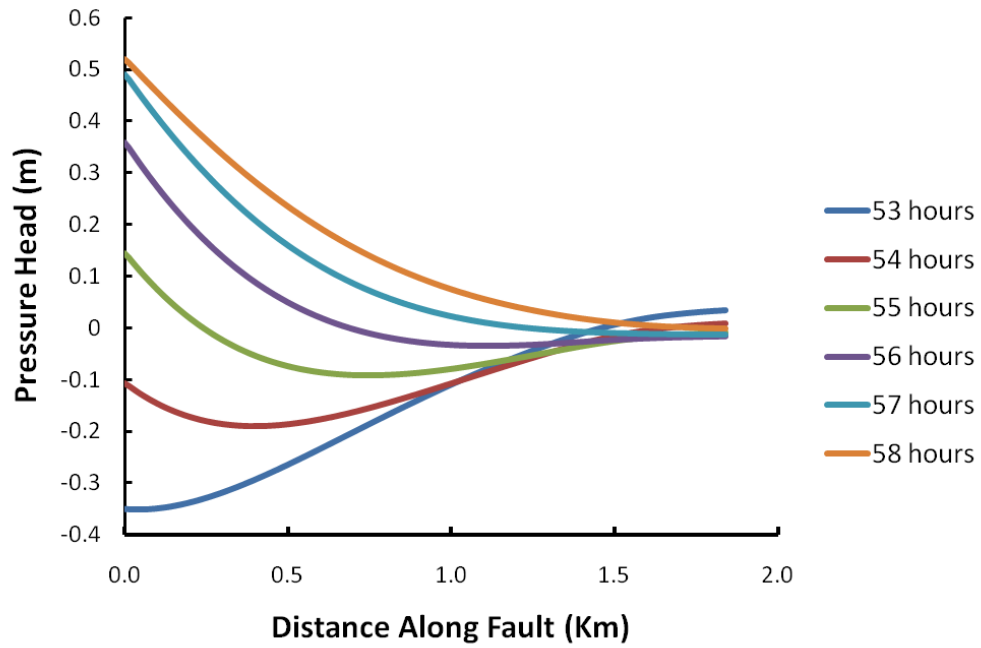


Figure 38. Pressure head changes vs distance along the fault for the rise of the tide.

Finally, the simulation shows some interesting results for the pressure propagation into the adjacent Monterey Formation, and other formations. The simulation shows how the tidal signal propagates down the fault and diffuses into the surrounding formations where it is affected by the hydraulic anisotropy of the formation. Figures 39-42 show the pressure head distribution in the section beneath Platform Holly at various time steps. The implication of these results will be discussed further in Chapter 5.

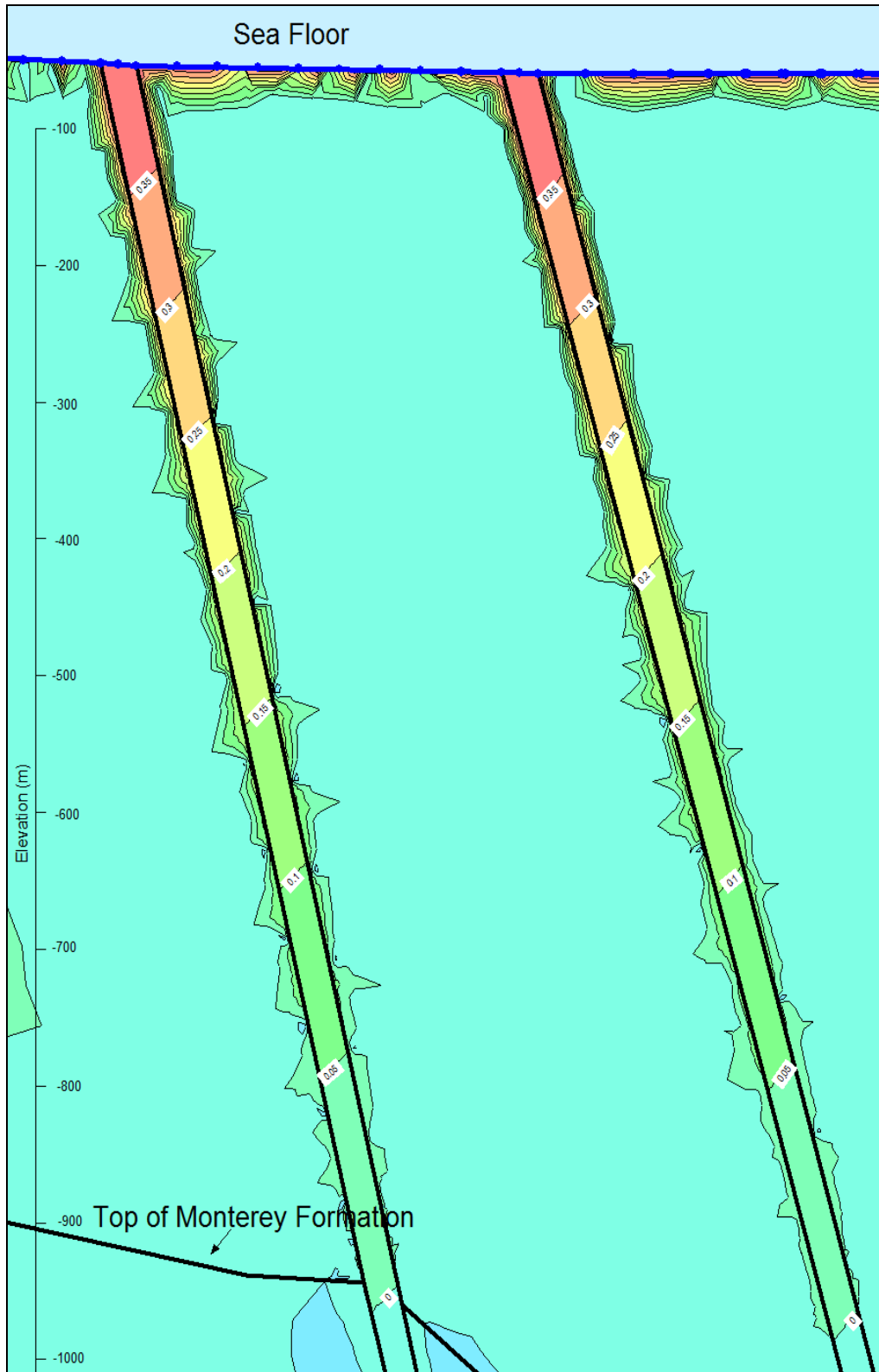


Figure 39. Pressure head propagation down fault towards the Monterey Formation.

Lines are of constant pressure head. $t=9$ hrs.

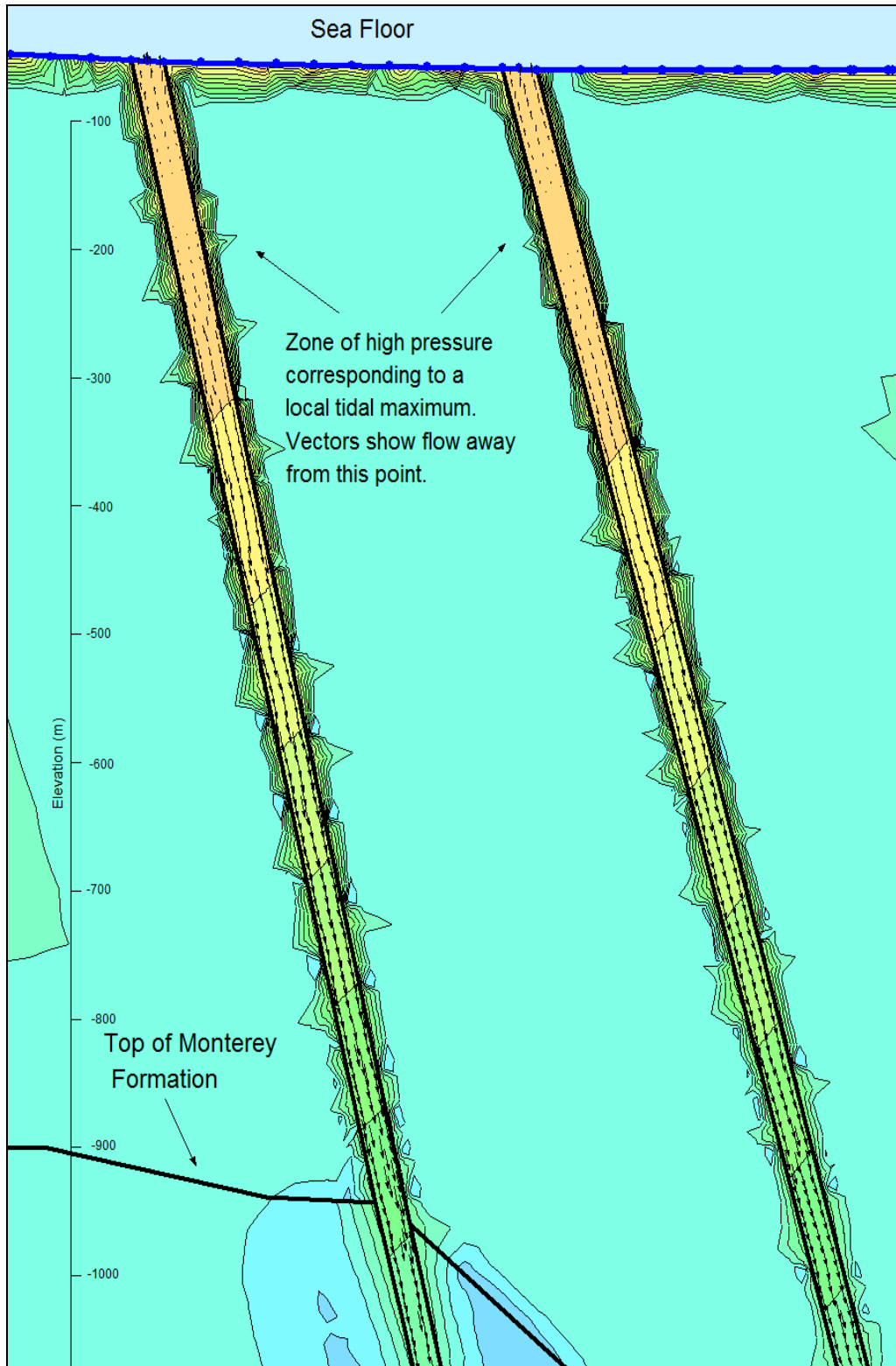


Figure 40. Start of high pressure pulse propagating down fault zone and start of propagation into Monterey Formation. $t=11$ hrs.

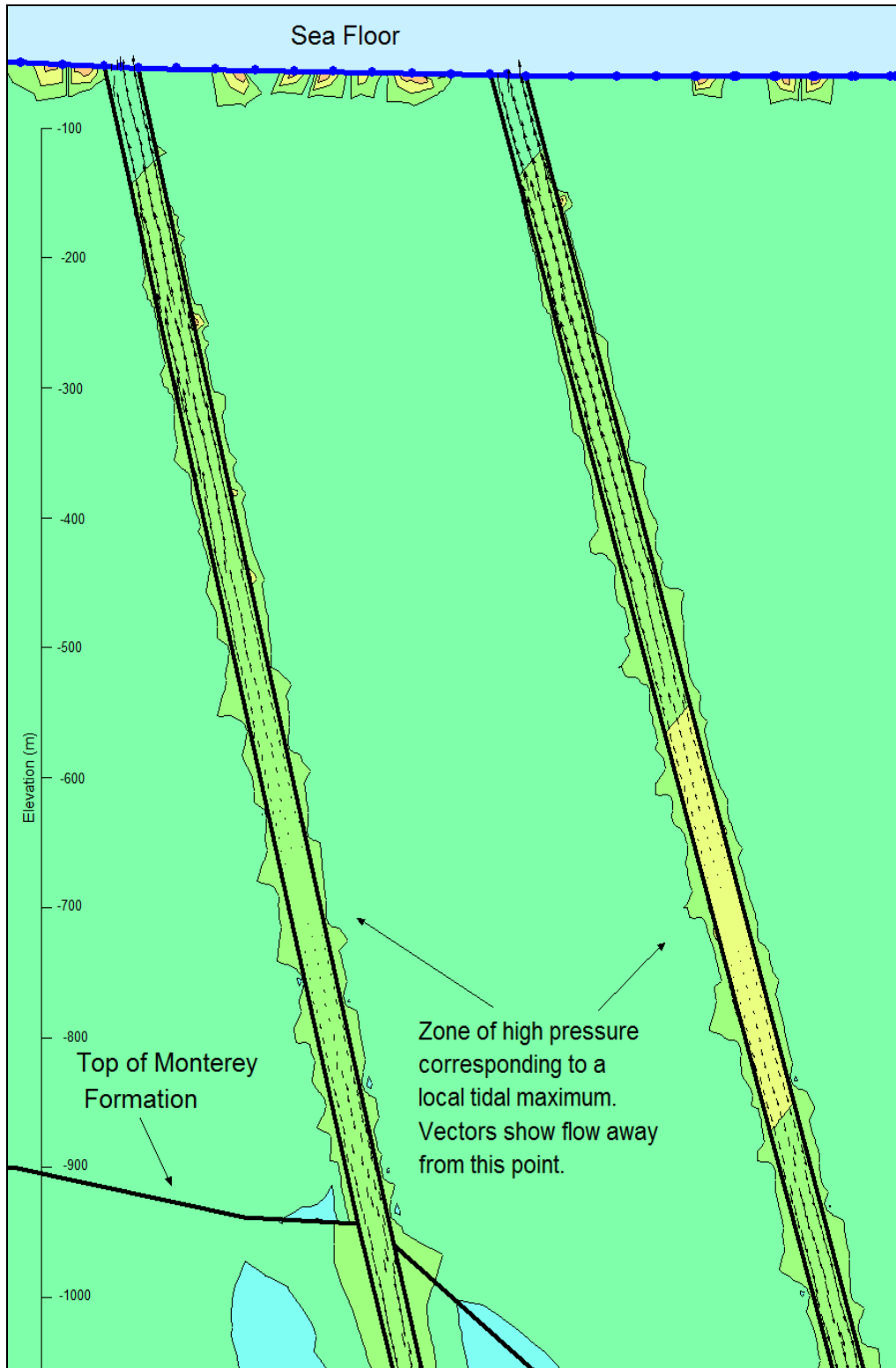


Figure 41. Later pressure propagation showing that tidal pulse has travelled further down fault. $t=14$ hrs.

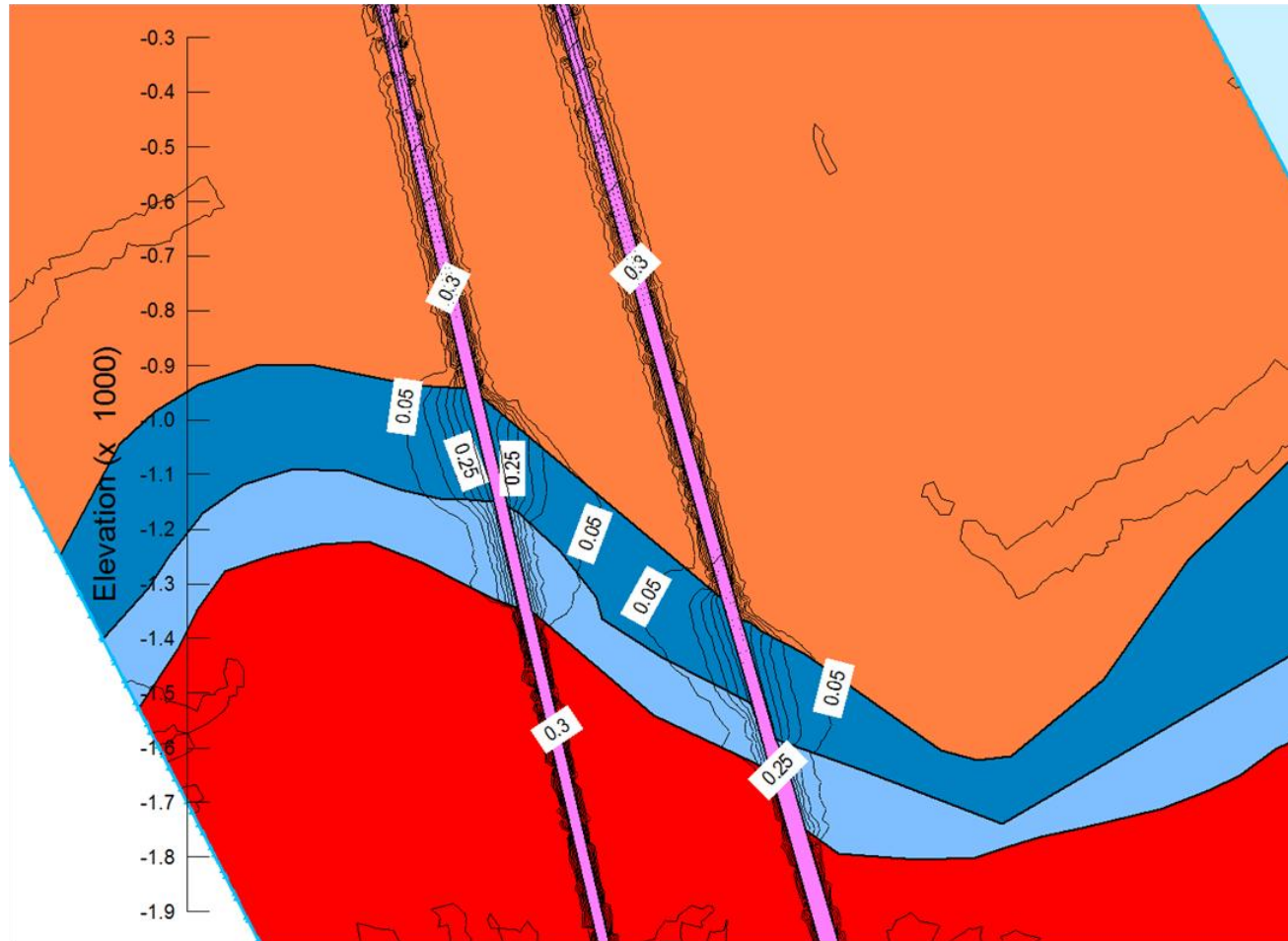


Figure 42. Signal propagation into Monterey Formation (blue). Lines show constant pressure head. $t=236$ hrs. Y axis in meters below sea level.

4.4 Effect of Hydraulic Diffusivity on Signal Propagation

Another objective of this thesis was to conduct a sensitivity study to how a variation in hydraulic diffusivity might affect the signal propagation in the fault. Diffusivity, $D=K/S_s$, is the only parameter needed in the groundwater flow equation to express how head will vary with time and distance. The variation of diffusivity was done to illustrate that this was the principal controlling variable on the tidal signal propagation. The sensitivity study was also done to show that the diffusivity of 13.9 m²/s represents a reasonable value for the fault zone, and that any substantial deviation from this results in either a complete un-attenuated signal or signal that has attenuated to such a level that it does not match the signal seen in the original data set recorded in the field.

Two values of diffusivity were chosen, one higher and the other lower than the 50,000 m²/hr value. The first simulation was done with a diffusivity of 35,000 m²/hr and the second was done with a diffusivity of 65,000 m²/hr. The best way to compare the results of these simulations is to look again at the pressure head variation with time at a depth of 1500 m (5,000 ft) and compare it with the previous simulation and also the recorded field data. These results can be seen in Figures 43-47 below.

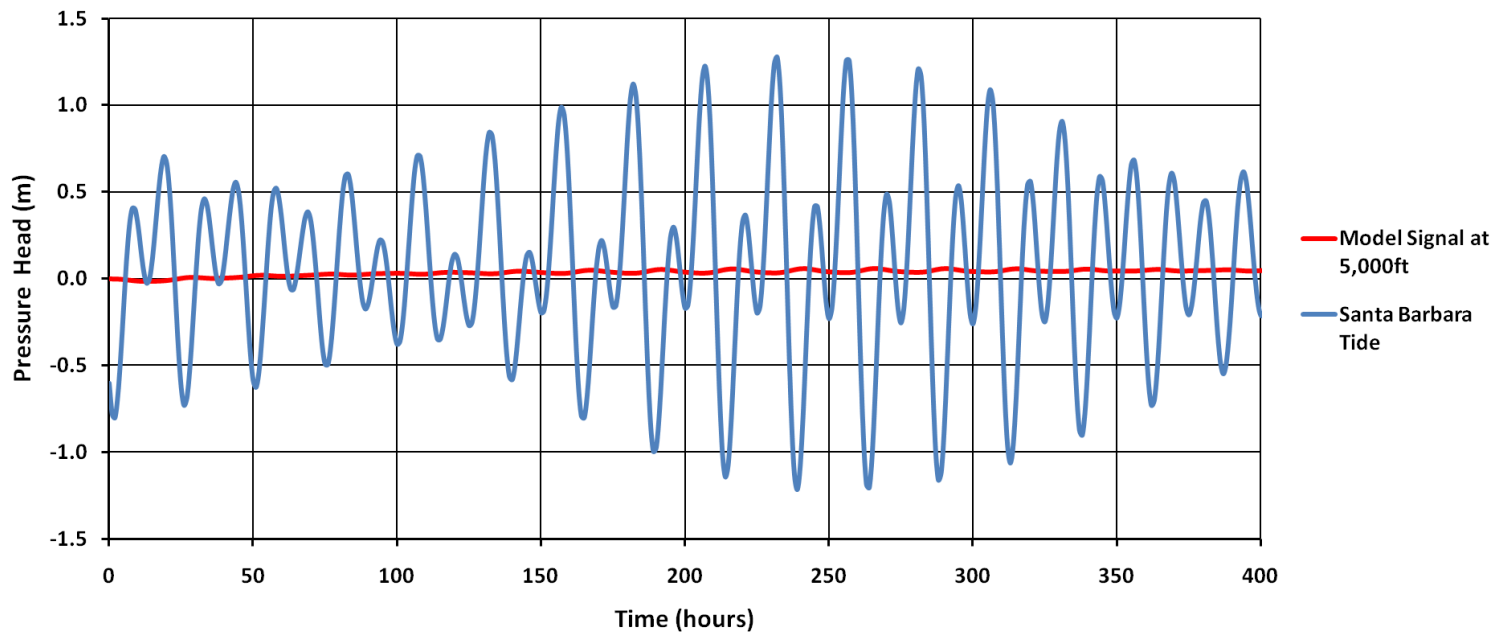


Figure 43. Diffusive Signal and Tidal Signal at -1500 m for $D=9.7 \text{ m}^2/\text{s}$. Note that signal predicted by model is marginal compared with tide.

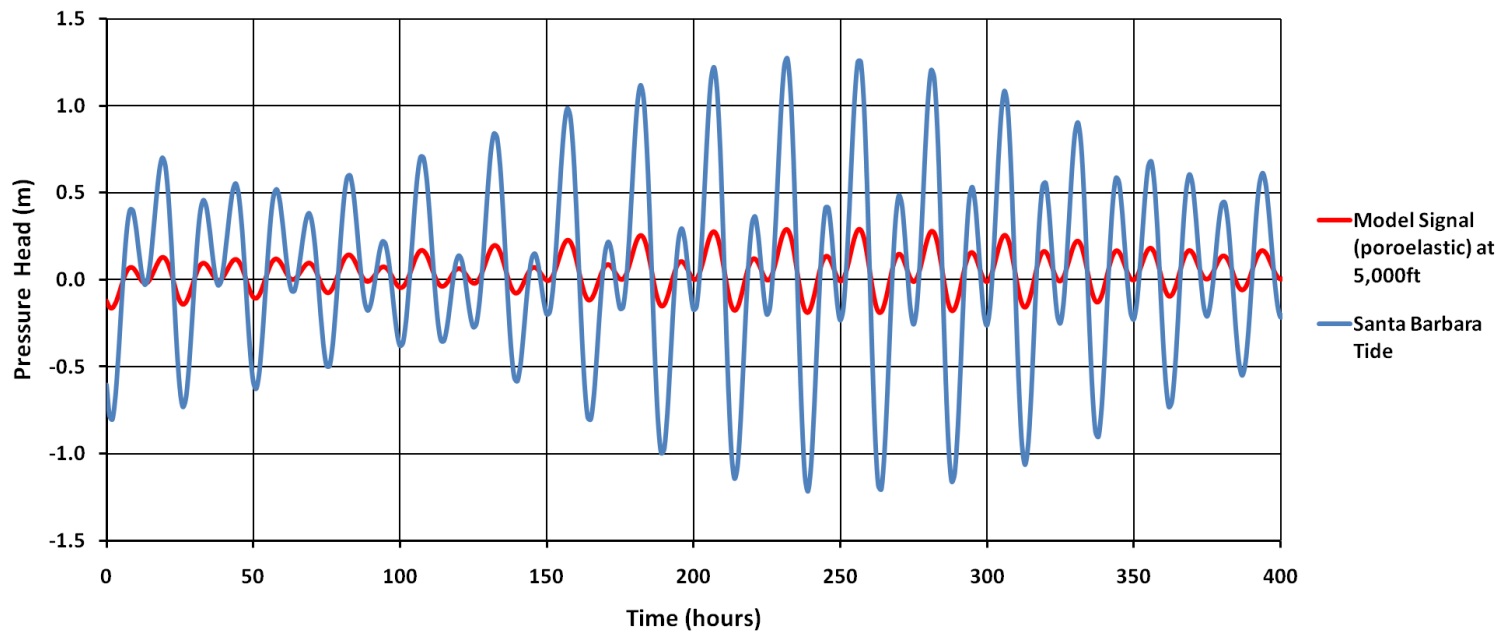


Figure 44. Diffusive and elastic signal with tide at -1500 m for $D=9.7 \text{ m}^2/\text{s}$. Note how elastic signal component overwhelms the diffusive signal and makes it seem as if there is no time lag.

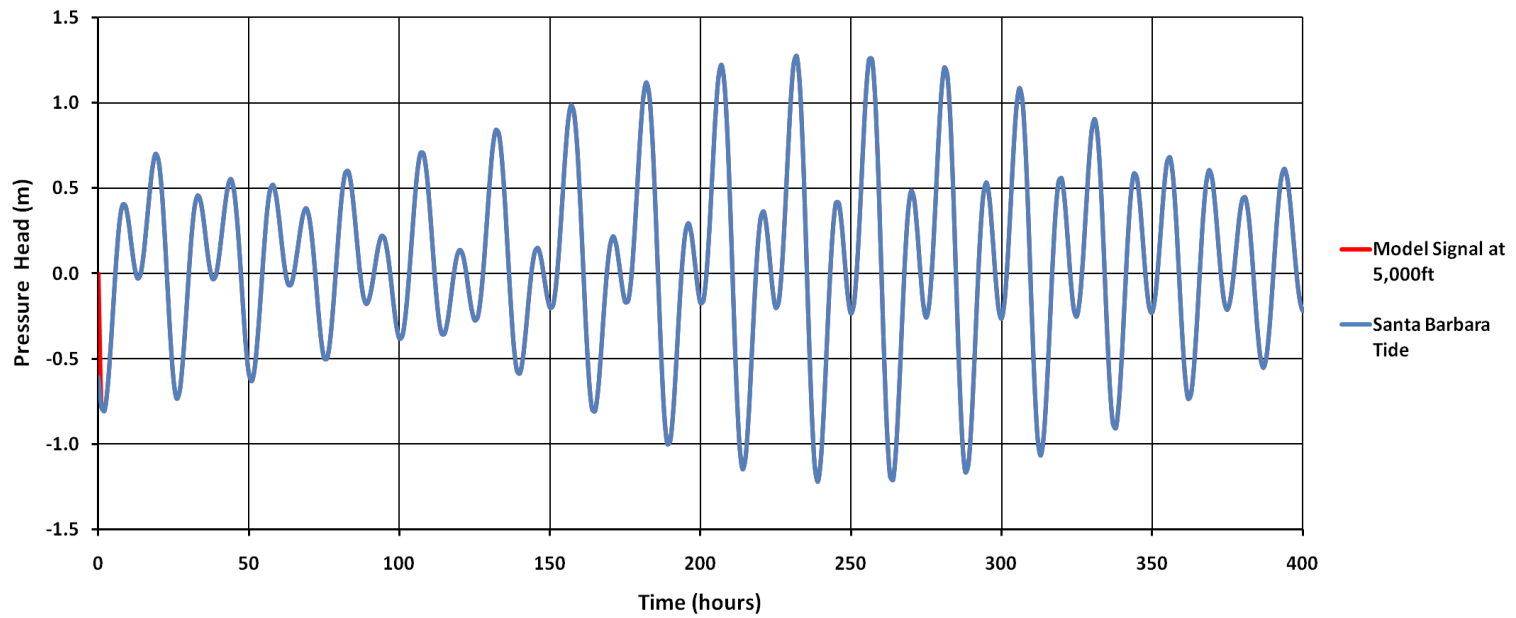


Figure 45. Diffusive signal and tidal signal at -1500 m for $D=18.1 \text{ m}^2/\text{s}$. Both the diffusive signal (model prediction) and the tidal signal are plotted in the figure but since the tidal signal does not attenuate they remain the same and no distinction appears.

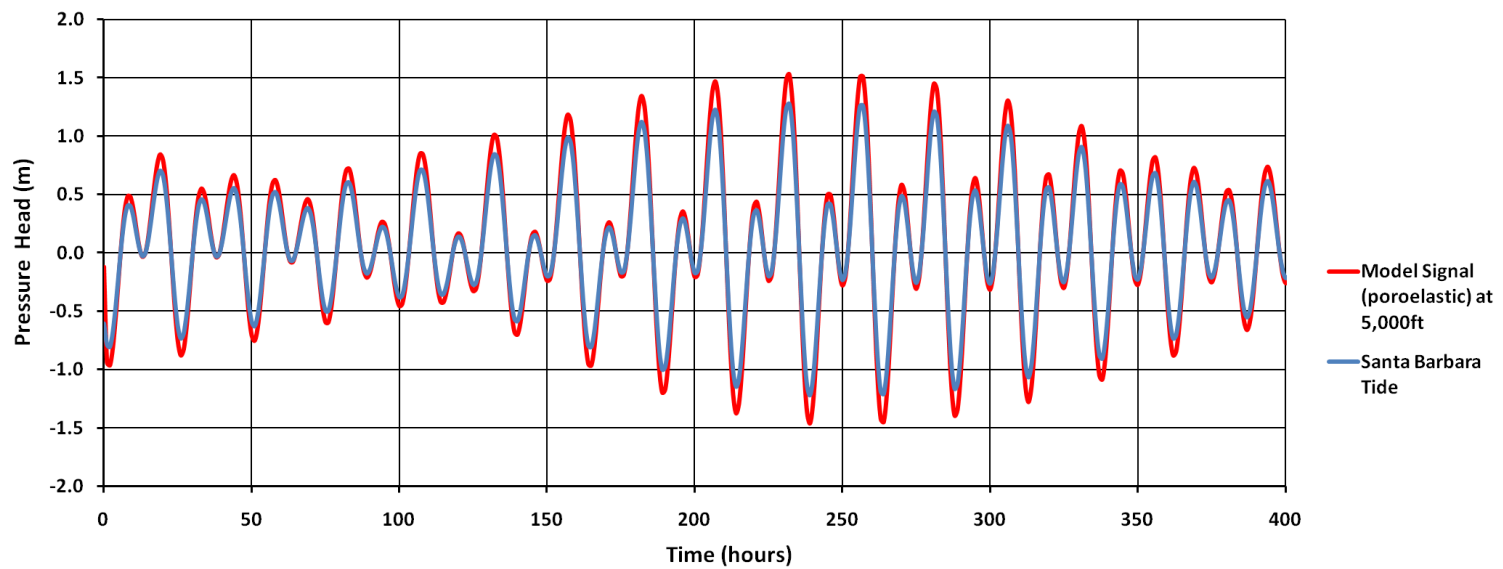


Figure 46. Diffusive Signal with elastic component added on with tidal signal at a depth of 1500 m for $D=18.1 \text{ m}^2/\text{s}$. Note how signal at depth is actually greater than tidal signal.

4.5 Summary

This chapter utilized numerical modeling of the one-dimensional groundwater flow equation to better explore and better understand the tidal signal propagation and attenuation in the South Ellwood fault zone. The first simulation focused on using the hydraulic diffusivity calculated by the analytical time lag solution to simulate propagation down the fault. This simulation has yielded some interesting results concerning the pressure head distribution at any given time and also the two-dimensional propagation into the Monterey Formation and illustrates that this is a real possibility depending on the anisotropy and heterogeneity of the formation. The second simulation illustrated the results of altering the hydraulic diffusivity parameter and show that deviations from a diffusivity of $13.9 \text{ m}^2/\text{s}$ result in a signal attenuation that does not match the field data recorded in Well #13. Further implications of the modeling will be discussed in the next chapter.

Chapter 5: Conclusions

5.1 Thesis Summary

In this thesis the mechanics controlling the propagation and attenuation of a tidal signal in the South Ellwood fault zone have been examined and various parameters have been calculated. The physical laws that govern the propagation and attenuation of the signal come from the theory of poroelasticity and the phenomenon can be classified as a poroelastic process. Likewise the processes contains a part defined by traditional groundwater flow theory and a part derived from geomechanics and classical mechanics of granular materials.

Given that much scientific and engineering interest exists around the hydraulic and mechanical properties of fault zones, a serious attempt has been made here to determine various coefficients that would define the “fault-zone” properties from a mechanical and hydraulic perspective. These parameters include the loading efficiency, vertical modulus, and hydraulic diffusivity. These parameters have been estimated using analytical solutions derived from the theories of heat / groundwater flow and classical soil mechanics.

Before arriving at a point where actual analytical solutions and numerical modeling could be constructed, a great deal of signal analysis had to be performed on both the tidal signal and the signal recorded at depth in a reservoir near the fault. This work consisted of de-trending the signal at depth, implementation of a discrete Fourier transform analysis and conducting a least squares harmonic regression. The principal objective of this was to show that both the tidal signal and signal at depth contained tidal frequencies, and to break out the amplitude and phase of each of the five major tidal

constituents from the records. The amplitudes and phase angles could then be used in analytical solutions to calculate various formation properties.

These calculations have been performed under certain assumptions about the geology, location of the pressure transducer, and the drainage conditions surrounding the fault zone material. This study has attempted to explore the range of hydraulic and anisotropic conditions existing along the South Ellwood fault zone and nearby Monterey Formation. A two-dimension numerical model was built to better explore how pressure changes along the fault zone change with the rising and falling of the tide, and to understand how changes in hydraulic diffusivity might affect the tidal signal. This model was constructed using SEEP/W and careful attention was given to ensure that it represented the stratigraphy beneath Platform Holly in the Santa Barbara Basin.

5.2 Discussion of results

5.2.1 Applications of Analytical Models

The first analytical solution employed in this study was to treat the amplitude to amplitude ratio as a direct measure of loading efficiency or Skempton's coefficient. The direct amplitude to amplitude measurement yielded a value of $\Upsilon \sim 0.15$ for efficiency. A series of charts were produced to learn more about Υ and β assuming the pore fluid was either water or gas (Figure 20-27). Given the natural gas seepage along the fault zones immediately around Platform Holly, it is likely that gas fills the pore space and therefore the gas curves (Figures 24-27) should be used for interpretations of loading efficiency.

To treat the signal amplitude ratios as a direct measurement of loading efficiency is warranted for either rapid loadings or Earth materials of low hydraulic conductivity. Only in these situations can the porous medium be thought of as exhibiting undrained

characteristics. This is not the case for the data set seen in Figure 14, which shows that one signal is lagging the other by 9 hours. The behavior of a truly un-drained material would show a 1 : 1 response in the surface loading to pore pressure at depth.

To address the presence of a time lag in the data, the solution by Jacob and Ferris was applied which allows one to solve for the hydraulic diffusivity of the South Ellwood fault. This diffusivity was calculated for each harmonic constituent and an average value of $13.9 \text{ m}^2/\text{s}$ is a representative value. The solutions by Jacob & Ferris also includes equation 29 which allows one to solve for the diffusivity based on the assumption that the amplitude decay is exponential. This equation yields a value of diffusivity that ranges from 42.7 and $97.2 \text{ m}^2/\text{s}$ which incredibly high for any material and likely unrealistic for the fault zone.

The reasons for the extreme differences in diffusivity prediction by these two methods are interesting to consider and likely illustrates something about the data set. In developing (29) and (27) Ferris simply assumed that the groundwater problem seen in tidal signal fluctuation was perfectly analogous to the same problem in heat flow. Ferris states in his paper that these solutions were previously defined in Ingersoll et al. (1948 p. 48) which is a large compilation of various solutions to heat flow. The fact that the diffusivities do not match and that they significantly deviate illustrate that while the analogy between heat flow and groundwater flow still holds it is not perfect and other factors must be at work in the processes.

The most likely factor that contributes to the difference in hydraulic diffusivities in the Ferris / Jacob model is the fact that part of the signal is due to poroelasticity or the loading efficiency term already discussed. This factor was noted by van der Kamp and others in the 1980's and led to the implementation of (31) and (32) to the data set. This equation assumes that part of the signal at depth is due to the instantaneous, un-drained response of the formation and part due to a diffusive component governed by the basic

form of the groundwater flow equation. The use of this equation predicts the same hydraulic diffusivity value as the Ferris heat flow solution but also provides a loading efficiency. Based on the analytical solution (Eq. 31 and Table 7) the loading efficiency is approximately $\Upsilon=0.20$ for all the tidal constituents. This result at first appears unusual, because the loading efficiency is greater than the amplitude ratio determined from the least-squares harmonic regression. However, since the signal at depth is a summation of the instantaneous poroelastic response and the diffusive attenuation of the signal it is possible that the diffusive part is decreasing the higher contribution from the poroelastic loading efficiency part.

The analytical solution seen in (32) is plotted out for both the K_1 and M_2 diurnal and semidiurnal frequencies. These two plots (Fig. 28 and 29) show the true poroelastic signal attenuation with depth. This figures shows different values of loading efficiency, over a range $0.15 < \Upsilon < 0.25$. While other constituents exist in the signal these two are the dominant two and all others are close in frequency to these and any deviations are marginal.

5.2.2 Application of SEEP/W modeling

The use of 2-D numerical modeling in this study has yielded some interesting results on the constraints on the hydraulic diffusivity term, the application of analytical solutions, pressure distribution within the fault zone, and two dimensional effects. SEEP/W has proven to be a highly useful tool to conduct this type of modeling. The automatic meshing algorithms proved invaluable in ensuring that the geometry seen in Figure 28 could be accurately modeled with minimal error.

The first conclusion that can be drawn from the finite element modeling is to show that the analytical solutions provided by Ferris and Jacob are accurate in predicting

the diffusive behavior of the signal down the fault. It was a hypothesis of the author that the model of Ferris and Jacob for a confined aquifer extending under the sea could be applied to a vertical, permeable fault zone with little interference in the signal attenuation. This assumption was also held by other authors who were dealing with barometric loadings (Lu, 2001). Figure 36 gives a clear presentation of how the attenuation expression of Ferris matches the output from the simulation. The model of Jacob and Ferris appears just as applicable to a permeable fault zone as it does to a confined aquifer extending under the sea.

The attempt at replicating the Well #13 signal, assuming no poroelastic (load efficiency) correction, and using only the basic groundwater flow equation built into SEEP/W was largely successful. This simulation yielded results that compared well with the observed field data recorded in Well #13, when comparing the simulations amplitude and time lag. The attempt at correcting the model simulation by adding in the poroelastic term seen in Figures 33 and 35 still yielded an amplitude that compared well with the observed field data, but seemed to erase a portion of the time lag. This is due to the poroelastic loading efficiency term eclipsing the diffusive component.

The simulation suggests that the poroelastic loading efficiency component has very little impact on the signal propagation and attenuation and the entire processes can successfully be modeled with the basic groundwater (diffusion) equation. It is hard to believe, however, that the fault zone is truly non deformable considering that the pore space is most likely saturated with gas or a mixture of gas and modified seawater. The lack of a loading efficiency effect does not make sense with the use of the Ferris Jacob analytical expression to calculate diffusivity. The hydraulic diffusivity used to create Figure 36 was $13.9 \text{ m}^2/\text{s}$ which was estimated by the time lag method, used in the simulation and not by the amplitude attenuation expression. It is likely then that the attempt to correct the model simulation for loading efficiency is inaccurate.

Figures 37-41 show how the pressure distribution within the fault zone changes with the rising and falling of the tide at the seafloor. These figures show how the tide acts a true transient load on the fault zone material sending a “pulse” of high pressure head down the fault zone. The figures show how for the rising of the tide the pressure gradient and pulse of pressure is directed down the fault-zone into the formation. When the tide begins to recede the reverse phenomenon occurs and a low pressure pulse propagates down the fault. The effect on any give particle of gas or water sitting in the fault zone is to constantly cycle back and forth for both the incoming and outgoing tide.

The simulation using the 400 hour tidal record and the assumed diffusivity of $13.9 \text{ m}^2/\text{s}$ also illustrated that the tidal signal was capable of propagating down the fault zone and into surrounding shale and sandstone formations. This is illustrated in Figure 40, where tidal effects propagate about 100 m from the fault zone. It should be noted that properties assigned to the Monterey Formation were estimated from other independent studies in the Santa Barabara basin. This simulation confirms that even if Well #13 does not intersect the fault zone completely and simply comes near the fault zone to within 50 m or so, it is likely the pressure transducer would still pick up the signal. The signal propagation into the Monterey Formation would only be improved with the presence of large fractures connecting Well #13 with the fault.

The last simulation was performed to illustrate the effects of significantly changing the diffusivity perimeter from that calculated by the time lag analytical solution. This simulation showed that altering the hydraulic diffusivity will result in either a signal that attenuates to sharply and shows no amplitude decay at depth, or a signal that is perfectly transmitted down the fault with no attenuation at all. It is likely in light of this that the presence of the tidal signal in the fault is very sensitive to the diffusivity parameter which, in turn, is affected by the hydraulic conductivity and specific storage.

Alterations in drained compressibility, fluid compressibility or hydraulic conductivity are likely to strongly affect the nature of the signal propagation.

5.3 Global Conclusions and Fault- Zone Formation Properties

The global conclusions of this study concerning the fault zone material and its mechanical and hydraulic properties can be summarized in the following list. These conclusions are the result of the analysis of this data set with applicable poroelastic theory. Given the diverse nature of fault-zones it would be difficult to apply the exact numerical values of material properties to other fault zones without further detailed studies. The following are conclusions about the fault zone beneath Platform Holly

1. The propagation of the tidal signal is a poroelastic process that can be represented as of diffusive flow governed by Darcy's Law and the elastic loading efficiency term governed by Skempton's coefficient. The expression for the coupling between diffusion and elasticity are provided by Eq. (30) and (31).
2. Hydraulic diffusion part likely defines the majority of the tidal signal. The groundwater flow equation on its own can successfully model the propagation and attenuation.
3. The hydraulic behavior of the fault zone indicates that it is highly transmissive and only a diffusivity of $13.9 \text{ m}^2/\text{s}$ or a value close to this can account for the signal propagation at depth.

4. The range of hydraulic conductivity and specific storage values that can make this value possible are illustrated in the figure below.

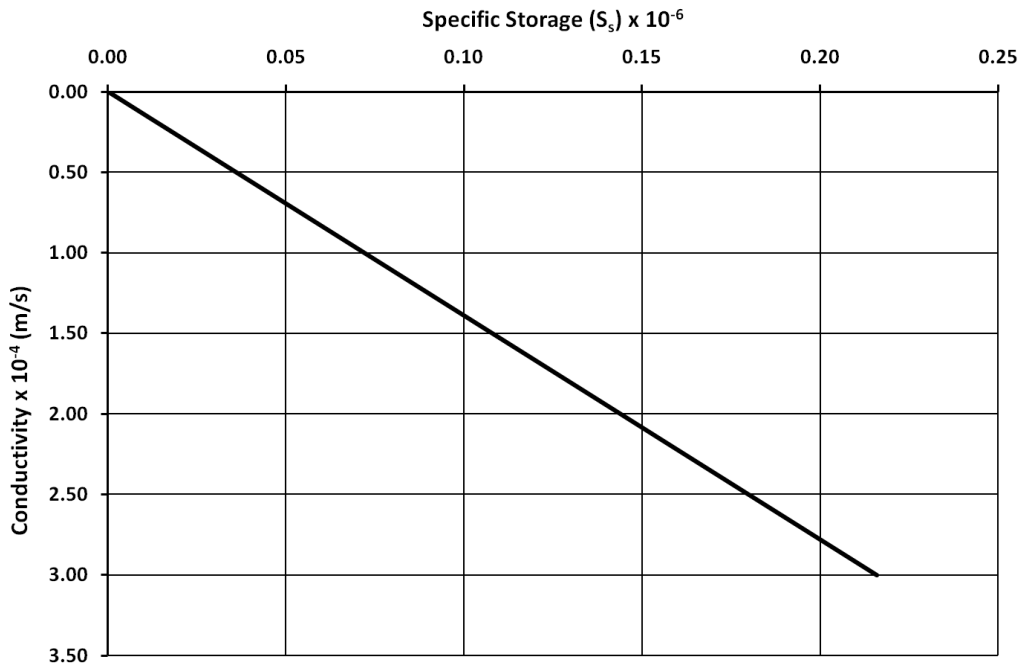


Figure 47. Possible specific range for storage and hydraulic conductivity for the South Ellwood fault-zone.

5. Given that the previous independent hydraulic conductivity estimate from earlier seep tent studies on the fault (Boles and Garven, 2010) reveal a permeability of 30 md which corresponds to a conductivity of 3×10^{-7} m/s assuming water at standard temperature and pressure. This value of conductivity with a diffusivity of 50,000 m^2/hr or $13.9 \text{m}^2/\text{sec}$ means that the specific storage is 2.086×10^{-8} for the fault.
6. The tidal signal can be thought of as transient loading that is applied to the fault-zone and has the effect of stressing it in a certain way. Since the cause of this stress is the tide and no other phenomenon the tidal signal and its attenuated lag

signal at depth is something that is superimposed on whatever hydrodynamic regime has developed beneath Platform Holly. If oil and gas production has significantly altered the pressure regimes in the formation beneath Platform Holly it should have little effect on the presence of the tidal signal at depth. The signal will be an addition to whatever phenomenon is occurring at depth. This fact is apparent in the original signal data which shows the signal imposed on pressure recovery in the formation after hydrocarbon production was suspended.

7. While the signal does not depend on the hydraulic regime the hydraulic diffusivity and loading efficiency calculated are parameters that are material properties and can be used to predict pressures and fluid migration up and down the fault zone.
8. The loading efficiency is $\gamma = 0.2 \pm 0.05$ as calculated by the analytical solution of (Wang, 2000). The loading efficiency charts shown earlier previously should be used to determine a modulus from this value depending on the porosity and Poisson's ratio one wishes to adopt.
9. The use of the tidal signal should be given more attention as an in-situ field test for determining formation properties when highly permeable materials are under consideration. The oil industry could gain significantly from this considering that many drilling operations are conducted off shore. The tide constitutes a predictable transient loading that should be taken advantage of in determining formation properties wherever possible.

10. If long term monitoring of the signal at depth in the formation is possible this should be done since changes in the nature of the signal (amplitude and time lag) mean either an alteration in the hydraulic or mechanical properties of the fault zone material. Hydraulic or mechanical changes in the fault could have implications for seawater intrusion down the fault and into the Monterey Formation. If for example the time lag is seen to decrease over the course of a few years it would signify an increase in hydraulic diffusivity.

5.4 Suggestions for Future Work

The greatest limitation to this study has been the fact that the original data set is secondary information gathered from a test that was intended to gain information about the recovery of pressures beneath Platform Holly. The purpose of this test was not to generate useful data for poroelastic calculation of a fault zone, though this information was determined from the data set. Now that the phenomenon of tidal propagation and attenuation is known to occur along the fault zones near Platform Holly it would be highly desirable to record the tidal signal at varying depths and for a period of at least 30 days. This type of data would yield even more certainty in resolving the five major harmonic constituents and allow for the calculation of diffusivity and loading efficiency at multiple locations allowing more certainty in the D and γ values calculated here.

In addition to a longer signal record it would be desirable to determine the mechanical properties of the fault-zone by laboratory analysis of core sample taken from the fault zone. This type of testing would ideally begin with an understanding of the percentage of gas filling the pore space and replicate that percentage of gas in the

laboratory. If this testing could be done with a tri-axial cell or similar equipment it would be possible to determine Skempton's B coefficient, Poisson's ratio, the drained modulus (or compressibility) and un-drained modulus. It would be great to compare the results of such a testing program to the "in-situ" values calculated in this study.

Another direction for future study would be to conduct more in-depth computer modeling. SEEP/W has proven to be an effective tool to use in this study and its continued use is highly suggested for studying the effects of signal propagation. Ideally any numerical method would solve (31) directly since this is the true expression for the signal propagation containing both a diffusive and elastic component. Future simulations might explore the use of SEEP/W and SIGMA/W to model the signal.

A final direction for research should be to take into account the effects of temperature and salinity on the signal attenuation with depth since these values have been known to vary with depth (Boles et al., 2004). The effects of temperature and salinity would be present in both the hydraulic conductivity and specific storage term.

References

- Antonellini, M., Aydin, A., Outcrop-Aided Characterization of a Faulted Hydrocarbon Reservoir: Arroyo Grand Oil Field, California, USA *Faults and Subsurface Fluid Flow in the Shallow Crust*. Geophysical Monograph 113, p. 7-26, AGU, Washington DC, 1999.
- Aydin, A., Fractures, faults, and hydrocarbon entrapment, migration and flow. *Marine and Petroleum Geology*, v. 17 (7), p. 797-814, 2000.
- Boles, J.R., Horner, S., and Garven G., Permeability estimate of the South Ellwood Fault. *Society of Petroleum Engineers Western Regional Meeting*, Anaheim, CA, SPE Paper No. 133613-MS, 2010.
- Boles, J.R., Eichhubl, P., Garven, G., and Chen, J., Evolution of hydrocarbon migration pathway along a basin-bounding fault: evidence from fault cements. *AAPG Bulletin*, v. 88, p. 947-970, 2004.
- Braun, J., Munroe, S.M., and Cox, S.F., Transient fluid flow in and around a fault. *Geofluids*, v. 3, p. 81-87, 2003.
- Bredehoeft, J.D., Fault permeability near Yucca Mountain. *Water Resources Research*, v. 33, p. 2459-2463, 1997.
- Boon, J. D. , *World Tides User Manual* . Gloucester Point, VA, USA, 2007
- Caine, J. S., Evans, J. P., and Forester, C. B., Fault zone architecture and permeability structure. *Geology* , v. 24 (7), p. 1025-1028, 1996.

- Carr, P. A., and van der Kamp, G. S.,. Determining aquifer characteristics by the tidal method. *Water Resources Research*, v. 5 (5), p. 1023-1031, 1969.
- Chao, S., Javandel, I., and Witherspoon, P., Characterization of leaky faults: Study of air flow in faulted vadose zones. *Water Resources Research*, v. 35 (7), p. 2007-2013, 1969.
- Cocco, M., Rice, J.R., Pore pressure and poroelasticity effects in Coulomb stress analysis of earthquake interactions. *Journal of Geophysical Research*, v. 107 (B2), p. ESE 2-1—ESE 2-17, 2002.
- Dake, L.P.,. *Fundamentals of Reservoir Engineering*. ,Amsterdam: Elsevier, 1978.
- Domenico, P. A., Schwartz, F. W., *Physical and Chemical Hydrogeology*, New York: John Wiley & Sons, 1990.
- Education/tutorial tides: National Oceanic Atmospheric Administration*. NOAA, http://oceanservice.noaa.gov/education/tutorial_tides/tides02_cause.html, Accessed 2013.
- Emery, W. J., Thomson, R. E., *Data Analysis Methods in Physical Oceanography* Amsterdam: Elsevier, 2010.
- Evans, J. P., Forester, C. B., Goddard, J. V. ,Permeability of fault-related rocks, and implications for hydraulic structure of fault zones. *Structural Geology* , 1997, v.19 (11), p. 1393-1403.
- Fante, R. L.,. *Signal Analysis and Estimation An Introduction*., New York: John Wiley & Sons, 1988.
- Ferris, J.G., Cyclic Fluctuations of Water Level as a basis for Determining Aquifer Transmissibility, *Department of the Interior Geological Survey Water Resources Division Ground Water Branch*, Washington DC, 1952.

Fisher, Q.J., Knipe, R.J. The permeability of faults within iliclastic petroleum reservoirs of the North Sea and Norwegian continental shelf. *Marine and Petroleum Geology.*, v. 18, p. 1063-1081, 2001.

Freeze, R. A., Cherry, J. A., *Groundwater*, Prentice-Hall, Englewood Cliffs, N. J., 1979.

Galloway, J. M., Santa Barbara-Ventura Basin Province. *Structure and Petroleum Geology, Santa Barbara Channel, California* , Miscellaneous Publication 46. (eds Kunitomi DS, Hopps TE, Galloway JM), p. 63-72. Pacific Section AAPG, Bakersfield CA, 1998.

Ge., S., Garven, G., Hydromechanical modeling of tectonically driven groundwater flow with applicant to the Arkoma foreland basin. *Journal of Geophysical Research*, v. 97, p. 9119-9144, 1994.

Harden, D. R., *California Geology.*, Simon&Schuster, 1998.

Heck, R. G., Santa Barbara Channel Regional Formline Map. *Structure and Petroleum Geology, Santa Barbara Channel, California*, Miscellaneous Publication 46 (eds Kunitomi DS, Hopps TE, & Galloway JM), p. 183-185. Pacific Section AAPG , Bakersfield CA, 1998.

Heynekamp, M. R., Goodwin, L. B., Mozley, P. S., and Haneberg, W. C., Controls on fault-zone architecture in poorly lithified sediments, Rio Grande Rift, New Mexico: Implications for Fault-Zone Permeability and Fluid Flow . *Faults and Subsurface Fluid Flow in the Shallow Crust* . AGU, Washington, D.C., 1999.

Holtz, R. D., Kovacs, W. D., *An Introduction to Geotechnical Engineering*. 1981, Upper Saddle River : Prentice-Hall Inc.

Ingersoll, L.R., Zobel, O.J., and Ingersoll, A.C., *Heat Conduction With Engineering and Geological Applications*. New York: McGraw-Hill Book Company LLC, 1948.

Ippen, A. T. ,*Estuary and Coastal Hydrodynamics*, New York: McGraw-Hill Book Company LLC, 1996.

Jacob, C. E., The flow of water in an elastic artesian aquifer, *Trans American Geophysical Union* , v. 21, p. 574-586, 1940.

Jiao, J. J., Tang, Z., An analytic solution of groundwater response to tidal fluctuation in a leaky confined aquifer. *Water Resources Research* , v. 35, pp. 747-751, 1999.

Lambe, W. T., Whitman, R. V., *Soil Mechanics*, New York: John Wiley & Sons, 1969.

Levorsen, A. I., *Geology of Petroleum*, W.H. Freeman and Company, 1967.

Lu N. , Determining fault permeability from subsurface barometric pressure *Geotechnical and Geoenvironmental Engineering*, v. 127 (9), p. 801-808, 2001.

Merrit M.L., Estimating Hydraulic Properties of the Floridan Aquifer System by Analysis of Earth-Tide, Ocean-Tide, and Barometric Effects, Collier and Hendry Counties Florida *Water-Resources Investigations Report 03-4267*. U.S Geologic Survey, Tallahassee, FL, 2004.

Minor, S. A., Kellogg, K. S., Stanley, R. G., Brandt, T. R., *Geologic Map of the Goleta Quadrangle, Santa Barbara County, California*. Open File Report, U.S. Department of Interior, U.S. Geological Survey, 2007.

Nelson, E. P., Kullman, A. J., Gardner, M. H., Batzle, M., Fault-Fracture Networks and Related Fluid Flow and Sealing, Brushy Canyon Formation, West Texas. *Faults and*

Subsurface Fluid Flow in the Shallow Crust, Washington, D.C.: American Geophysical Union, 1999.

Neuzil, C.E., Hydrodynamic coupling in geologic processes. *Hydrogeology Journal*, v. 11, p. 41-83, 2003.

Nur, A., Byerlee, J. D., An exact effective stress law for elastic deformation of rock with fluids. *Geophysical Reserch.*, vol. 84, p.6071-6082, 1971.

Odling, N.E., Harris, S.D., Knipe, R.J., Permeability scaling properties of fault damage zones in siliclastic rocks. *Structural Geology*, v. 26, p. 1727-1747, 2004.

Platform Holly: Where We Work:Venoco Inc., Retrieved January 1, 2013, from Venoco Inc: <http://www.venocoinc.com/>, 2001.

Redin, T., Forman, J., Kamerling, M. J., Regional Structure Section Across the Eastern Santa Barbara Channel, from Eastern Santa Cruz Island to the Carpinteria Area, Santa Ynez Mountains. *Structure and Petroleum Geology, Santa Barbara Channel, California , Miscellaneous Publication 46*. Bakersfield, C.A.: Pacific Section AAPG and Coast Geological Society, 1998

Shan, C., Javandel I., Witherspoon, P.A.,Charachterization of leaky faults: Study of air flow in faulted vadose zones. *Water Resources Research*, v. 35, p. 2007-2013, 1999.

Sibson, R.H., An episode of fault-valve behaviour during compressional inversion?-The 2004 M6.8 Mid-Niigata Prefecture, Japan, earthquake sequence. *Earth and Planetary Science Letters*, v. 257 (1-2), p. 188-199, 2007.

Sigda, J.M., Goodwin, L.B., Mozley P.S., Wilson, J. L., Permeability Alteration in Small-Displacement Faults in Poorly Lithified Sediments: Rio Grande Rift, Central New

Mexico. In: *Faults and Subsurface Fluid Flow in the Shallow Crust*, Geophysical Monograph 113 (eds Haneberg WC, Mozley PS, Moore JC, Goodwin LB), p. 51-69. AGU, Washington, DC, 1999.

Stanislavsky, E., Garven, G., A theoretical model for reverse water-level fluctuations induced by Transient Permeability in Thrust Fault Zones. *Earth and Planetary Science Letters*, v.210 (3-4), p. 579-586, 2003.

Tennyson, M. E., Kropp, A. P., Regional Cross Section Across Santa Barbara Channel from Northwestern Santa Rosa Island to Canada de Molino. *Structure and petroleum Geology, Santa Barbara Channel, California* , Miscellaneous Publication 46 (eds Kunitomi DS, Hopps TE, Galloway JM), p. 185-193. Pacific Section AAPG, Bakersfield, CA, 1998.

van der Kamp, G., Tidal Fluctuations in a Confined Aquifer Extending Under the Sea. *24th International Geological Congress*, Montreal, p. 101-106, 1972.

van Der Kamp, G., Gale, J. E. , Theory of Earth Tide and Barometric Effects in Porous Formations with Compressible Grains. *Water Resources Research* , 1983, v. 19 (2), p. 538-544, 1983.

Vedder, J. G., Wagner, H. C., Schoellhamer, J. E., Geology, Petroleum Development and Seismicity of the Santa Barbara Channel Region, California. U.S. Department of the Interior. Geologic Survey Professional Paper 679, 1969.

Wang, H. F., *Theory of Linear Poroelasticity*, Princeton, New Jersey: Princeton University Press, 2000